Survey of Dense Cores in Orion Molecular Clouds 2, and Detection of Extremely High Velocity Flows

松下, 祐子

https://doi.org/10.15017/4059983

出版情報：九州大学, 2019, 博士（理学）, 課程博士
バージョン：
権利関係：

Survey of Dense Cores in Orion Molecular Clouds 2, and Detection of Extremely High Velocity Flows

MATSUSHITA Yuko

Department of Earth and Planetary Sciences,
Graduate School of Science, Kyushu University

January 15, 2020

Abstract

I investigated new 1.3 mm continuum sources and extensive CO J = 2–1 and SiO J = 5–4 outflows located in the Orion Molecular Cloud 2 FIR 6 (OMC-2/FIR 6) region. In total, 21 dust continuum sources have been identified and spatially resolved, in which 1.3 mm continuum sources have dust masses in the range $\sim$ 0.02 to 0.9 $M_{\odot}$. I calculated the dust continuum mass of each source using the integrated flux value measured by Dendrogram using T $\sim$ 25 K. I confirmed that 1.3 mm continuum sources correspond to the previously known 11 sources and discovered 10 new additional sources. Both CO and SiO emissions were detected only in FIR 6 – ALMA 13, and the CO Extremely High Velocity (EHV) flow can be seen only in FIR 6 – ALMA 5. FIR 6 – ALMA 5 and FIR 6 – ALMA 13 clearly show redshifted and blueshifted bipolar outflow. The complexity of the CO line emission is attributed to the contamination from the ambient molecular cloud and it is difficult to determine which object drives outflow. In conclusion, three sources are clearly associated with bipolar outflow and six sources are with moderate outflow. In OMC-2/FIR 6, the detected sources show various evolutionary stages such a starless core, Class 0 and Class II phases, in which the half of sources are associated with outflows. More than half of the continuum sources are not associated with an infrared source. OMC-2/FIR 6 is a very young star formation region. Thus, it is expected that there exist many starless cores.

Contents

Chapter 1

INTRODUCTION

The star is one of the smallest components in the universe and is closely related to the environment and evolution of the universe. Therefore, understanding the process by which stars are formed is a very important clue to know the universe. CO molecular outflows are ubiquitous phenomena in star forming regions independent of central stellar mass (Bachiller and Tafalla 1999, Zhang et al. 2001, Arce et al. 2007). On the other hand, Jet/Extremely High Velocity (EHV) flows are episodic phenomena. Outflows/jets are directly related to the main accretion phase, and the molecular line emission provides key information about the mass accretion and ejection processes during the protostar evolution. The outflows/jets are often used to identify protostars in dense cores. Moreover, molecular outflows are direct evidence of ongoing star formation in a observed region. Therefore, it is possible to discover invisible sources with outflow as a landmark and to measure the activity of star formation in the star forming region.

1.1 Hierarchical Structures of Star Forming Region

The infrared observations have shown that 80 % $\sim$ 90 % of stars belong to the clusters within giant molecular clouds (GMCs located at d $\sim$ 2 kpc). Most stars are formed in embedded clusters, and the isolated star forming environment is considered to be the minor case (Lada and Lada 2003, Porras et al. 2003). Figure 1.1 (a) shows the observation area in (Porras et al. 2003), and (b) shows the observation results for each scale of the cluster/stellar groupe. This result shows that large clusters are the most common. Therefore, embedded clusters and stars in GMCs are very important for understanding the general characteristics of star formation. In addition, embedded clusters are often associated with dense filamentary structures. Molecular clouds contain filamentary structures (Schneider and Elmegreen 1979), and the filaments are ubiquitous and perhaps fundamental structure of molecular clouds. These facts are revealed by the Herschel Space Observatory (André et al. 2014:in Figure 1.2). Filaments exist on a scale of parsec, and have a hierarchical structure, associated with clusters of young stars (Hacar et al. 2013, Takahashi et al. 2013, Wang et al. 2014, Teixeira et al. 2016, Busquet et al. 2016). In the case of Taurus filament L1495/B213, the filament is known to have undergone hierarchical fragmentation (Hacar et al. 2013). There are several velocity-coherent sub-filaments in Taurus filament in Figure 1.2, and each of sub-filaments has the sonic velocity dispersion. A mass-to-length relation is consistent with an isothermal cylinder, thus the filament is considered to be formed by hierarchical fragmentation. Hierarchical thermal fragmentation would occur in other star forming regions, such as the Orion Molecular Cloud (OMC) 1, 2 and 3 (Takahashi et al. 2013) and the Spokes cluster in NGC 2264 (Teixeira et al. 2006, 2007, Pineda and Teixeira 2013, Teixeira et al. 2016). Within the host filaments, the spatial distribution of protostars implies the same fragmentation process independent of the environment of star forming region. The filaments convey the material onto a central hub and the hub should be the formation site of stellar clusters (Myers 2009). Such feeding process have been observed in Serpens south (Kirk et al. 2013), Cygnus-X (Schneider et al. 2010) and infrared dark clouds (Peretto et al. 2013). The fragmentation condition of filaments depends on the gas temperature, density and magnetic field strength. Moreover, the enhanced mass concentrations is also important except for magnetic field, external pressure and cloud rotation (Hanawa et al. 1994, Burkert and Hartmann 2004, Pon et al. 2011).

It is important to research the cluster as landmark, and examine the formation process of the core from the filament. The youngest stellar objects and clusters are identified as infrared excess sources (Myers 2009). The filamentary structures within the molecular clouds and their fragmentation structures (cluster or core) are important to clarifying the initial conditions of the mass distribution of stars forming region and evolutionary sequence.

Within the Orion filament, there are several fragmentation scales between the cloud and core scales. The Orion A and Orion B GMCs have the largest scaling separation of $\sim 4^\circ.7$ (35 pc) (Maddalena et al. 1986). Moreover, the periodically separation with 10 arcmin (1.2 pc) between OMC-1, OMC-2 and OMC-3 within the Orion A cloud has been reported (Dutrey et al. 1991, Hanawa et al. 1993, Johnstone and Bally 1999). OMC filaments contain several dense clumps of $\sim$ 0.1 pc scale, and these clumps are equally separated ($\sim$ 50 arcsec; 0.1 pc) along with the filament (Cesaroni and Wilson 1994, Chini et al. 1997, Lis et al. 1998, Johnstone and Bally 1999). The several continuum sources are revealed within the 0.1 pc clumps, and the separation between nearest neighbors is about 0.06 to 0.035 pc (Takahashi et al. 2013). Therefore, star formation is the results of the hierarchical fragmentation of host filament/clouds.

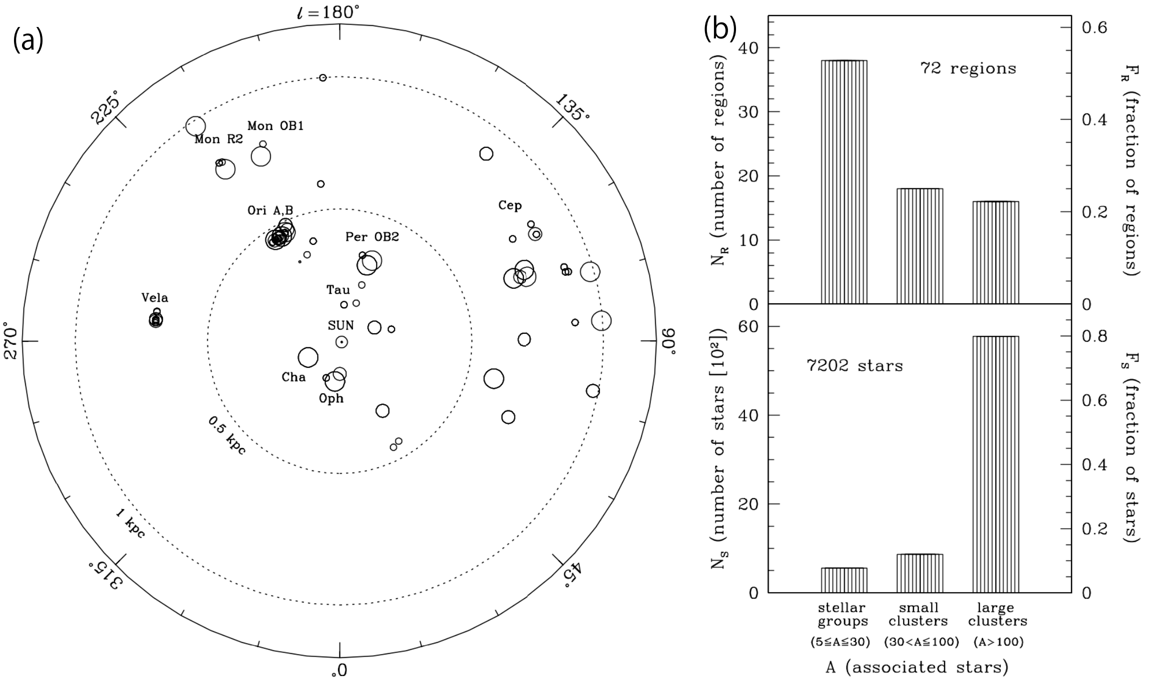

Figure 1.1: (a) In galactic plane, there are the distribution of young stellar groups and clusters. The size of the open symbols correspond to the number of the stars in the cluster. (b) The histogram bars show the number of regions of multiple star formation in the top panel and the associated stars in the bottom panel. These figures are referenced from Porras et al. (2003).

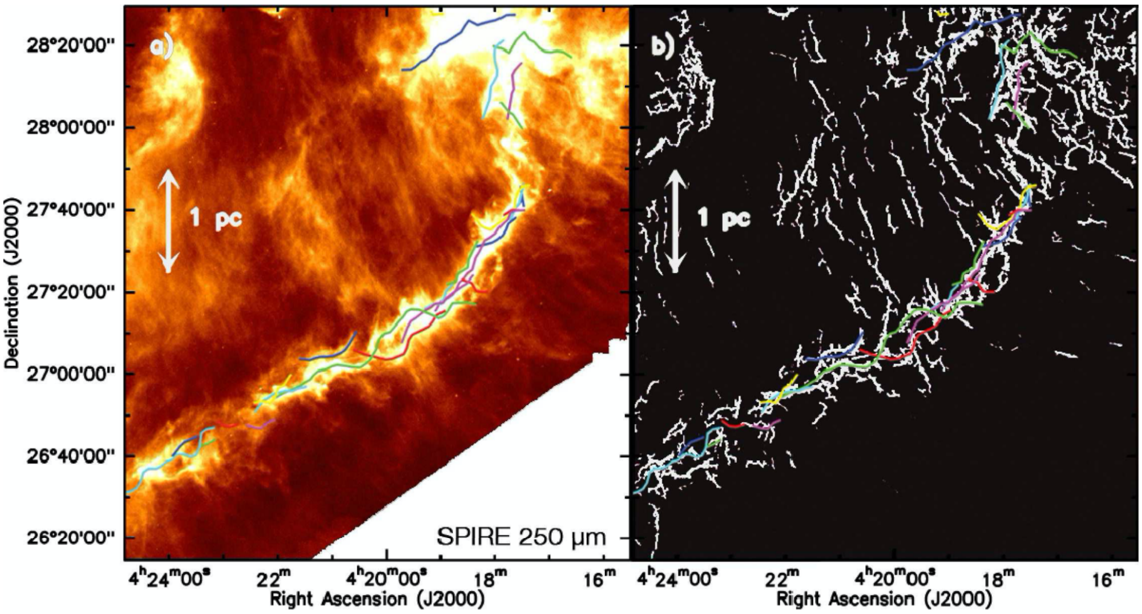

Figure 1.2: (a) There is the image of the B211, B213 and L1495 in Taurus by *Herschel*/SPIRE 250 μm dust continuum. (b) The figure is the result of applying the multi-scale algorithm *getfilaments* to the image of (a). These figures are referenced from André et al. (2014).

1.2 Outflow and Jet Structure

Molecular outflows are ubiquitously observed and theoretically known to be driven in the early evolutionary stage of star formation. On the other hands, the molecular jets are episodic phenomena. The outflow and jet are related to mass ejection and accretion processes. Thus, they are regarded as important indicators for understanding the star formation process. Observations show that there are varieties of molecular outflows such as bipolar or monopolar, low velocity or high velocity flows and wide opening angle or collimated structure. Most of protostars drive only molecular outflow, but a few objects drive both outflow and jet (extremely high velocity flow) at the same time. These sources are called as Extremely High Velocity (EHV) objects. Details are given in Section 1.3.

Although the existence of outflow and jet has been confirmed by observation, their driving mechanisms have not been elucidated. Theoretically, there are two scenarios about the explanation of the driving mechanism of both outflow and jet. (i) nested disk wind scenario (Tomisaka 2002, Banerjee and Pudritz 2006, Machida et al. 2008) and (ii) entrainment scenario (Arce et al. 2007:and references therein). Schematic images of the each scenarios are shown in Figure 1.3. In the former scenario, outflows are driven by the circumstellar disk and jets are directly driven by the protostar, respectively (Machida 2014). The low velocity outflow is magnetically accelerated by the rotationally supported disk. On the other hand, in the latter scenario, only the high velocity jet is driven by the protostar. The jet is accelerated and entrains the surrounding infalling material and gas until the entrained gas reaches supersonic speed. As a result, the low velocity outflow is created by the high velocity jet (Arce et al. 2007). Both scenarios imply that the jet is driven by the centrifugal and Lorentz forces (Kudoh and Shibata 1997, Spruit et al. 1997, Tomisaka 2002, Machida et al. 2008, Seifried et al. 2012).

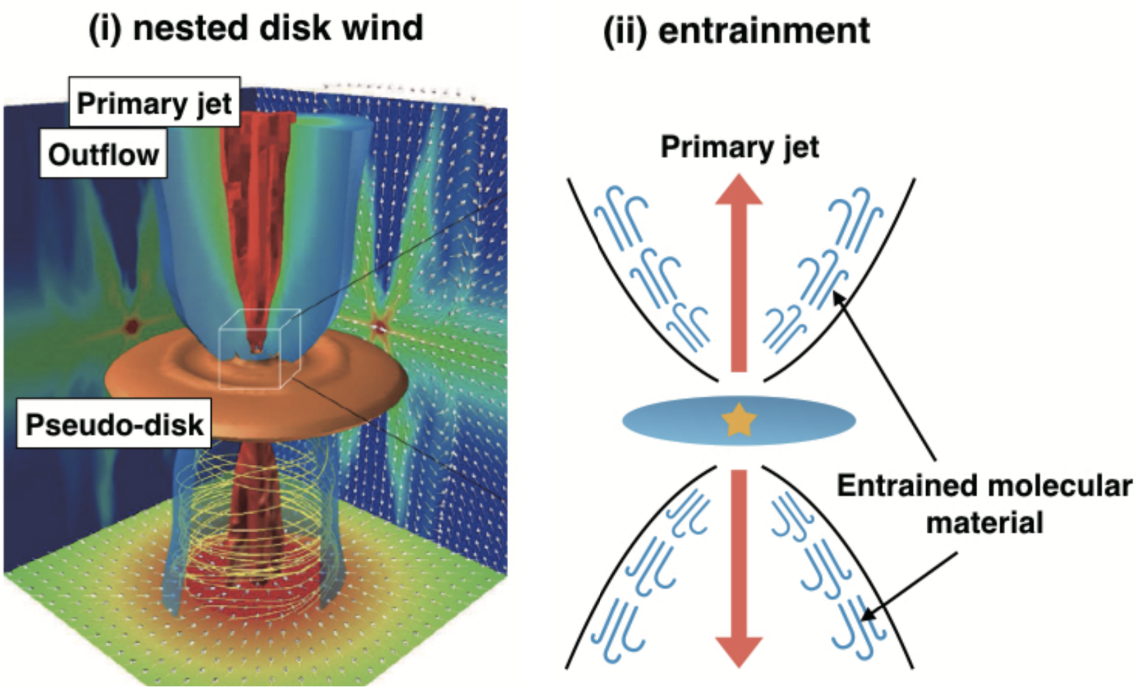

Figure 1.3: (i) The schematic image shows the nested disk wind scenario. This figure is referenced from Machida et al. (2008). (ii) The schematic image shows the entrainment scenario.

1.3 Extremely High Velocity Objects

The most energetic and high velocity flow, detected by molecular line emission, is called as the Extremely High Velocity (EHV) flow (Bachiller and Cernicharo 1990, Bachiller et al. 1991b,c, Bachiller 1996). The EHV flow is considered to be the same as jet due to its velocity and collimated structure characteristics. Molecular outflows are universally observed during the star formation process. On the other hand, there are few examples of observations of jet. The objects, having the EHV flows are extremely rare, and only about 10 samples are currently known (Bachiller and Cernicharo 1990, Bachiller et al. 1991b,a, 2001, Lebrón et al. 2006, Hirano et al. 2010, Gómez-Ruiz et al. 2013, Tafalla et al. 2017, Lee et al. 2017, Matsushita et al. 2019). The jets exist from low mass to massive stars independent of the protostellar mass. In other words, the objects, which have been confirmed to be molecular jets, drive outflow at the same time, and are known as objects that are observed simultaneously with outflow and jet. In Figure 1.4, it can be confirmed from MMS 5/OMC-3 that CO outflow emission and SiO high velocity jet are simultaneously detected.

The jets are normally observed in the CO emission and also detected in the SiO emission. Interestingly, all of the SiO jets are associated with the Class 0 source, which has a timescale of $t \lesssim 10^4$ yr. The jets have a velocity of $|v - v_{\rm sys}| \sim 50$ km s^{-1} to 200 km s^{-1} and exhibit a collimated structure with a few opening angle of $\sim 5^\circ$ to 20° (Gueth et al. 1996, Lebrón et al. 2006, Santiago-García et al. 2009, Hirano et al. 2010, Podio et al. 2015, Matsushita et al. 2019). There are some knotty structures within the collimated jet-like components (Bachiller and Tafalla 1999, Santiago-García et al. 2009, Hirano et al. 2010, Matsushita et al. 2019). In contrast, low velocity molecular outflows also exhibit bipolarity, but have a V-shapes structure and wide opening angles of $30^\circ - 60^\circ$ (Tafalla et al. 2004, 2010, 2017, Hirano et al. 2010, Santiago-García et al. 2009, Matsushita et al. 2019). Figure 1.4 shows that the outflow has a wide opening angle and the jet has a collimated structure. Thus, the jets appear to be surrounded by the low velocity outflow.

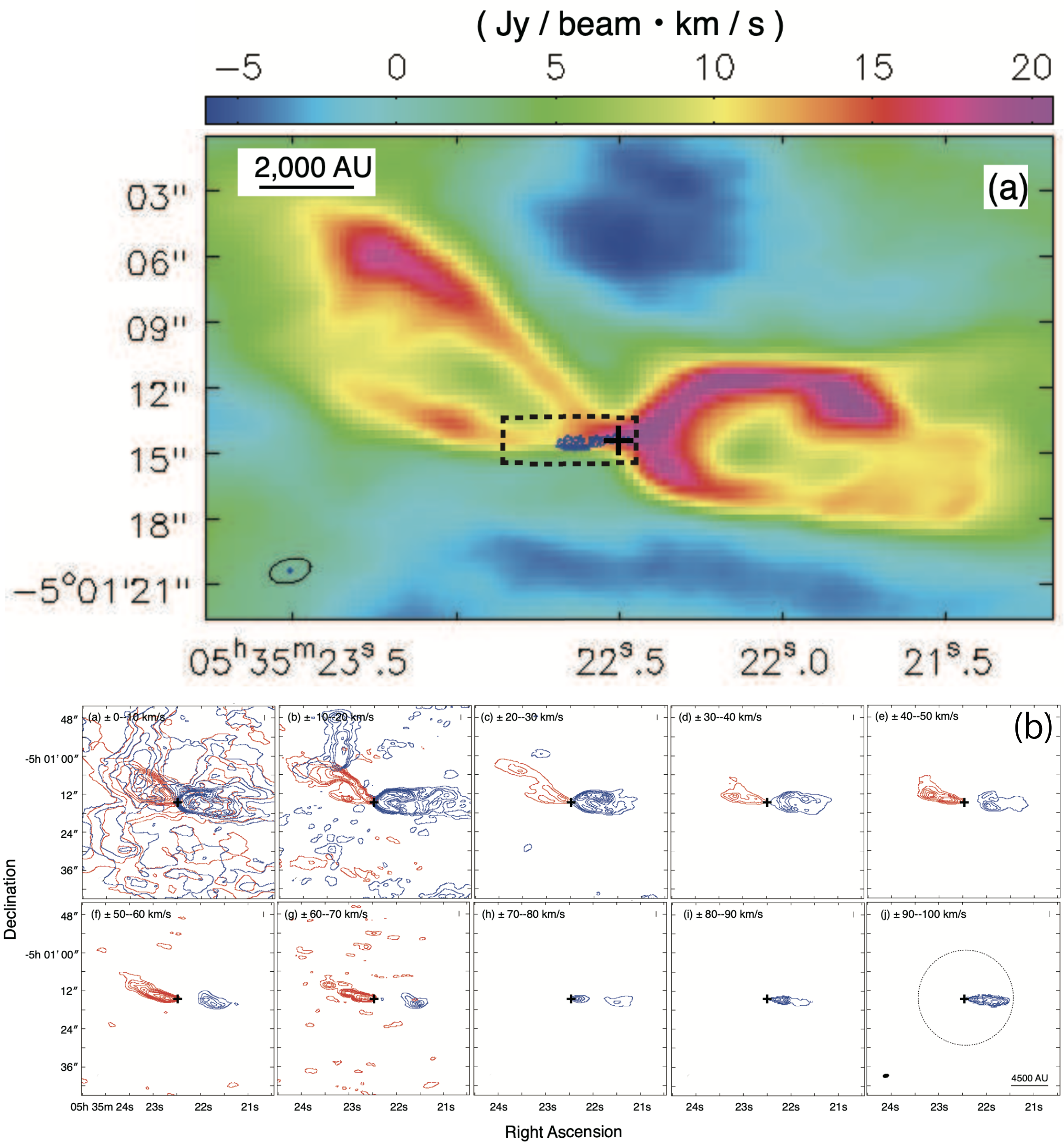

Figure 1.4: (a) In OMC 3, there is the prestellar core, MMS 5. The color shows the CO integrated intensity map and the blue contours show the SiO integrated intensity map. (b) The CO channel maps show the red- and blueshifted emission of low velocity outflows and high velocity jets. These figures are referenced from Matsushita et al. (2019).

1.4 OMC-2/FIR 6 Region

The Orion A is the nearest giant molecular cloud, and includes a large filament extending $\sim$ 7 pc, so-called Integral Shaped Filament (ISF). The observation image of ISF is showed in Figure 1.5 (a) and zooming up the OMC-2 and OMC-3 region is showd in Figure 1.5 (b). The ISF is the host of the most massive cluster in the nearest the active massive star forming region. A few prestellar cores with outflow and jet (EHV flow) were discovered in the filament of OMC-3 (Matsushita et al. 2019) in Orion A. In the Orion A, there is a high possibility that other similar objects which drive the EHV flows exist. Therefore, it is very important to discover outflow, jet and undiscovered protostellar cores in this region in order to understand the early star formation. In addition, it is possible to unveil the star formation process with a hierarchical structure. As described in Section 1.2, the ISF in Orion A is a very good target for studying outflow and jet while elucidating the hierarchical structure from filament to core.

In the OMC-2 region, there are embedded clusters contained with $\sim$ 100 stars (Lada and Lada 2003). FIR 6 region has four millimeter clumps 6a, 6b, 6c and 6d, and only 6d contains a Class II binary MIR source (MIR 31/32) (Nielbock et al. 2003:in Figure 1.6). van Terwisga et al. (2019) showed that the OMC-2 region is observed for the purpose of comparing the disk population in this region with that in other regions. In the observation, there are newly discovered sources such as Spitzer detected sources and non-spitzer sources. In total, 12 sources with ALMA 3 mm dust continuum have been detected in the OMC-2 / FIR 6 region, of which 6 sources are detected for the first time.

Takahashi et al. (2008) and Shimajiri et al. (2009) reported the outflow observation results with ASTE 10 m and Nobeyama Millimeter Array (NMA), respectively. Two clear CO outflows were detected on the four millimeter clumps (FIR 6a to 6d) that have been discovered by (Takahashi et al. 2008:in Figure 1.7). FIR 6b has a bipolar CO J = 3–2 outflow which extends to the northeast to southwest direction, and FIR 6c has a bipolar outflow extending from the north to south direction. These two molecular outflows were not detected in Aso et al. (2000) single-dish observation with CO J = 1–0 emission. Shimajiri et al. (2009) showed that FIR 6b, 6c, and 6d eject molecular outflow with CO J = 1–0 emission. FIR 6d has a clear bipolar structure, and the velocity is in the range of 7.7 km s^{-1} to 12.6 km s^{-1} with the CO J = 1–0 emission. The FIR 6c is also associated with a collimated jet-like component in SiO J = 2–1 emission. The SiO emission of the FIR 6c has two components, one is the blueshifted velocity (-11.7 to 11.0 km s^{-1}) and the other is in the range of 3.4 to 14.2 km s^{-1}.

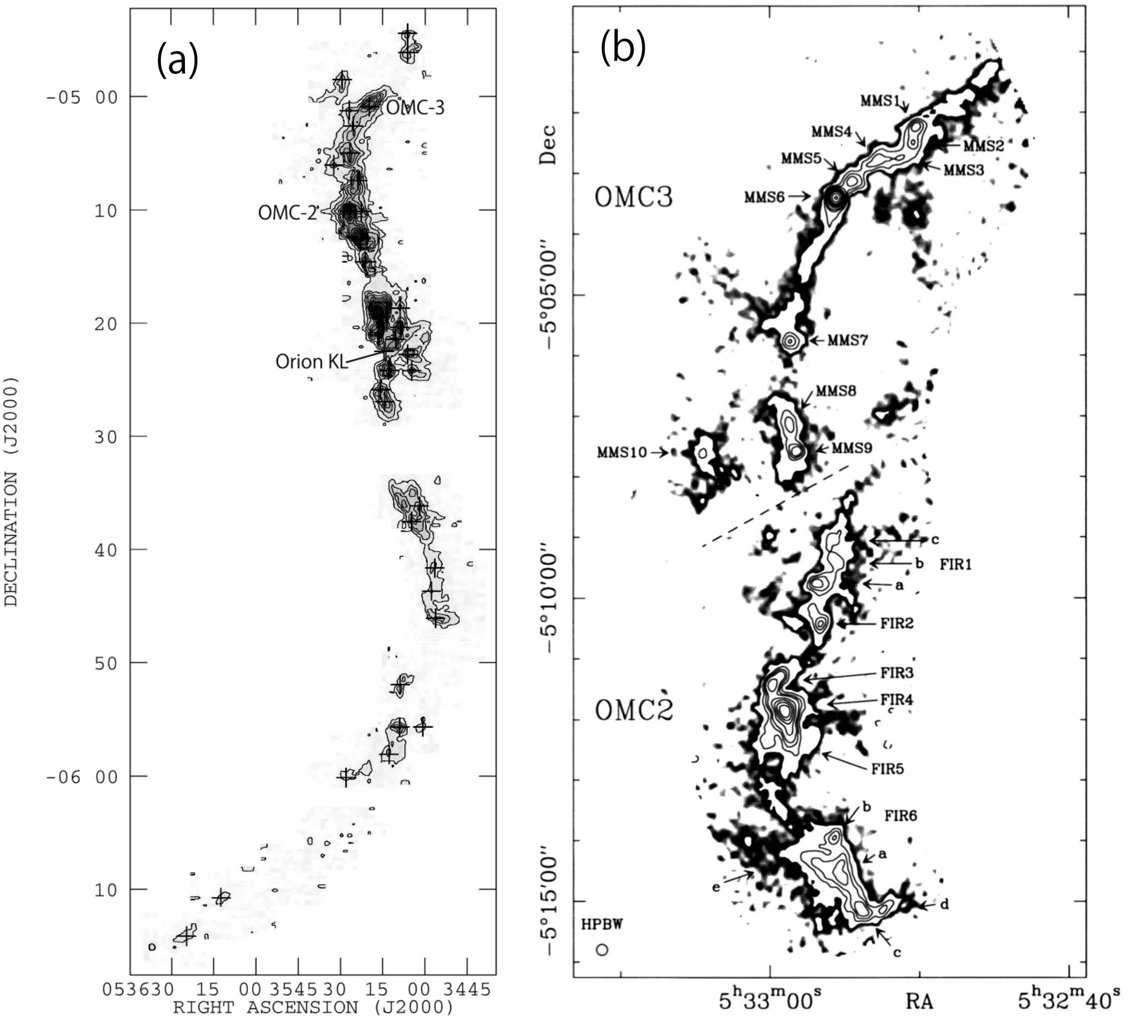

Figure 1.5: (a) The image shows the integrated intensity map of the N_2H^+ image of the Integral Shaped Filament (ISF). This figure is referenced from Tatematsu et al. (2008). In the ISF, the OMC-2, OMC-3 and Orion KL regions are contained. (b) The far-infrared (FIR) observation result at 1300 μm mapped around the OMC-2 and OMC-3 region. This figure is referenced from Chini et al. (1997).

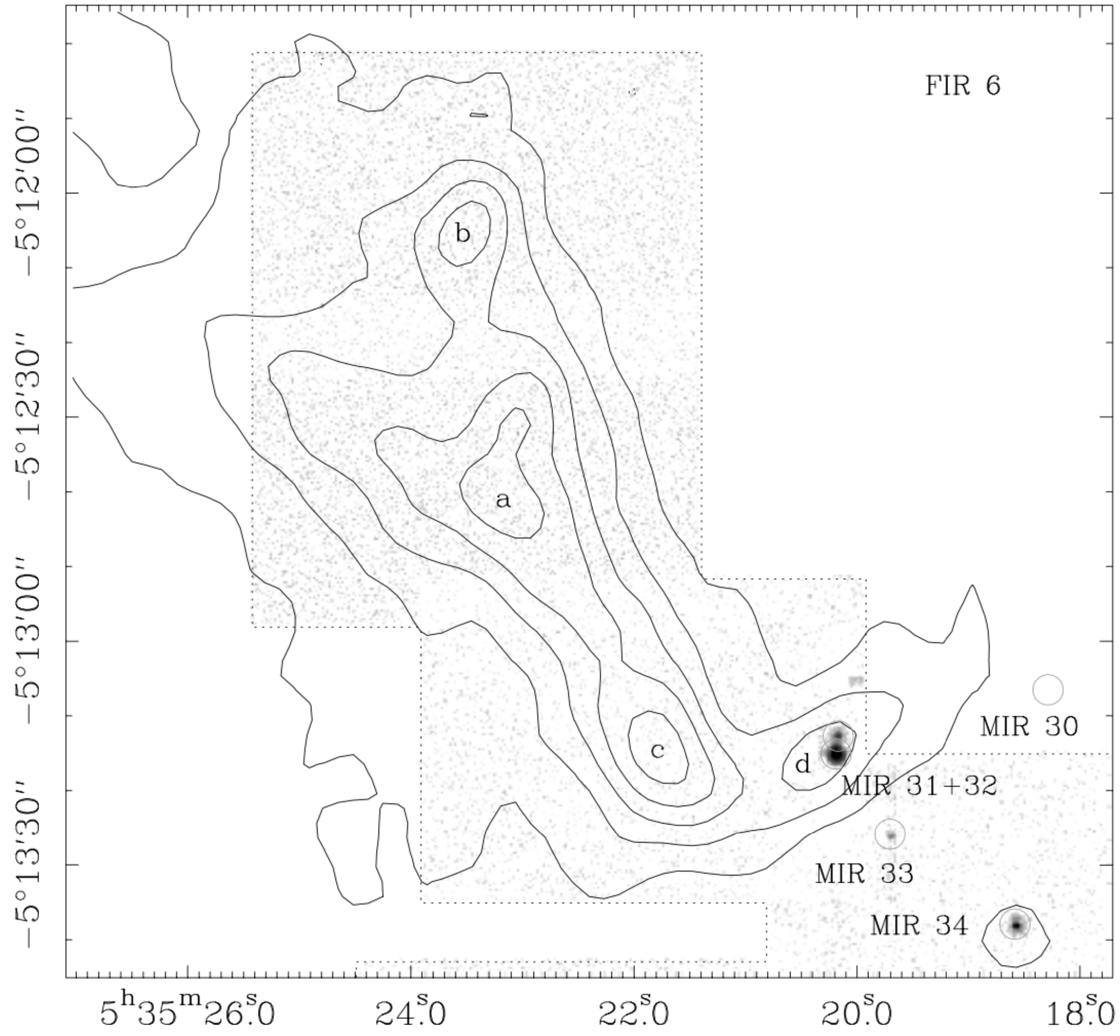

Figure 1.6: The image shows the mid-imfrared (MIR) and mm data around OMC-2/FIR 6 region. The grey scale color shows the results of the TIMMI 2. This figure is referenced from Nielbock et al. (2003).

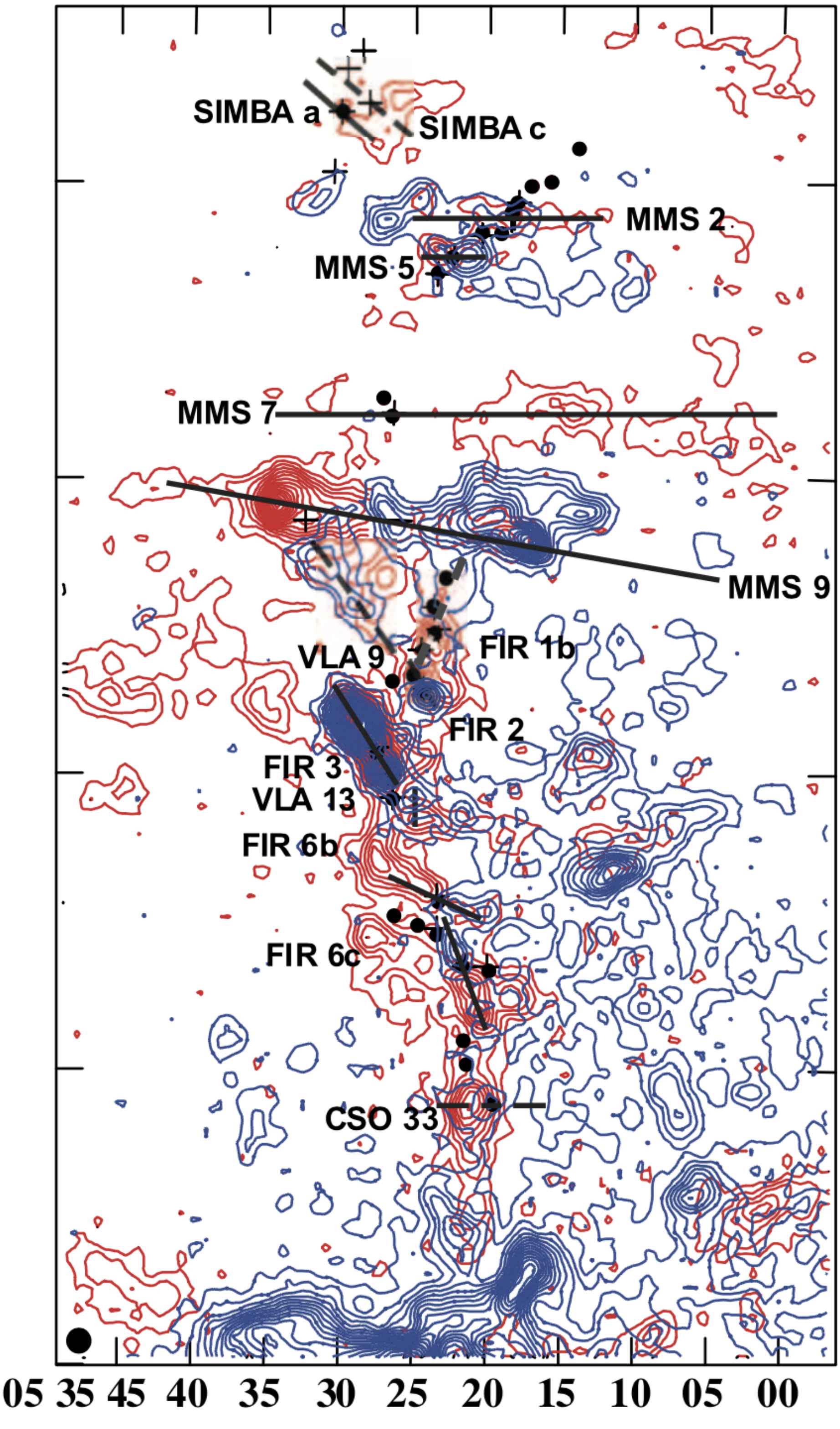

Figure 1.7: The intensity map of the CO J = 3–2 with the ASTE. The contours show the blue and red-shifted emission and the velocity range is $v_{\rm lsr}$ = -6.2 to 7.8 km s^{-1} and $v_{\rm lsr}$ = 14.3 to 27.3 km s^{-1}, respectively. This figure is referenced from Takahashi et al. (2008).

I describe the observation in Section 2. In Section 3, I demonstrate my results about OMC-2/FIR 6. Discussions section is 4, and Section 5 summarizes the paper.

Chapter 2

OBSERVATION

The ALMA 12m array observation was performed at 2019 April 19 and ACA 7m array (Morita array) observations were performed at 2018 January 7, 10, 11 and 17 toward the OMC-2/FIR 6 (center of this region: R.A. = $05^h35^m21^s.700$, Dec = $-05°12'51''.000$) in Integral Shaped Filament (ISF) with mosaic. The distance of my target is $d \sim 388$ pc (Kounkel et al. 2017). In Table 2.1, observational parameters are summarized. The data are 1.3 mm ALMA Band-6 continuum and two molecular lines, CO (J = 2–1; 231.207 GHz) and SiO (J = 5–4; 217.105 GHz), which were taken as part of observation program 2017.1.01353.S (PI: S. Takahashi). On source time per field was 1.2 minutes for the ACA 7m array with 45 points in total, and 2.2 minutes for the ALMA 12m array with 110 points in total, respectively. The ALMA correlator was configured to provide two independent spectral windows. The spectral windows

Table 2.1: ALMA Observing Parameters

Parameters	ACA 7 m-Array	12 m-array
Observation date (YYYY-MM-DD)	2018-01-07, 2018-01-10, 2018-01-11 and 2018-01-17	2019-04-19
Number of antennas	11	44
Phase center (ICRS)	$05^h35^m21^s.7000$, $-05°12'51''.000$	
Primary beam size (arcsec)	43.2	25.2
Continuum representative frequency (GHz)	230.532	
Continuum effective bandwidth (GHz)	5.88	
CO J=2–1 and SiO J=5–4 imaging velocity resolution (km s^{-1}) [1]	2.5	
Projected baseline coverage (m)	7–48	12–500
Maximum recoverable size (arcsec)	29.2	7.0
On-source time per field (minutes)	1.2	2.2
System temperature (K)	60–210	70–180
Flux calibrator	J0522-3627	J0423-0120
Gain calibrator	J0607-0834, J0542-0913	J0541-0211
Bandpass calibrator	J0522-3627	J0423-0120

Table 2.2: Summary of the image parameters for each figure

Data set	Configuration	Synthesized beam [arcsec, deg]	Noise level
1.3mm continuum	ACA+12m-array	4.5 × 2.5, -83	0.5 [mJy beam^{-1}]
CO J=2–1	ACA+12m-array	4.5 × 2.5, -87	15 [mJy beam^{-1} $\cdot$ km s^{-1}]
SiO J=5–4	ACA+12m-array	4.7 × 2.6, -87	13 [mJy beam^{-1} $\cdot$ km s^{-1}]

---

[1] Values listed in the table are imaging velocity resolution. The original velocity resolution used for the observations is mentioned in Section 2.

assigned to CO $J = 2$–1 and SiO $J = 5$–4 have a bandwidth of 1875.00 MHz, and the spectral resolutions are 976.563 kHz and 31.250 MHz, respectively. The velocity resolutions achieved 1.27 km s^{-1} for CO J = 2–1 and 43.156 km s^{-1} for SiO J = 5-4. The continuum images are produced by the channels of no detection with the molecular line emission. The effective bandwidth for the continuum emissions is approximately 5.9 GHz, after subtraction of the line emissions.

Calibration of the raw visibility data was performed by using the Common Astronomy Software Application (CASA: McMullin et al. 2007) with version 5.4.0. For both the continuum and molecular line imaging, robust weighting with Briggs parameter = 0.5 was used. As a data set, I firstly combined the visibility data of ACA 7m array and ALMA 12m array configurations using the CASA concat task. From the combined visibility, I created a final image using t-CLEANed task. In the final images, the beam size is $\sim$ 4 arcsec, and the noise level is 0.5 mJy beam^{-1} for continuum image and 15 mJy $\text{beam}^{-1} \cdot \text{km s}^{-1}$ with $\Delta v = 2.5$ km s^{-1} for CO J = 2–1 line images and 13 mJy $\text{beam}^{-1} \cdot \text{km s}^{-1}$ with $\Delta v = 43$ km s^{-1} for SiO J = 5–4 images. Sensitivity in this observation is 0.48 mJy beam^{-1}, and mass sensitivity is 9.27×10^{-3} $M_\odot$ at 5 σ, and there is enough sensitivity for detecting fragmentation in brown-dwarf mass scale. Compared to previous observations, my observation can detect many compact structures. The achieved synthesized beam and noise levels are summarized in Table 2.2.

Chapter 3

RESULTS

3.1 Search for the newly sources/cores in OMC-2/FIR 6

3.1.1 1.3 mm Continuum

Figure 3.1 shows the result of this ALMA observation at Orion Molecular Cloud-2/Far Infrared source 6 (OMC-2/FIR 6). For the image of ALMA observation, I combined ACA data with ALMA 12m observation data using CASA concat task with weight 20:1. There is a filament structure in the region of OMC-2/FIR 6. In addition, there are several cores and clumps in the filament. In the ALMA observation, filaments seems to have the same shape as those seen in the previous studies. The filament extends to approximately 0.24 pc ($\sim$ 2') in the north-south direction, and is divided into two parts around the center of the filament. The thickness of the filament is approximately 0.02 pc ($\sim$ 10").

Two methods were used to identify astronomical objects. (1) Using Dendrogram (Rosolowsky et al. 2008), I set the minimum contour to 8 σ and the contour step size to 3 σ. The sources are detected and total flux and peak flux are measured, with this setting. (2) Using CASA, the minimum contour is set to 5 σ, the step size of contour is set to 5 σ, and two or more contours that can be confirmed are identified as sources. I used CASA imfit task, in which 2D Gaussian fitting was performed for each candidate source, and total flux and peak flux were measured. The results of (1) and (2) are shown in Figure 3.1 and Figure 3.2. Figure 3.1 shows the diagram describing the ID numbers in the image of the observation result of ALMA and overlaid the contour started at 5 σ (1 $\sigma \sim$ 0.5 mJy). Figure 3.2 shows the results of source identification using Dendrogram. As a result of these analysis, I discovered 21 sources and assigned ID number to these sources. From Figure 3.4 to Figure 3.7, I plotted an enlarged image of the region where the candidate object of the core of OMC-2/FIR 6 was found. The black symbol shown in the figure corresponds to the peak flux position of each source. I summarized correspondence with source ID determined by CASA, source ID determined by Dendrogram, continuum peak flux position, integrated flux, peak flux, 1.3 mm dust mass, previous infrared observation results in Table 3.1. In addition, I also described the source identification and classification in previous studies. Regarding Outflow/Jet, the emissions detected with CO or SiO in the previous observations are shown. I measured the integrated flux and peak flux using the Dendrogram values. In Table 3.2, I described the summary and comparison of the values measured by CASA and Dendrogram. As listed in Table 3.2, and there is significant difference between CASA results and Dendrogram results. Therefore, the integrated flux value that was mechanically processed by Dendrogram was adopted.

Moreover, I calculated the dust continuum mass of each source using the integrated flux value measured by Dendrogram. The dust mass of the envelope/disk traced by the 1.3 mm continuum emission ($M_{1.3\mathrm{mm}}$) can be estimated as

$$M_{1.3\mathrm{mm}} = \frac{F_{1.3\mathrm{mm}} d^2}{\kappa_{1.3\mathrm{mm}} B_{1.3\mathrm{mm}}(T_{\mathrm{dust}})}, \tag{3.1}$$

where $F_{1.3\mathrm{mm}}$ is the total integrated 1.3 mm flux, d is the distance to the source from the earth, $\kappa_{1.3\mathrm{mm}}$ is the dust mass opacity at $\lambda = 1.3$ mm, T_{dust} is the dust temperature, and $B_{1.3\mathrm{mm}}(T_{\mathrm{dust}})$ is the Planck function at a temperature of T_{dust}. I adopted the dust opacity of $\kappa_{1.3\mathrm{mm}} = 0.037\ \mathrm{cm}^2\mathrm{g}^{-1}\ (\lambda/400\ \mu\mathrm{m})^{-\beta}$ (Keene et al. 1982), $\beta = 2$ (Johnstone and Bally 1999, Sadavoy et al. 2016) and the dust temperature of $T_{\mathrm{dust}} = 25$ K (Cesaroni and Wilson 1994, Chini et al. 1997, Tatematsu et al. 2008, Lombardi et al. 2015). I assumed a gas-to-dust mass ratio of 100. Here, T_{dust} of 25 K was also adopted, because Lombardi et al. (2015) shows $T_{\mathrm{dust}} \sim 20$ to 30 K and an average value of 25 K. Table 3.1 and Table 3.2 show the results of dust continuum mass using T $\sim$ 25 K. The dust mass of each temperature is summarized in Table 3.3. Comparing the calculation using 20 K or 30 K with the calculation results at 25 K, the change in the dust mass is only 0.2 $\sim$ 0.3 %. The 1.3 mm continuum source mass is estimated to be in the range of 0.0196 to 0.861 $M_{\odot}$.

Table 3.1 shows the results of previous studies of the infrared observation (Chini et al. 1997, Lis et al. 1998, Nielbock et al. 2003, Furlan et al. 2016), in which the latest ALMA observations (van Terwisga et al. 2019) are also summarized. The top right of Figure 3.3 shows the image of this ALMA observation data overlaid on the position of the HOPS objects detected by Herschel telescope. In the figure, all the infrared and far infrared sources coincide with the continuum peak positions observed by ALMA. The infrared observation taken from the Herschel telescope has identified 10 objects in OMC-2 / FIR 6. My ALMA Band 6 observations discovered 21 objects. The infrared detection rate is $\sim$ 47.6 %. In the observation, there are many detected sources that are not observed in infrared wavelength. They are only visible with ALMA. Thus, FIR 6/OMC-2 is a very young star forming region and there exists a high possibility to detect many starless cores.

In van Terwisga et al. (2019), which is the latest ALMA observation, 11 sources were observed in ALMA 3 mm continuum observation. The bottom left of Figure3.3 is a plot of these objects superimposed on my ALMA observations. In the observation of van Terwisga et al. (2019), the sources with IDs starting from U are not observed in the Spitzer telescope. They were discovered for the first time (van Terwisga et al. 2019). Although only the source U22 was not seen in my observations, all the remaining sources were observed. In addition to those sources, my observations have discovered 10 new sources. On the other hand, the objects observed by 2MASS with Near Infrared (NIR) (Carpenter et al. 2001) are shown in the bottom right panel in Figure 3.3. These four NIR objects with the red letter in Figure 3.3 can not identify in Furlan et al. (2016) and van Terwisga et al. (2019). These four objects are only observed by NIR but not by IR, FIR, and radio wavelength. Therefore, it is considered that the star formation process has already done and the gas is dissipated.

Table 3.1: Source List

ID	Dendrogram ID	RA	Dec	integrated flux [mJy]	peak flux [mJy/beam]	mass[1] [$M_\odot$]	HOPS[2]	FIR[3]	MIR[4]	CSO[5]	ALMA[6]	Class[2]	Outflow[7]
FIR 6 – ALMA 1	28	05:35:24.698	-5.11.30.186	5.07	7.21	0.0196	62	...	...	...	P20	flat	...
FIR 6 – ALMA 2	27	05:35:26.841	-5.11.39.4679	6.48	6.11	0.0250	...	...	...	...	...	...	...
FIR 6 – ALMA 3[9]	...	05:35:26.919	-5.11.44.3164	...	...	...	...	...	...	...	...	...	...
FIR 6 – ALMA 4	26	05:35:23.055	-5.11.50.8168	17.0	9.81	0.0657	...	...	...	...	U12	...	...
FIR 6 – ALMA 5	25	05:35:23.343	-5.12.03.9702	219	122	0.846	60	6b	29	25	P3	0	CO
FIR 6 – ALMA 6	23	05:35:22.806	-5.12.27.399	93.5	51.1	0.361	...	6a[8]	32[8]	...	U5	starless[8]	...
FIR 6 – ALMA 7	24	05:35:25.200	-5.12.22.3590	23.0	13.3	0.0888	...	...	...	...	...	...	...
FIR 6 – ALMA 8	22	05:35:24.214	-5.12.33.9064	17.6	16.5	0.0680	...	...	...	...	...	...	...
FIR 6 – ALMA 9	21	05:35:23.858	-5.12.38.3425	14.0	16.4	0.0541	...	...	...	...	...	...	...
FIR 6 – ALMA 10	19	05:35:22.898	-5.12.42.297	223	27.3	0.861	...	6a[8]	33[8]	...	U19	starless[8]	...
FIR 6 – ALMA 11	17	05:35:21.326	-5.12.59.8310	8.55	8.90	0.0330	...	...	...	...	...	...	...
FIR 6 – ALMA 12	13	05:35:21.778	-5.13.12.328	46.7	34.1	0.180	...	6c[8]	35[8]	...	U15	starless[8]	...
FIR 6 – ALMA 13	10	05:35:21.421	-5.13.18.145	105	86.7	0.406	409	6c	...	...	U1	0	CO/SiO
FIR 6 – ALMA 14	6	05:35:20.807	-5.13.22.959	33.2	26.9	0.128	...	6c[8]	38[8]	...	P14	starless[8]	...
FIR 6 – ALMA 15	12	05:35:20.195	-5.13.16.1724	161	129	0.622	59	6d	31, 32	30	U22, P2	flat	CO
FIR 6 – ALMA 16	14	05:35:19.681	-5.13.09.775	19.7	15.3	0.0761	...	...	...	...	...	...	...
FIR 6 – ALMA 17	15	05:35:18.260	-5.13.06.6104	27.7	27.1	0.107	...	...	30	...	P11	...	...
FIR 6 – ALMA 18	2	05:35:18.530	-5.13.38.756	53.0	34.9	0.205	58	...	34	...	D3	flat	...
FIR 6 – ALMA 19[10]	1	05:35:19.331	-5.14.08.0016	14.2	5.57	0.0549	...	...	...	...	...	...	...
FIR 6 – ALMA 20[10]	1	05:35:19.299	-5.14.12.0139	14.2	5.57	0.0549	...	...	...	...	...	...	...
FIR 6 – ALMA 21	0	05:35:19.054	-5.14.19.6951	10.0	5.48	0.0386	...	...	...	...	...	...	...

---

[1] The flux obtained by Dendrogram was used in the calculation. T∼ 25 K is adopted.

[2] Furlan et al. (2016)

[3] Chini et al. (1997)

[4] Nielbock et al. (2003)

[5] Lis et al. (1998)

[6] S.E. van Terwisga et al. (2019). D is the object with the disk. P is the object detected protostar. U is the objects not included in the Spitzer catalog.

[7] Takahashi et al. (2008), Shimajiri et al. (2009)

[8] Kainulainen et al. (2017)

[9] No detected by Dendrogram.

[10] Dendrogram doesn't distinguish 19 and 20 as a different sources and I used same data is described for 19 and 20.

Table 3.2: Flux compareed with Dendrogram and CASA

Dendrogram ID	integrated flux [mJy]	peak flux [mJy/beam]	FIR 6 – ALMA ID	integrated flux [mJy]	peak flux [mJy/beam]	mass $[M_\odot]$[1]
0	10.04	5.48	21	32.5	5.31	0.0515
1	14.21	5.57	19, 20	28, 22.72	5.47, 5.14	0.0729
2	53.02	34.9	18	51.0	32.3	0.272
6	33.23	26.9	14	65.3	23.8	0.170
10	105.0	86.7	13	184	73.2	0.538
12	161.4	129	15	165.9	124.4	0.828
13	46.65	34.1	12	394	32.1	0.239
14	19.72	15.3	16	96.9	14.0	0.10
15	27.72	27.1	17	32.0	27.2	0.142
17	8.551	8.90	11	41.0	8.78	0.0438
19	222.5	27.3	10	800	24.4	1.14
21	13.96	16.4	9	96.6	16.4	0.072
22	17.56	16.5	8	137	16.2	0.090
23	93.48	51.1	6	151	45.2	0.479
24	22.98	13.3	7	61.9	13.3	0.118
25	218.8	122	5	172	114	1.12
26	16.98	9.81	4	23.7	9.51	0.0871
27	6.479	6.11	2	15.99	5.81	0.0332
28	5.070	7.21	1	15.9	5.76	0.0260

---

[1] The flux obtained by Dendrogram was used in the calculation. T$\sim$ 25 K is adopted.

Table 3.3: Compering of Mass for 20 K, 25 K, 30 K

ID	mass [$M_\odot$] (20 K)	mass [$M_\odot$] (25 K)	mass [$M_\odot$] (30 K)
FIR 6 – ALMA 1	0.0260	0.0196	0.0157
FIR 6 – ALMA 2	0.0332	0.0250	0.0201
FIR 6 – ALMA 3			
FIR 6 – ALMA 4	0.0871	0.0657	0.0526
FIR 6 – ALMA 5	1.12	0.846	0.678
FIR 6 – ALMA 6	0.479	0.361	0.289
FIR 6 – ALMA 7	0.118	0.0888	0.0712
FIR 6 – ALMA 8	0.090	0.0680	0.0545
FIR 6 – ALMA 9	0.072	0.0541	0.0433
FIR 6 – ALMA 10	1.14	0.861	0.690
FIR 6 – ALMA 11	0.0438	0.0330	0.0265
FIR 6 – ALMA 12	0.239	0.180	0.145
FIR 6 – ALMA 13	0.538	0.406	0.325
FIR 6 – ALMA 14	0.170	0.128	0.103
FIR 6 – ALMA 15	0.828	0.622	0.498
FIR 6 – ALMA 16	0.10	0.0761	0.0610
FIR 6 – ALMA 17	0.142	0.107	0.0857
FIR 6 – ALMA 18	0.272	0.205	0.164
FIR 6 – ALMA 19	0.0729	0.0549	0.0439
FIR 6 – ALMA 20	0.0729	0.0549	0.0439
FIR 6 – ALMA 21	0.0515	0.0386	0.0309

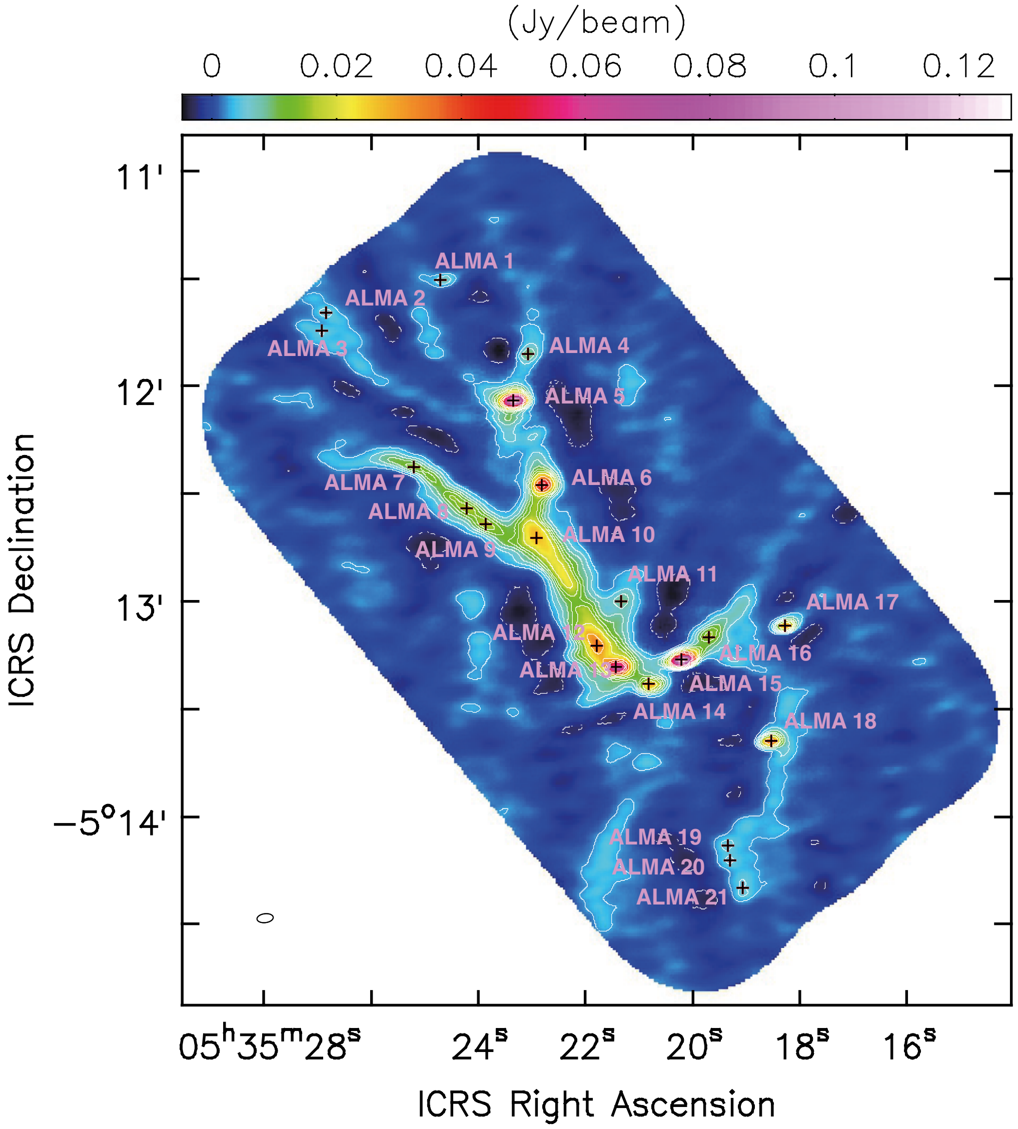

Figure 3.1: The 1.3 mm continuum image combined with ALMA 12m and ACA. The contour level starts at 5σ, [-5, 5, 10, 15, 20, 25, 30, 40, 60, 80, 100] (1σ for the continuum image is 0.5 mJy beam^{-1}.) The beam size is indicated by a circle in each panel.

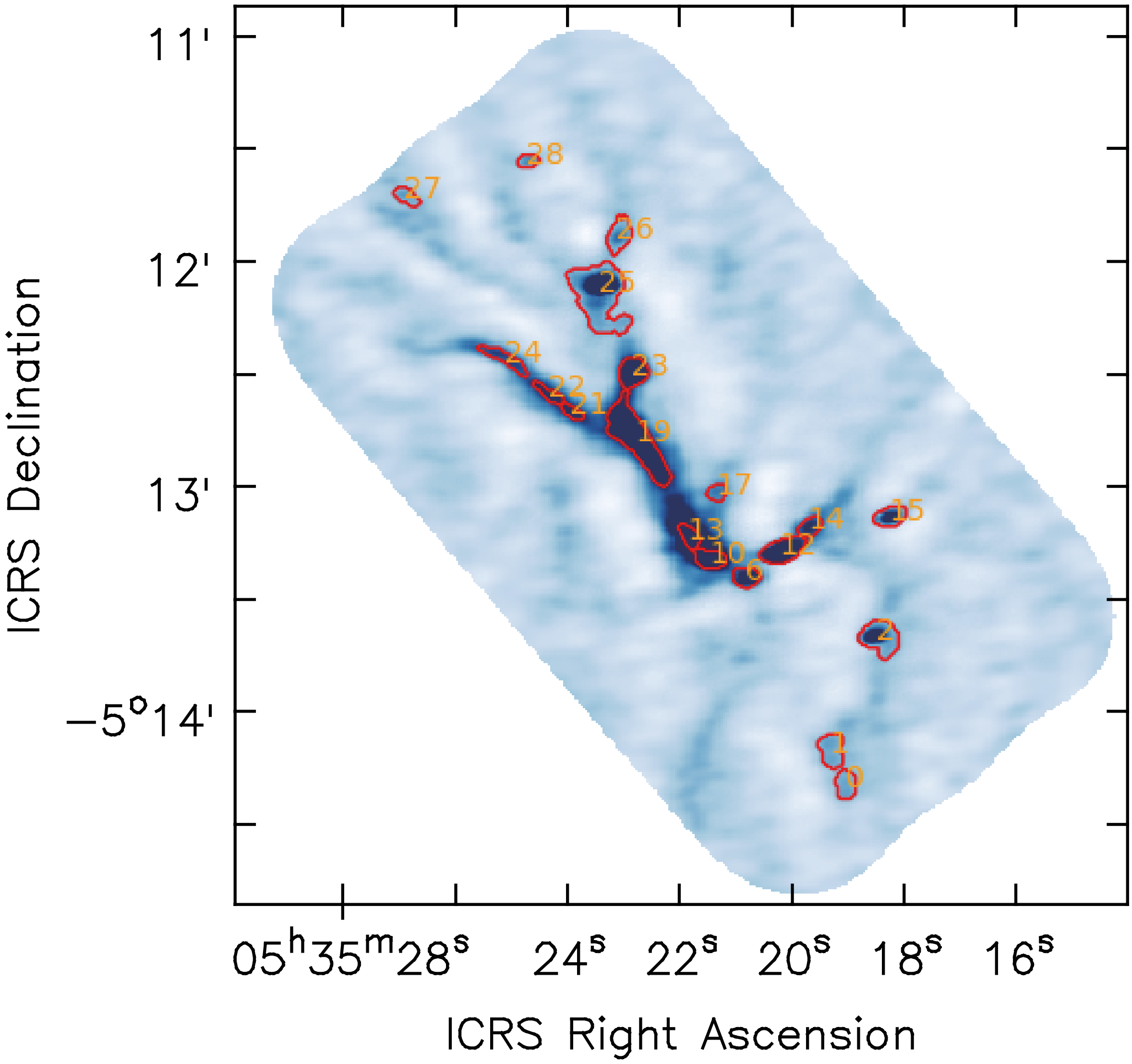

Figure 3.2: This panel is Dendrogram image with the red contour starts at 8σ with 3σ interval (1σ for the continuum image is 0.5 mJy beam^{-1}.), overlaid ID by Dendrogram.

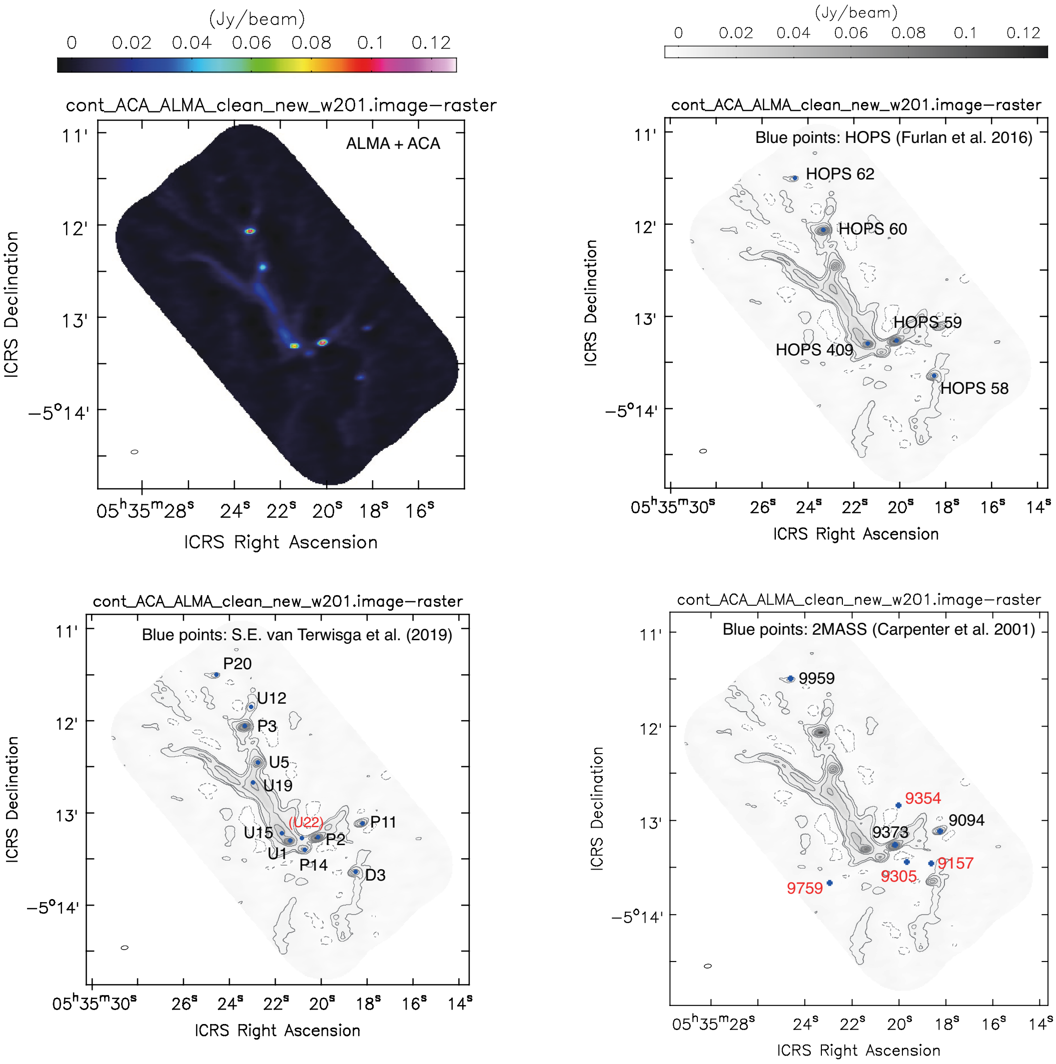

Figure 3.3: Top left panel is 1.3 mm continuum color image combined with ALMA 12m and ACA. Top right panel is 1.3 mm continuum contour map overlaid HOPS position (Furlan et al. 2016). Bottom left panel is 1.3 mm continuum contour map overlaid latest ALMA observation position (van Terwisga et al. 2019). Bottom right panel is 1.3 mm continuum contour map overlaid 2MASS position (Carpenter et al. 2001). The contour level starts at 5σ, [-5, 5, 10, 25, 50, 75, 100] (1σ for the continuum image is 0.5 mJy beam^{-1}.) The beam size is indicated by a circle in each panel.

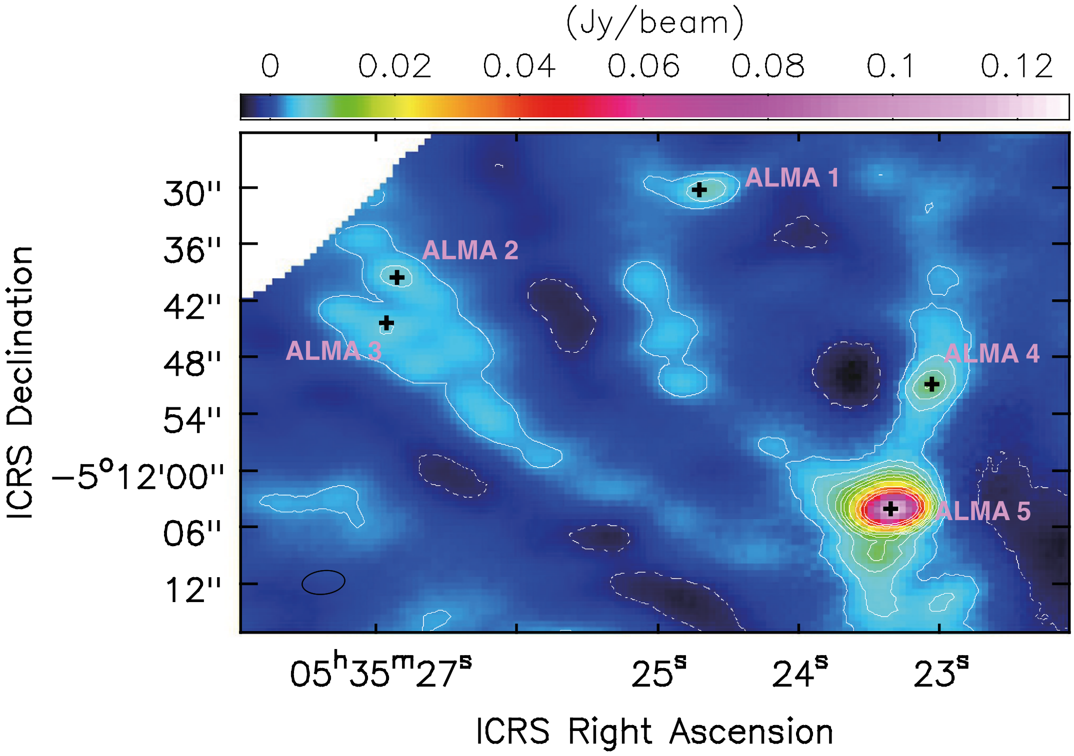

Figure 3.4: This panel is 1.3 mm continuum combined with ALMA 12m and ACA enlarged image of the region of FIR 6 – ALMA 1 to FIR 6 – ALMA 5. The contour level starts at 5σ, [-5, 5, 10, 15, 20, 25, 30, 40, 60, 80, 100] (1σ for the continuum image is 0.5 mJy beam^{-1}.) The beam size is indicated by a circle in each panel.

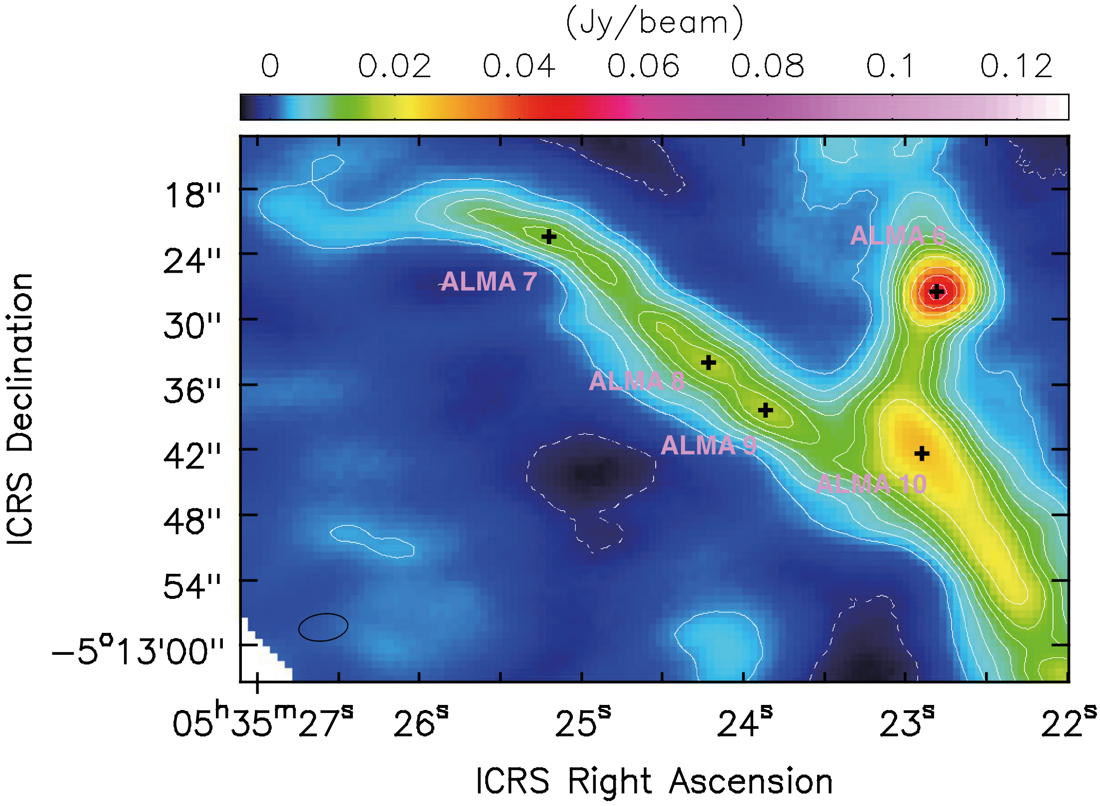

Figure 3.5: This panel is 1.3 mm continuum combined with ALMA 12m and ACA enlarged image of the region of FIR 6 – ALMA 6 to FIR 6 – ALMA 10. The contour level starts at 5σ, [-5, 5, 10, 15, 20, 25, 30, 40, 60, 80, 100] (1σ for the continuum image is 0.5 mJy beam^{-1}.) The beam size is indicated by a circle in each panel.

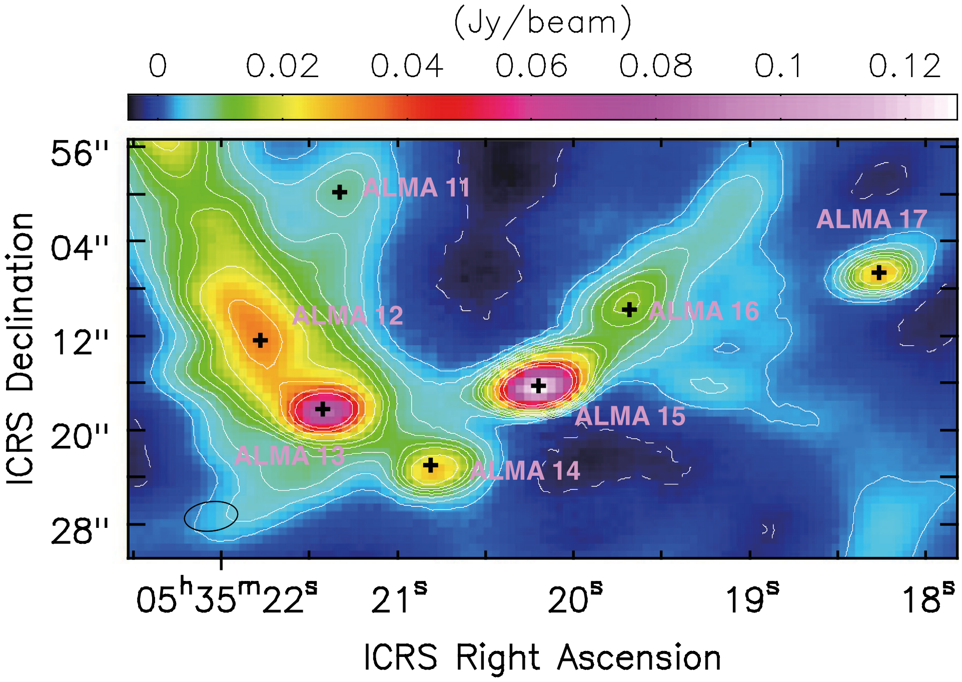

Figure 3.6: This panel is 1.3 mm continuum combined with ALMA 12m and ACA enlarged image of the region of FIR 6 – ALMA 11 to FIR 6 – ALMA 17. The contour level starts at 5σ, [-5, 5, 10, 15, 20, 25, 30, 40, 60, 80, 100] (1σ for the continuum image is 0.5 mJy beam^{-1}.) The beam size is indicated by a circle in each panel.

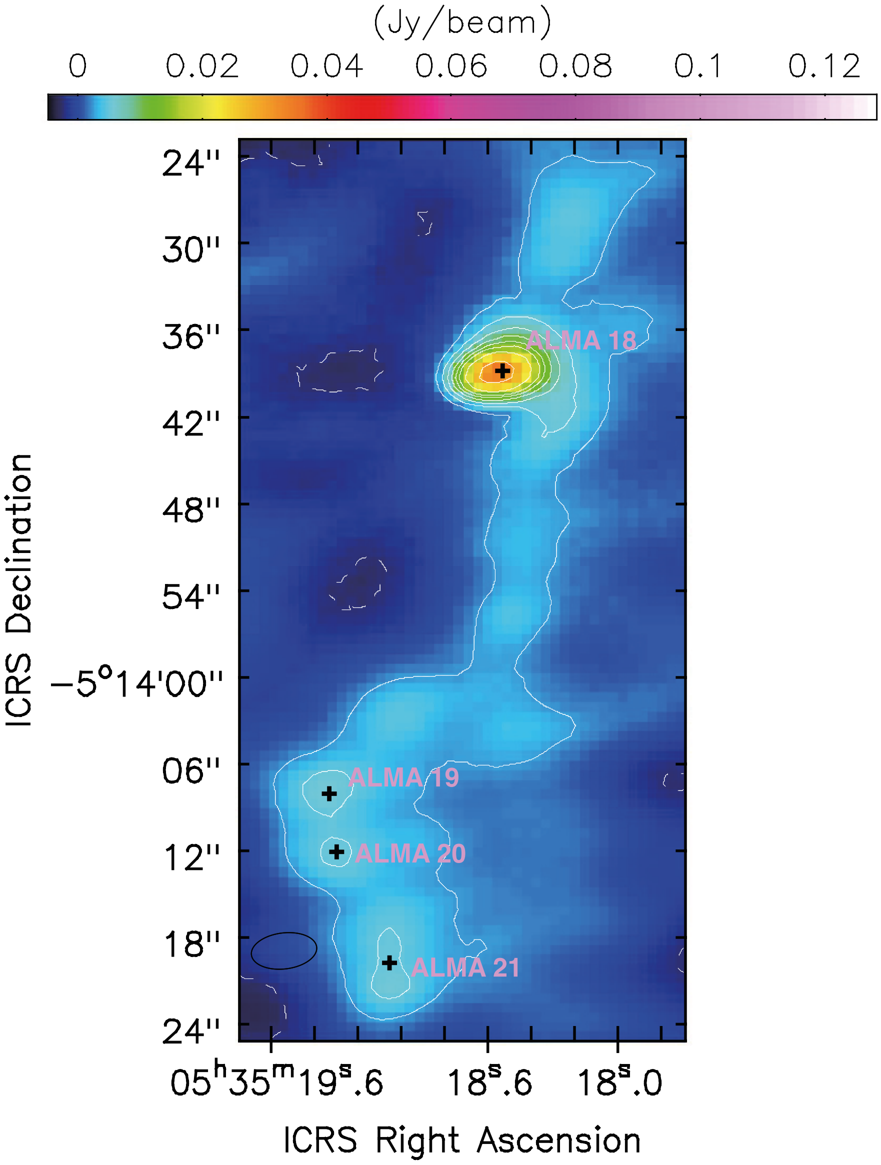

Figure 3.7: This panel is 1.3 mm continuum combined with ALMA 12m and ACA enlarged image of the region of FIR 6 – ALMA 18 to FIR 6 – ALMA 21. The contour level starts at 5σ, [-5, 5, 10, 15, 20, 25, 30, 40, 60, 80, 100] (1σ for the continuum image is 0.5 mJy beam^{-1}.) The beam size is indicated by a circle in each panel.

3.2 Search for Outflow and Jet in OMC-2/FIR 6

3.2.1 CO outflow

In the OMC-2 / FIR 6 region, I investigated whether outflows and/or jets were driven from the cores identified in Section 3.1. In this chapter, I will describe the observation for outflow and jet. I described the conditions for determining the outflow: (i) Observed predominantly above 5 σ, (ii) Bipolar blowing from identified core, (iii) $v_{\rm sys} \sim 11$ km s^{-1} and the existense of the blueshifted and redshifted components. In Ikeda et al. (2007), H^{13}CO^{+} $J = 1$–0 emission was detected from 9.8 km s^{-1} to 11.9 km s^{-1}. Therefore, I adopted the median velocity of $\sim$ 11 km s^{-1} as the system velocity. Figure 3.8 shows the CO $J = 2$–1 moment 0 (Integrated Intensity) map in the velocity range of -9 km s^{-1} to 30 km s^{-1}. Note that the data around the system velocity in the range of 9 km s^{-1} to 13 km s^{-1} is excluded. Figure 3.9 shows the CO $J = 2$–1 moment map in the range of -100 km s^{-1} to -62.5 km s^{-1} and 32.5 km s^{-1} to 97.5 km s^{-1}. The contours started at 5 σ and described every 5 σ in Figure 3.8 and Figure 3.9. Figure 3.8 shows the low velocity moment 0 map in which the low velocity outflow is driven from FIR 6 – ALMA 5, FIR – ALMA 13 and FIR – ALMA 18. The Extremely High Velocity (EHV) flow (hereinafter jet) are confirmed only in FIR 6 – ALMA 5, and the clear knot structures are also confirmed within the jets (Figure 3.9). Figure 3.10 shows the moment 1 (velocity) map of OMC-2/FIR 6. The redshifted and blushifted velocity components from the system velocity can be remarkably confirmed from the moment 1 map. FIR 6 – ALMA 5 and FIR 6 – ALMA 13 clearly show redshifted and blueshifted bipolar outflow. The complexity seen in the CO line emission is attributed to the contamination from the ambient molecular cloud. In the vicinity of the system velocity, many components can be seen in CO line emission. Because the structures are complicated, it is difficult to determine whether outflow is driven. Note that, for details, see 10 $\sim$ 13 km s^{-1} vicinity of all CO channel maps Figure A.1 to Figure A.8, and Figure A.9 to Figure A.22 in Appendix. Therefore, in the moment 0 map (Figures 3.8 and 3.9), the imaging is performed except for $v_{\rm sys}$. FIR 6 – ALMA 1, FIR 6 – ALMA 12, FIR 6 – ALMA 14, FIR 6 – ALMA 15, FIR 6 – ALMA 16, FIR 6 – ALMA 17 have possibility to drive CO outflow. Hereafter, I will describe the sources which outflow/jet is likely to drive in detail. Table 3.4 describes the components that seem to have outflows in the cores observed. There are five sources that have clearly show outflow in the counter part. Considering outflows on only one side of the red or blue shift (non-bipolar outflow), 9 sources have been identified in total. Therefore, in the OMC-2/FIR 6 region, the outflow detection rate is 5/21 $\sim$ 24 % (9/21 $\sim$ 43 %).

---

[1] Takahashi et al. (2008); Shimajiri et al. (2009)

Table 3.4: CO Outflow Candidate

ID	$v_{\rm blue}$ [km s^{-1}]	$v_{\rm red}$ [km s^{-1}]	$R_{\rm blue}$ [pc]	$R_{\rm red}$ [pc]	P.A. [deg]	SiO	Previous study[1]
FIR 6 – ALMA 1	-5 – 8	14 – 17	0.03	0.03	150	no	no
FIR 6 – ALMA 5	-10 – 7.5	12.5 – 37.5	0.12	0.12	70 (blue), 60 (red)	no	yes
FIR 6 – ALMA 5 (EHV)	-87.5 – -62.5	40 – 95	0.04	0.12	60 (blue), 60 (red)	no	no
FIR 6 – ALMA 12		16 – 19		0.02	115	no	no
FIR 6 – ALMA 13	-15 – 7.5	12.5 – 35	0.22	0.15	20	yes	yes
FIR 6 – ALMA 14		16 – 19		0.05	60	no	no
FIR 6 – ALMA 15	4 – 6		0.03		120	no	yes
FIR 6 – ALMA 16	3 –6		0.02		115	no	no
FIR 6 – ALMA 17	5 –8	15 – 19	0.01	0.036	140	no	no
FIR 6 – ALMA 18	-9 – 7	16 – 30	0.044	0.016	130	no	no

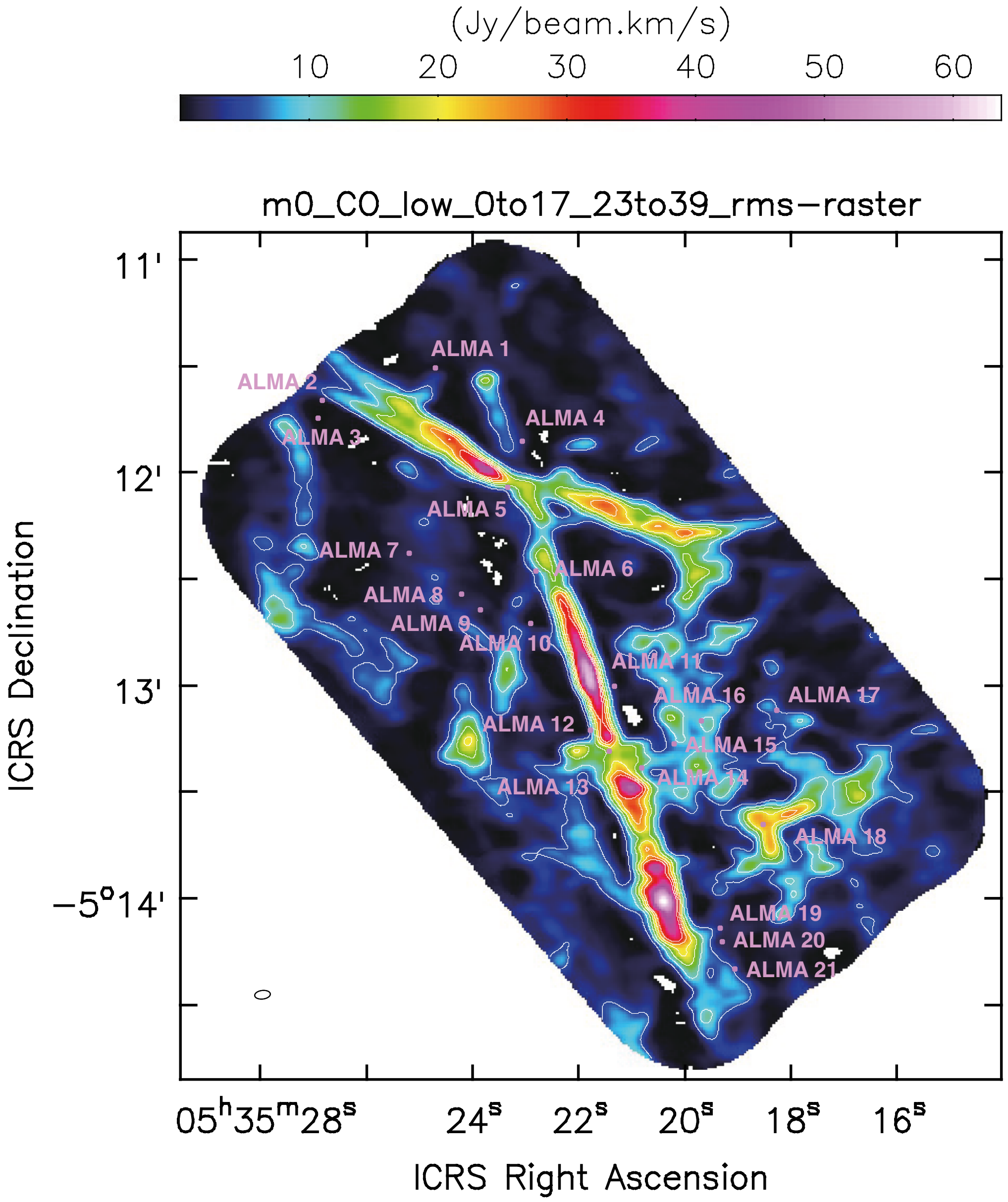

Figure 3.8: CO low velocity moment 0 map combined with ALMA 12m and ACA. The contour level starts at 5σ, [-5, 5, 10, 15, 20, 25, 30] (1σ for the continuum image is 14.7 mJy beam^{-1}.) The beam size is indicated by a circle in each panel.

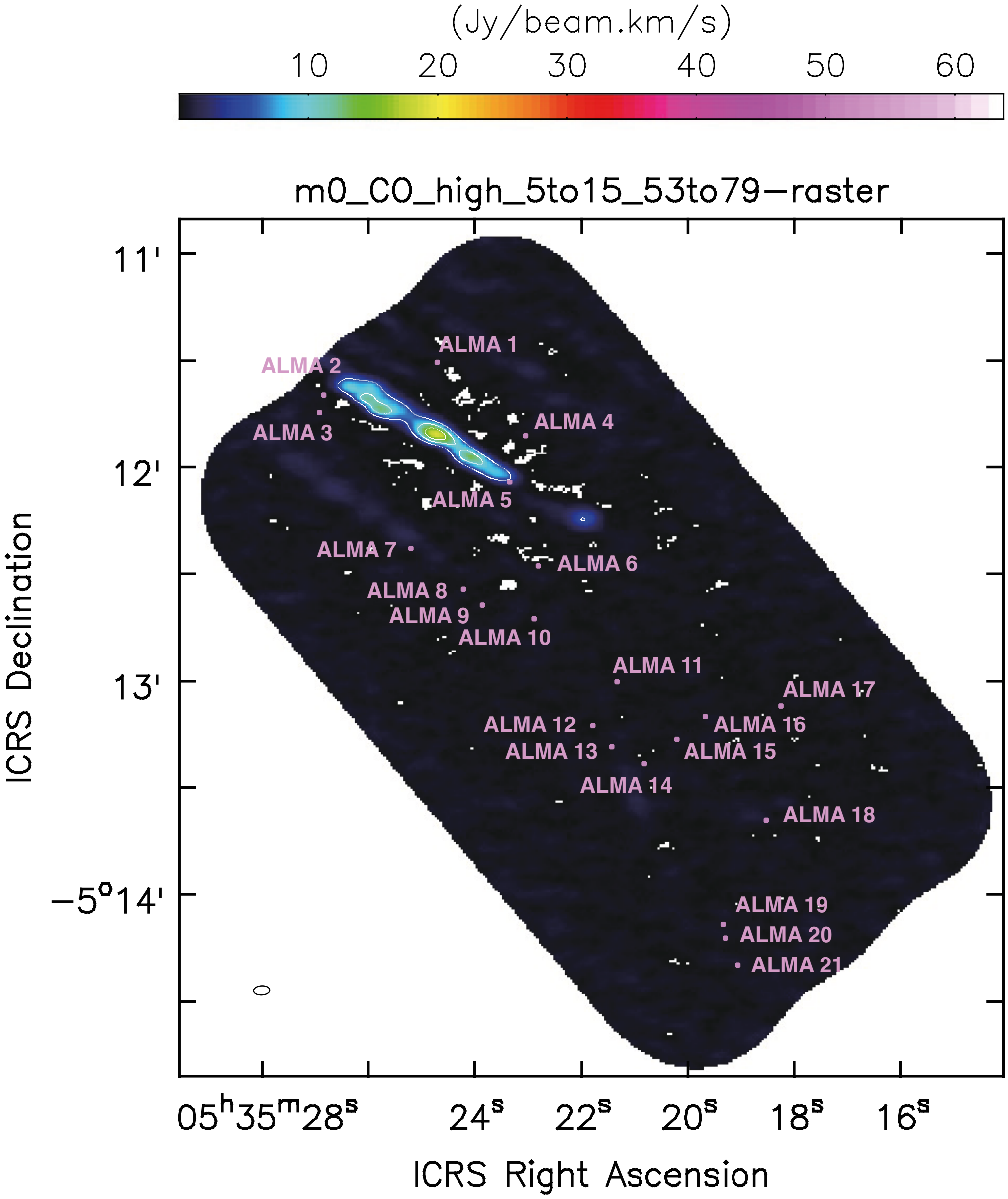

Figure 3.9: CO high velocity moment 0 map combined with ALMA 12m and ACA. The contour level starts at 5σ, [-5, 5, 10] (1σ for the continuum image is 14.7 mJy beam^{-1}.) The beam size is indicated by a circle in each panel.

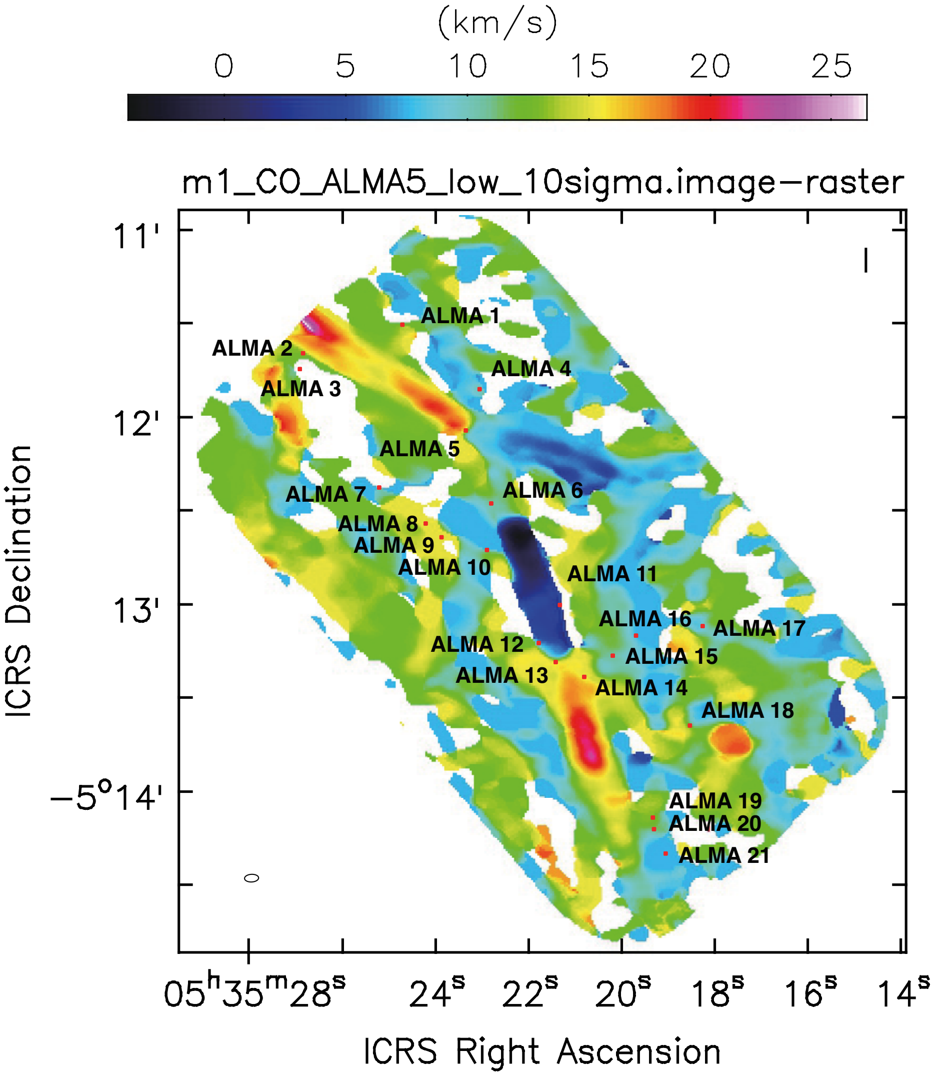

Figure 3.10: CO low velocity moment 1 map of OMC-2/FIR 6 combined with ALMA 12m and ACA. The panel shows the low velocity components with the velocity range of $v_{\rm LSR}$ -5 to 30 km s^{-1}. The beam size is indicated by a circle in each panel.

FIR 6 – ALMA 5 and FIR 6 – ALMA 13 have the strong CO outflow emission. Figure 3.11, Figure 3.12 and Figure 3.13 show the velocity channel map of CO emission in the entire OMC 2/FIR 6 region. Figure 3.11 shows an image of the low velocity component from -15 km s^{-1} to 37.5 km s^{-1}, and Figure 3.12 is a high velocity blueshifted component from -87.5 km s^{-1} to -62.5 km s^{-1}. Figure 3.13 is an image of the high velocity redshifted component from 40 km s^{-1} to 55 km s^{-1}, and Figure 3.13 is an image of the high velocity redshifted component from 57.5 km s^{-1} to 95 km s^{-1}.

FIR 6 – ALMA 5

The CO J = 2–1 channel maps shown in Figure 3.11, Figure 3.12 and Figure 3.13 indicate that the molecular outflow associated with FIR 6 – ALMA 5 is elongated along the NE–SW direction. In the low velocity components of $v_{\rm blue}$ = -10 $\sim$ 7.5 km s^{-1} and $v_{\rm red}$ = 12.5 $\sim$ 37.5 km s^{-1}, CO emission delineates a V-shaped structure and the opening angle is measured to be $\sim$ 5 deg. The size of this structure extends up to $\sim$ 60 arcsec, which corresponds to $\sim$ 0.12 pc (P.A.= 60 deg). The outflow direction is an approximately NE–SW (-115 deg) with a velocity of $\sim$ 9 km s^{-1} and a size of $\sim$ 0.2 pc, which are consistent with those estimated in previous studies (Takahashi et al. 2008; Shimajiri et al. 2009).

In the range of $v_{\rm blue}$ = -87.5 $\sim$ -62.5 km s^{-1} and $v_{\rm red}$ = 40 $\sim$ 95 km s^{-1}, which corresponds to the velocity of the EHV flow (i.e., the jet), a geometrically collimated structure is detected. The redshifted component is clearly resolved, and the length and width of the collimated structure are $\sim$ 0.12 pc and $\sim$ 0.02 pc, respectively. The collimated component is spatially resolved, because the synthesized beam size ($\leq$ 1,800 au) is smaller than the measured flow width. On the other hand, the blueshifted component does not have the elongated structure and the strong emission is detected as the compact component around ($05^h35^m21^s.914$, $-05^\circ12'14''.348$). The several bright compact knots are detected in the high velocity components. The knotty like structures are confirmed in other EHV flows observed in CO and SiO line emissions (Santiago-García et al. 2009, Kwon et al. 2015, Matsushita et al. 2019).

Figure 3.14 shows the CO J = 2–1 line profile of FIR 6 – ALMA 5 and the main (low velocity) component ranges are $|v_{\rm sys}|$ $\sim$ 11 km s^{-1}. In addition, I have detected EHV flows (i.e., the jet) in the range of 60 to 80 km s^{-1} with respect to the $v_{\rm sys}$ in CO J = 2–1 toward FIR 6 – ALMA 5. In the blueshifted line profile, the main components exist in the range of 0 to 25 km s^{-1} and the sub components, which correspond to the EHV flow, exist in the range of -20 to 0 km s^{-1}, while the emission is very weak. In FIR 6 – ALMA 5, the high velocity jet is detected for the first time.

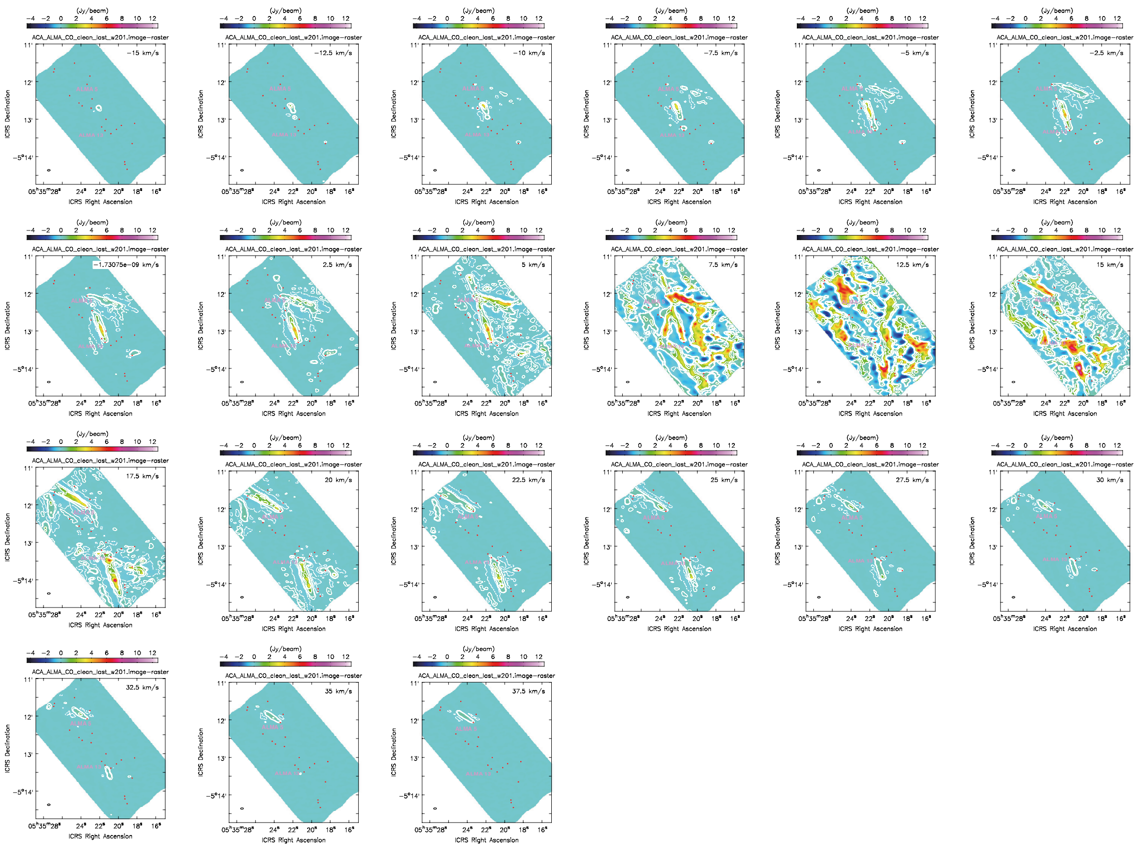

Figure 3.11: CO low velocity channel map combined with ALMA 12m and ACA. I described the velocity from -15 km s^{-1} to 37.5 km s^{-1}. The contour level starts at 5σ, [-5, 5, 10, 50, 100] (1σ for the continuum image is 14.7 mJy $beam^{-1}$.) The beam size is indicated by a circle in each panel.

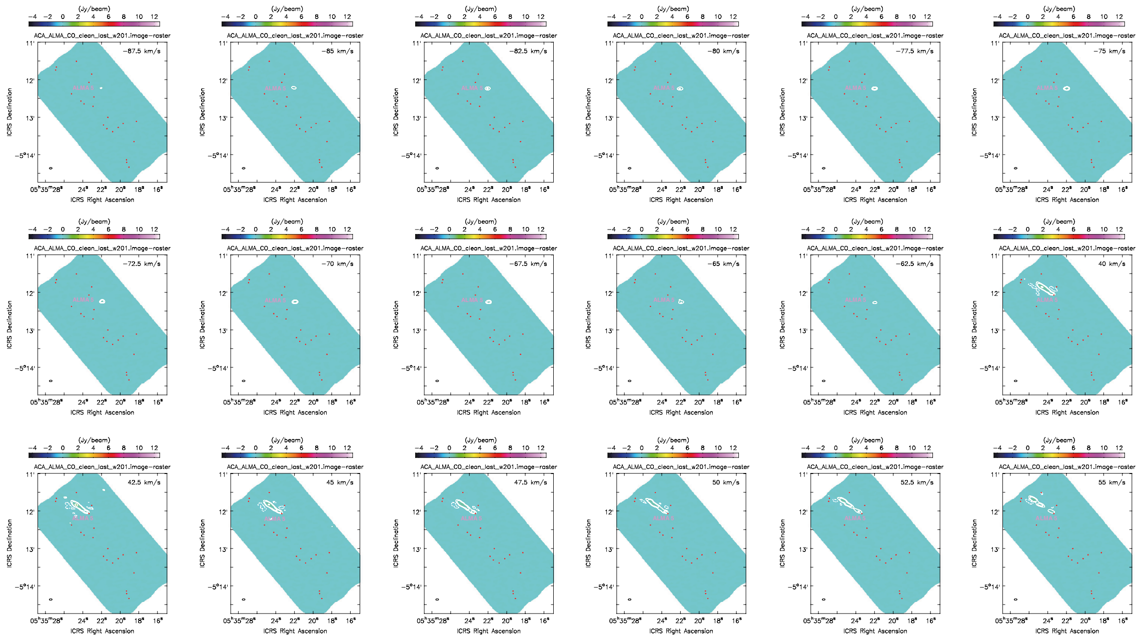

Figure 3.12: CO high velocity channel map combined with ALMA 12m and ACA. I described the velocity from -87.5 km s^{-1} to -62.5 km s^{-1} and 40 km s^{-1} to 55 km s^{-1}. The contour level starts at 5σ, [-5, 5, 10, 50, 100] (1σ for the continuum image is 14.7 mJy beam^{-1}.) The beam size is indicated by a circle in each panel.

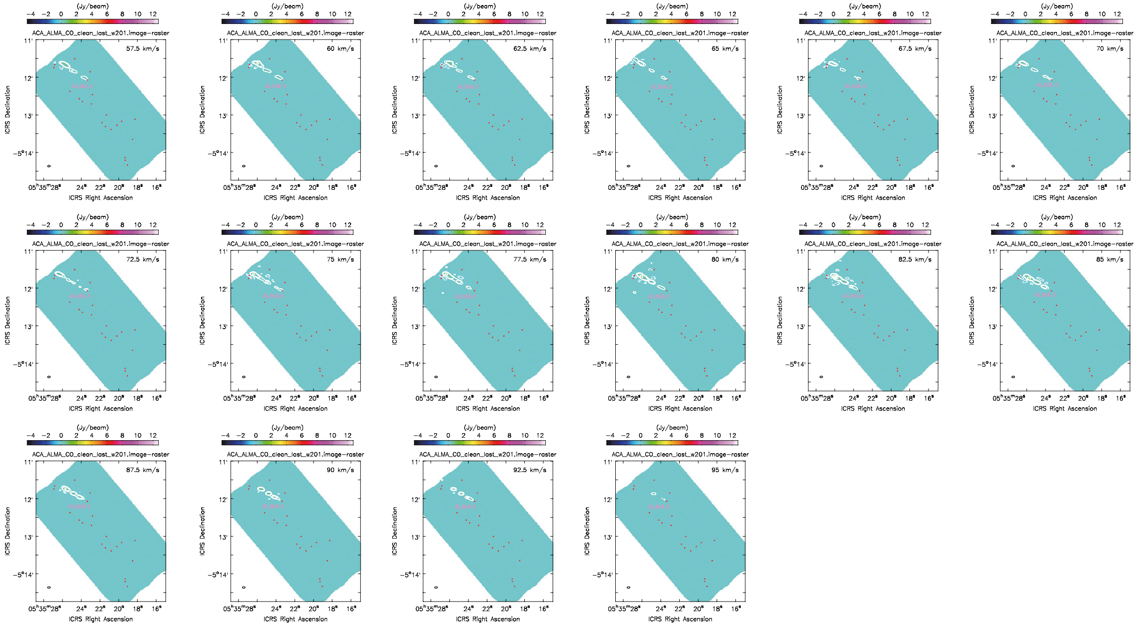

Figure 3.13: CO high velocity channel map combined with ALMA 12m and ACA. I described the velocity from 57.5 km s^{-1} to 95 km s^{-1}. The contour level starts at 5σ, [-5, 5, 10, 50, 100] (1σ for the continuum image is 14.7 mJy $beam^{-1}$.) The beam size is indicated by a circle in each panel.

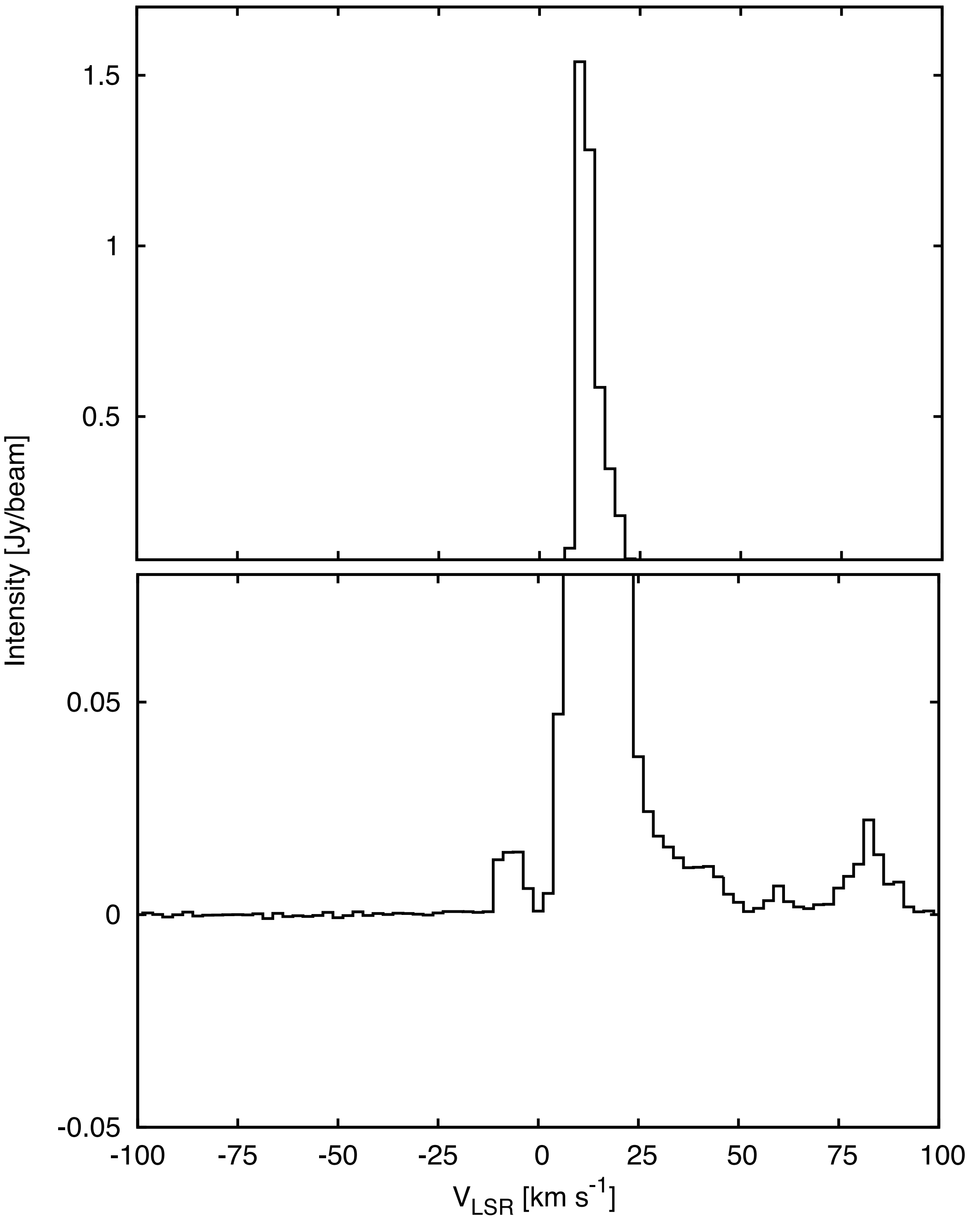

Figure 3.14: The line profile of the FIR 6 – ALMA 5 with CO emission.

FIR 6 – ALMA 13

The molecular outflow associated with FIR 6 – ALMA 13 is elongated along the N–S direction in Figure 3.11, Figure 3.12 and Figure 3.13. CO emission shows the low velocity components of $v_{\rm blue}$ = -15 $\sim$ 7.5 km s^{-1} and $v_{\rm red}$ = 12.5 $\sim$ 35 km s^{-1}. The low velocity component of FIR 6 – ALMA 13 does not delineate a V-shaped structure, but has a collimated structure like jet component. This structure extends up to $\sim$ 110 arcsec (blueshifted component) and $\sim$ 75 arcsec (redshifted component), which corresponds to $\sim$ 0.22 pc and $\sim$ 0.15 pc (P.A.= 20 deg), respectively. In previous studies (Takahashi et al. 2008; Shimajiri et al. 2009), the outflow is elongated in roughly N–S direction (30 deg) with the velocity of $\sim$ 10 km s^{-1} and size of $\sim$ 0.17 pc. They are consistent with my results.

FIR 6 – ALMA 18

Figure 3.15 top panel shows the moment 0 map of FIR 6 – ALMA 18 and others show the channel map. Figure 3.16 and Figure 3.17 show the channel map. The molecular outflow associated with FIR 6 – ALMA 18 is elongated along the NE–SW direction in Figure 3.15, Figure 3.16 and Figure 3.17. The CO emission shows the low velocity components of $v_{\rm blue}$ = -9 $\sim$ 7 km s^{-1} and $v_{\rm red}$ = 16 $\sim$ 30 km s^{-1}. In particular, CO emission delineated a V-shaped structure in the velocity range of $v_{\rm blue}$ = 1 $\sim$ 6 km s^{-1}. The size of this structure extends up to $\sim$ 22 arcsec (blueshifted component) and $\sim$ 8 arcsec (redshifted component), which corresponds to $\sim$ 8,800 au and $\sim$ 3,200 au (P.A.= 130 deg), respectively. The size of blueshifted component is 2.7 times larger than the redshifted component. In addition to the counter part of the redshifted components, there are other components in the velocity of $v_{\rm blue}$ = 16 $\sim$ 20 km s^{-1}. This outflow in FIR 6 – ALMA 18 has not been detected so far, and this is the first detection.

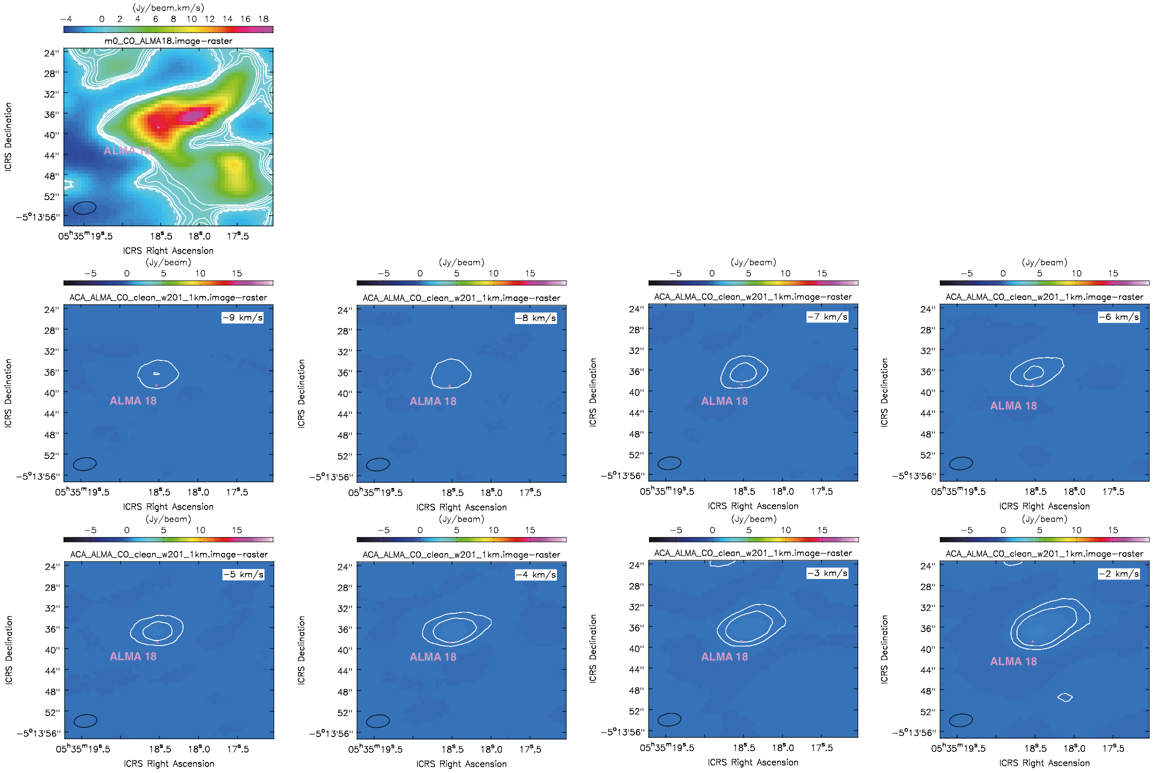

Figure 3.15: The top panel shows the moment 0 map around FIR 6 – ALMA 18 source, and others show these channel maps with the velocity range of v_{LSR} -9 to -2 km s^{-1}. The contour level starts at 5σ, [-5, 5, 10, 15, 20] (1σ for the continuum image is 14.7 mJy beam^{-1}.) The beam size is indicated by a circle in each panel.

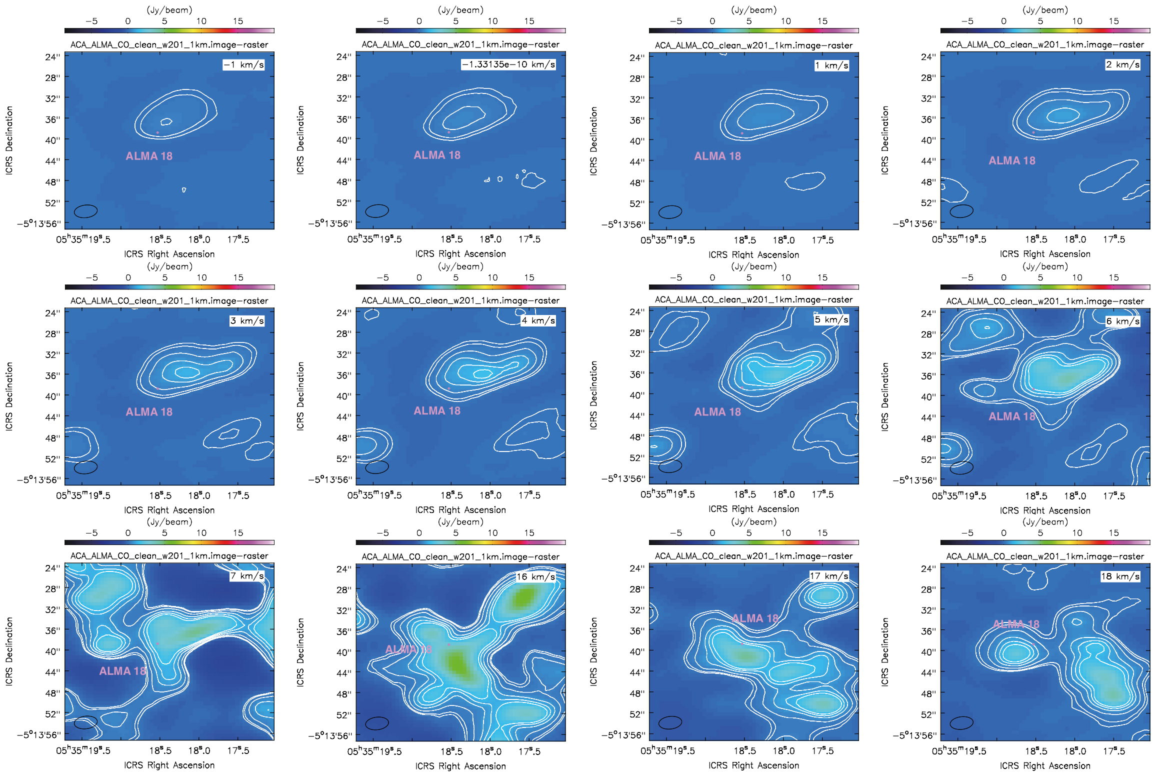

Figure 3.16: These panels show these channel maps around FIR 6 – ALMA 18 source with the velocity range of v_{LSR} -1 to 18 km s^{-1}. The contour level starts at 5σ, [-5, 5, 10, 15, 20] (1σ for the continuum image is 14.7 mJy beam^{-1}.) The beam size is indicated by a circle in each panel.

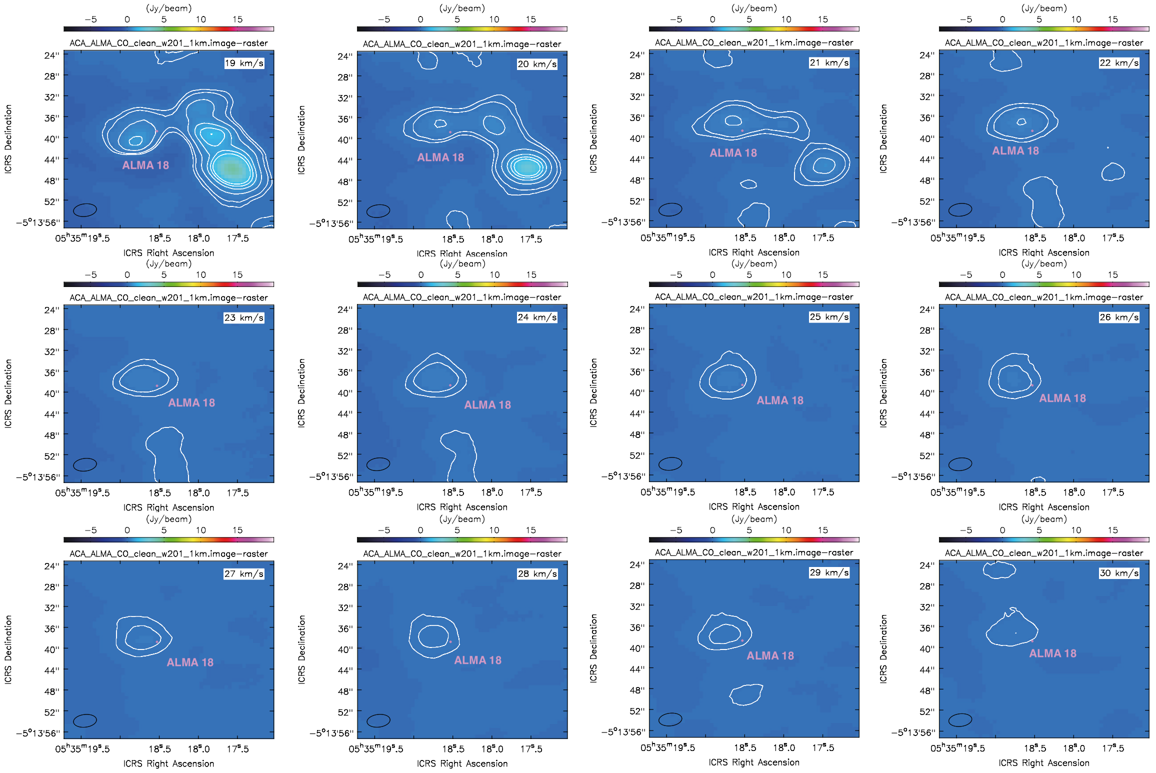

Figure 3.17: These panels show these channel maps around FIR 6 – ALMA 18 source with the velocity range of $v_{\rm LSR}$ 19 to 30 km s^{-1}.The contour level starts at 5σ, [-5, 5, 10, 15, 20] (1σ for the continuum image is 14.7 mJy beam^{-1}.) The beam size is indicated by a circle in each panel.

Next, I describe the details for some sources. It is difficult to determine whether outflow is driven in FIR 6 — ALMA 1, FIR 6 — ALMA 12, FIR 6 — ALMA 14, FIR 6 -– ALMA 15, FIR 6 — ALMA 16, FIR 6 — ALMA 17.

FIR 6 – ALMA 1

Figure 3.18 left panel shows the moment 0 map of FIR 6 – ALMA 1 and the eight right panels show the channel map. The CO emission shows the low velocity components of $v_{\rm blue} = 5 \sim 8$ km s^{-1} in the north region of FIR 6 – ALMA 1 and $v_{\rm red} = 14 \sim 17$ km s^{-1} in the south region of FIR 6 – ALMA 1. In particular, in the emission of the $v_{\rm LSR} = 6$ and 7 km s^{-1} of blueshifted component on the north side, it seems to be associated with FIR 6 – ALMA 1. On the redshifted side, there is the emission in the Northwest–Southeast direction, and it seems to be associated with FIR 6 – ALMA 1. This component overlaps the outflow driven from FIR 6 – ALMA 5. In all view, the emission seen in FIR 6 – ALMA 1 is outflow, because the redshifted and blushifted structures are visible in the N–S direction. For the first time, I detected the outflow in FIR 6 – ALMA 1.

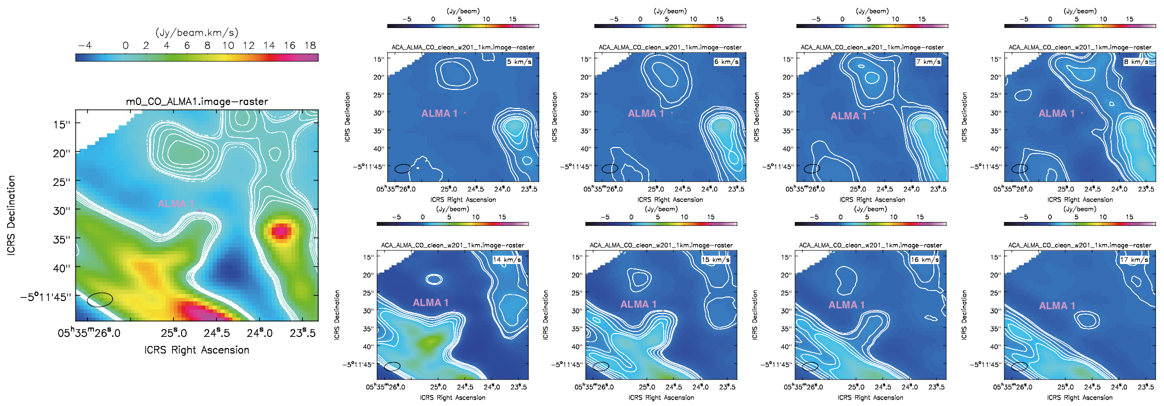

Figure 3.18: The top panel shows the moment 0 map around FIR 6 – ALMA 1 source, and others show these channel maps with the velocity range of $v_{\rm LSR}$ 5 to 8 km s^{-1} and $v_{\rm LSR}$ 14 to 17 km s^{-1}. The contour level starts at 5σ, [-5, 5, 10, 15, 20] (1σ for the continuum image is 14.7 mJy beam^{-1}.) The beam size is indicated by a circle in each panel.

In Figure. 3.19, the top of panel shows the moment 0 map around FIR 6 – ALMA 13 and the bottom of 10 panels show the channel map. With the velocity range of $v_{\rm blue} = 3 \sim 6$ km s^{-1} and $v_{\rm red} = 16 \sim 19$ km s^{-1}.

FIR 6 – ALMA 12

There was no emission on the blueshifted side. Even if the emission was detected around FIR 6 – ALMA 12, it may not be visible because it overlaps with FIR 6 – ALMA 13. On the other hand, in the velocity range of $v_{\rm red} = 16 \sim 19$ km s^{-1}, the redshifted emission was seen in the southwest side of FIR 6 – ALMA 12. In FIR 6 – ALMA 12, I could confirm the outflow where the counterpart was not clearly seen.

FIR 6 – ALMA 14

There is no clear emission in the blueshifted side in FIR 6 – ALMA 14, and the emission seen in the northeast direction of FIR 6 – ALMA 14 around the velocity of 6 km s^{-1} may be related. On the other hand, in the velocity range of $v_{\rm red} = 16 \sim 19$ km s^{-1}, the redshifted emission was seen on the southeast side of FIR 6 – ALMA 14. In FIR 6 – ALMA 14, I could confirm the outflow where the counterpart was not clearly seen.

FIR 6 – ALMA 15

The emisson is seen in the west direction of FIR 6 – ALMA 15 in the velocity range of $v_{\rm blue} = 4 \sim 6$ km s^{-1}. There is no emission on the redshifted side. In FIR 6 – ALMA 15, it is difficult to determine whether clear outflow is associated. However, the outflow from FIR 6 – ALMA 15 has been reported in Shimajiri et al. (2009). They showed that the outflow exists in the velocity range of 7.7 km s^{-1} to 12.6 km s^{-1}. On the other hand, in my observation, it was not detected because I performed imaging excluding these velocity range.

FIR 6 – ALMA 16

The emisson is seen in the west direction of FIR 6 – ALMA 15 in the velocity range of $v_{\rm blue} = 3 \sim 6$ km s^{-1}. There is no emission on the redshifted side. From FIR 6 – ALMA 16, it is difficult to determine whether clear outflow is associated. I named this outflow as marginal outflow.

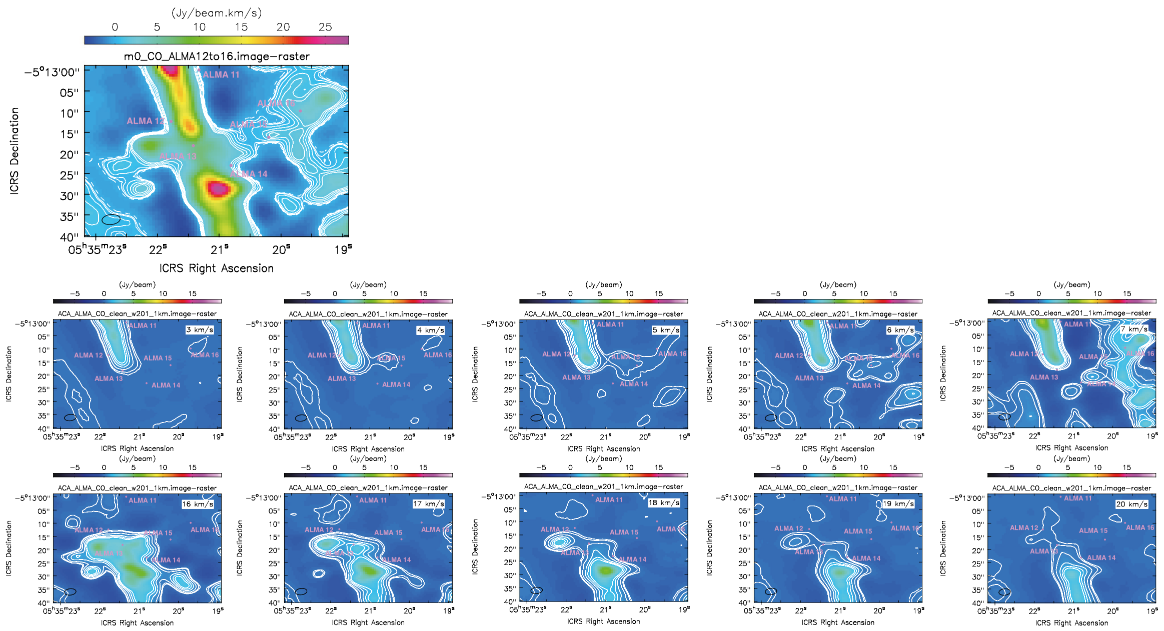

Figure 3.19: The top panel shows the moment 0 map around FIR 6 – ALMA 13 source, and others show these channel maps with the velocity range of $v_{\rm LSR}$ 3 to 7 km s^{-1} and $v_{\rm LSR}$ 16 to 20 km s^{-1}. The contour level starts at 5σ, [-5, 5, 10, 15, 20] (1σ for the continuum image is 14.7 mJy beam^{-1}.) The beam size is indicated by a circle in each panel.

FIR 6 – ALMA 17

Figure 3.20 top left panel shows the moment 0 map around FIR 6 – ALMA 17 and the other panels show the channel map. These figures show the velocity range of $v_{\rm blue} = 5 \sim 8$ km s^{-1} and $v_{\rm red} = 15 \sim 19$ km s^{-1}. The emisson is seen in the north direction of FIR 6 – ALMA 17 in the velocity range of $v_{\rm blue} = 5 \sim 8$ km s^{-1}. On the other hand, the redshifted component is complex in the velocity of 15–16 km s^{-1} and the emission is detected in the southwest direction of FIR 6 – ALMA 17 in the velocity range of $v_{\rm blue} = 17 \sim 19$ km s^{-1}. The direction in which the emission is confirmed in the moment map is slightly different from the direction in which the emission is confirmed by the channel map. This is the effect of the emission visible to the southeast of FIR 6 – ALMA 17 at 8 km s^{-1}. Roughly, the outflow seems to be driven with a size of 5 arcsec (blueshift) and 15 arcsec (redshift), which corresponds to $\sim$ 2,000 au and $\sim$ 6,000 au in the north-south direction. This outflow in FIR 6 – ALMA 17 is the first detection.

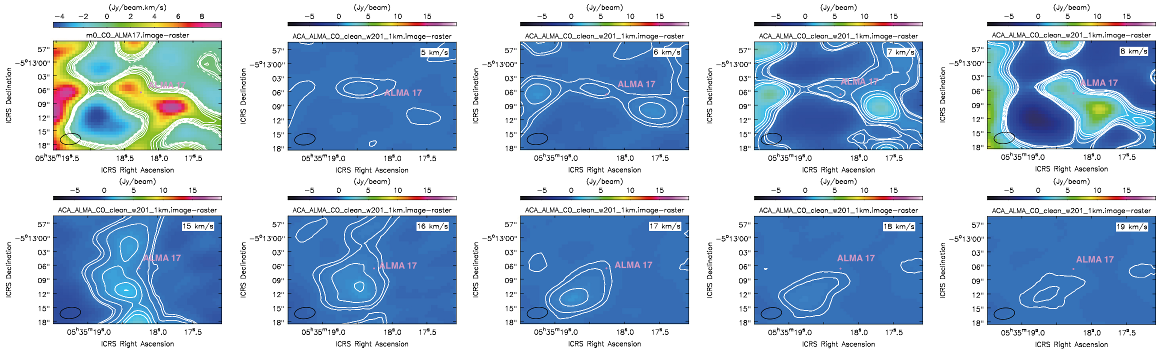

Figure 3.20: The top left panel shows the moment 0 map around FIR 6 – ALMA 17 source, and others show these channel maps with the velocity range of $v_{\rm LSR}$ 5 to 8 km s^{-1} and $v_{\rm LSR}$ 15 to 19 km s^{-1}. The contour level starts at 5σ, [-5, 5, 10, 15, 20] (1σ for the continuum image is 14.7 mJy beam^{-1}.) The beam size is indicated by a circle in each panel.

3.2.2 SiO outflow

In the moment map presented in Figure 3.21, I only detected a collimated SiO J = 5–4 structure associated with FIR 6 – ALMA 13. I could confirm the SiO collimated structure in the range of $|v_{\rm LSR} - v_{\rm sys}| \sim 10$ to 25 km s^{-1}. Figure 3.22 and Figure 3.23 show the SiO J = 5–4 channel map with the velocity range of -15 km s^{-1} to 22.5 km s^{-1}. A strong blueshifted emission is detected in the range of -15 km s^{-1} to 12.5 km s^{-1}. The redshifted emission is only detected about 60 arcsec ($\sim$ 0.12 pc) away from FIR 6 – ALMA 13 in the south region. The structure extends up to $\sim$ 75 arcsec (blueshifted components) and $\sim$ 60 arcsec (redshifted components), which corresponds to $\sim$ 0.15 pc and $\sim$ 0.12 pc (P.A $\sim$ 60 deg), respectively. The SiO J = 2–1 emission is also detected. The size of this structure is about 70 arcsec, $\sim$ 0.14 pc, (Shimajiri et al. 2009). The SiO J = 2–1 flow has a velocity range of -11.7 km s^{-1} to 15.3 km s^{-1}. This studies are consistent with my results. The peak flux of the blueshifted components is five times stronger than that of the redshifted components. I can see a strong CO J = 2–1 emission in FIR 6 – ALMA 5 and FIR 6 – ALMA 13. In addition, FIR 6 – ALMA 5 has the EHV flow (jet), while it does not associate with the SiO J = 5–4 emission.

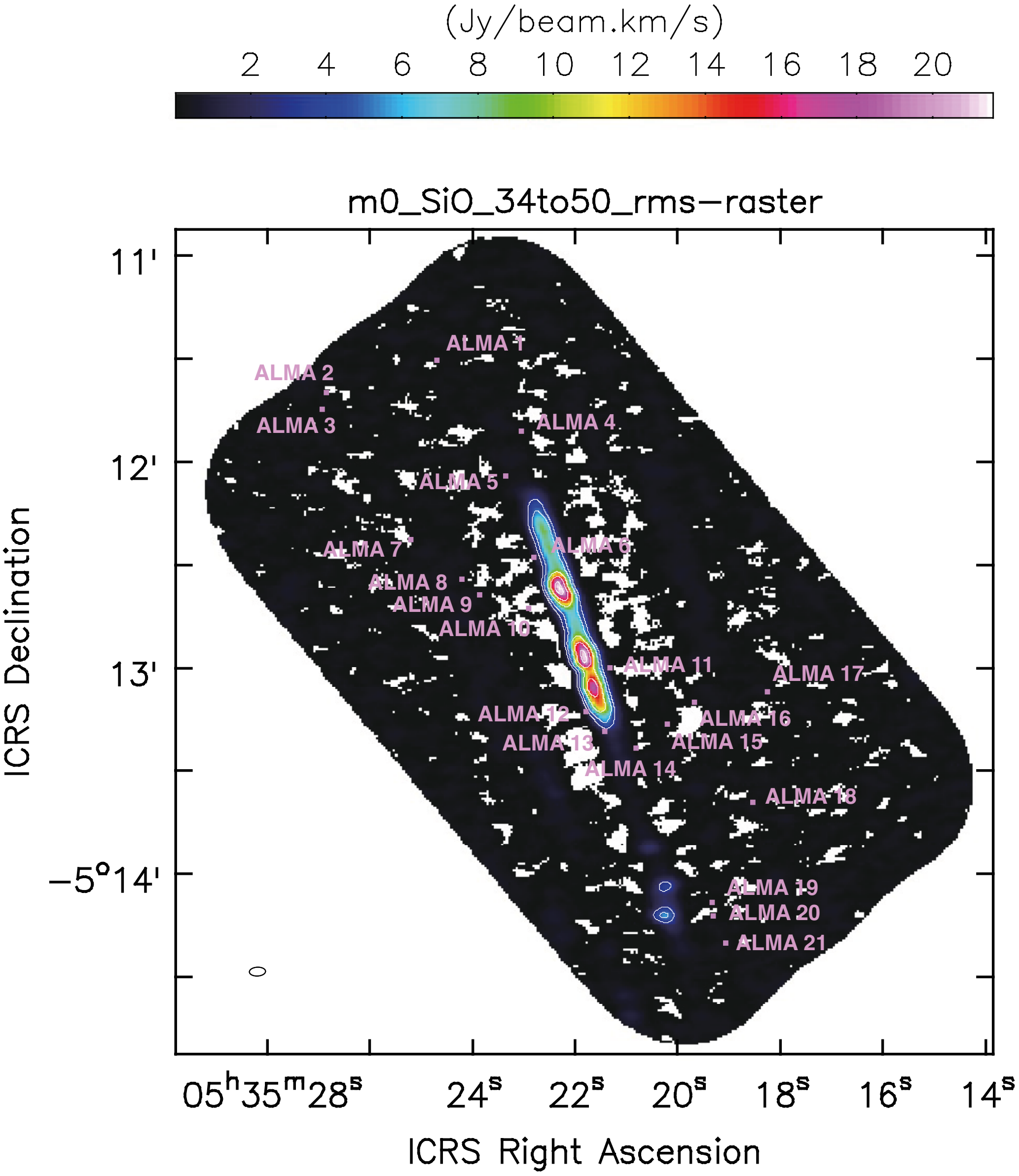

Figure 3.21: This figure shows SiO moment 0 map combined with ALMA 12m and ACA. The contour level starts at 3σ, [-3, 3, 5, 10, 15, 20] (1σ for the continuum image is 13.1 mJy beam^{-1}.) The beam size is indicated by a circle in each panel.

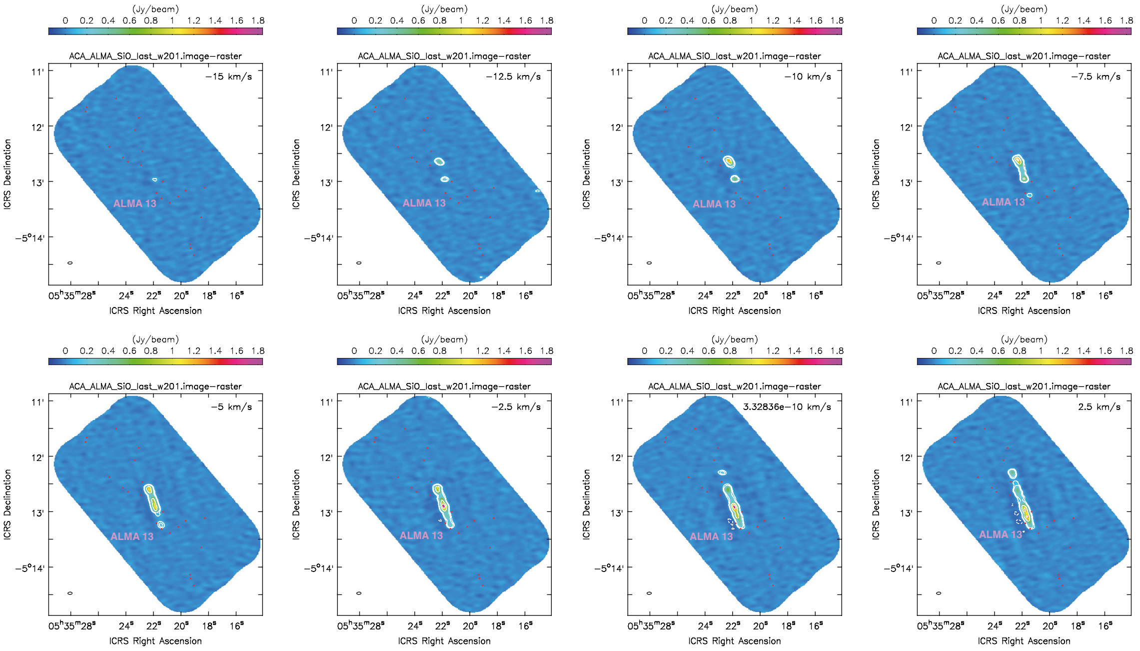

Figure 3.22: SiO: Combined with ALMA 12m and ACA. The contour level starts at 5σ, [-5, 5, 10, 50, 100] (1σ for the continuum image is 13.1 mJy beam^{-1}.) The beam size is indicated by a circle in each panel.

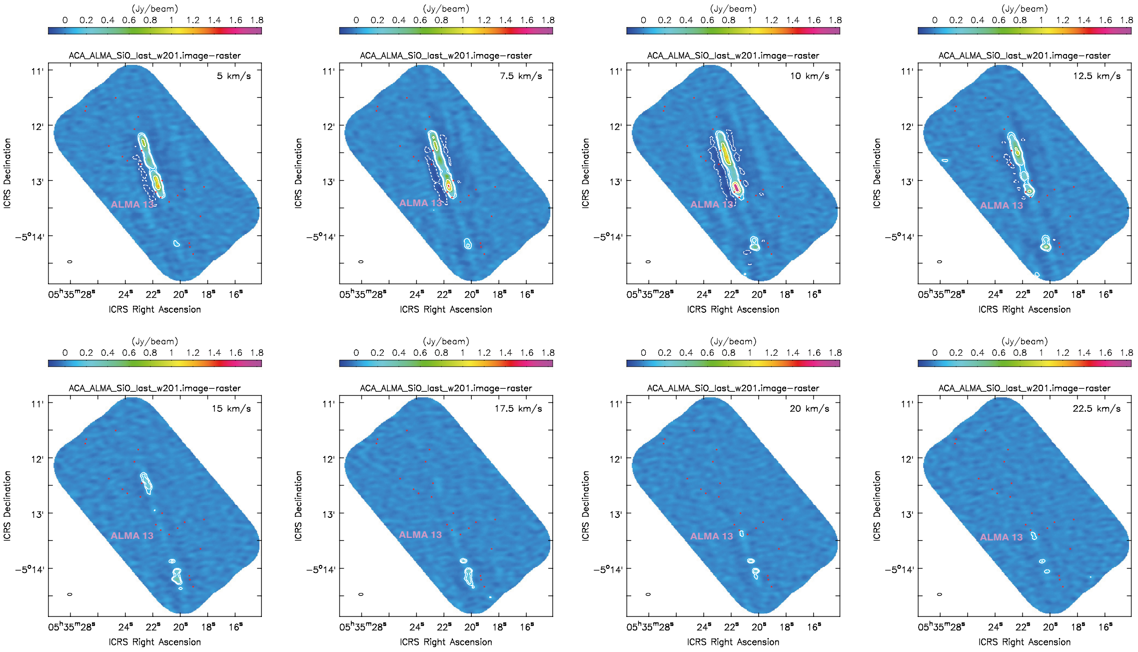

Figure 3.23: SiO: Combined with ALMA 12m and ACA. The contour level starts at 5σ, [-5, 5, 10, 50, 100] (1σ for the continuum image is 13.1 mJy beam^{-1}.) The beam size is indicated by a circle in each panel.

Chapter 4

DISCUSSIONS

4.1 Star formation in OMC-2/FIR 6

I could discover 10 sources for the first time with high angular resolution observation. They were not detected by the infrared observation (Chini et al. 1997, Lis et al. 1998, Nielbock et al. 2003, Furlan et al. 2016) and the latest ALMA observation (van Terwisga et al. 2019). In addition, since no sources consistent with observations at other wavelengths were detected, it is predicted that the sources are in either fairly young stage, prestellar cores or starless cores. The infrared detection rate in this entire region is 10/21, so it is approximately ~ 48 %. Nearly half of the sources found in OMC-2/FIR 6 are likely to be either fairly young stars without an infrared source, or starless cores.

CO and SiO results show that there are many sources showing outflow in this region. There are 9 sources that are considered to be accompanied by CO outflow, three of which are judged to have clear outflow, and six sources have marginal outflow. The outflow detection rate in OMC-2/FIR 6 was 23.8 to 42.7 % (5/21 to 9/21). Among the sources that are considered to be associated with outflow, three sources are Class II (flat), two sources are Class 0, two sources are known as the starless core in previous studies and two sources were discovered for the first time. It is considered that the starless core and the first detection sources, which were associated with outflow, were a fairly young stage and immediately after the formation of the protostar. FIR 6 – ALMA 5 and FIR 6 – ALMA 13 have the most intense outflow in this region, and only these two sources are Class 0 sources. Outflows from other Class II sources and the starless core are small and weak. This indicates that outflow is driven most actively in Class 0 sources. This result is consistent with the results suggested by theoretically simulations (Machida 2014).

I classified the sources discovered in my ALMA observation into starless core, Class 0, Class I, and Class II sources. FIR 6 – ALMA 2, FIR 6 – ALMA 3, FIR 6 – ALMA 4, FIR 6 – ALMA 7, FIR 6 – ALMA 8, FIR 6 – ALMA 9, FIR 6 – ALMA 11, FIR 6 – ALMA 19, FIR 6 – ALMA 20 and FIR 6 – ALMA 21 of total 10 sources are starless core, because they show neither infrared source nor outflow. FIR 6 – ALMA 6 and FIR 6 – ALMA 10 of total two sources are a little evolved starless core, because they have an infrared source without outflow. FIR 6 – ALMA 12, FIR 6 – ALMA 14, FIR 6 – ALMA 16 and FIR 6 – ALMA 17 of total four sources are in between starless and Class 0 (which is pretty younger than Class 0) stages, because they have outflow in my ALMA observation. Two sources are in the Class 0 stage (FIR 6 – ALMA 5 and FIR 6 – ALMA 13), and the Class II sources are FIR 6 – ALMA 1, FIR 6 – ALMA 15 and FIR 6 – ALMA 18 of total three. In particular, the core is concentrated in the bent part (hub) of the filament where FIR 6 – ALMA 12 to FIR 6 – ALMA 16 exist. The places where this core is concentrated have various age sources from starless to Class II stage. It is known that a lot of gas flows into the hub of the filament, and star formation and clamp formation are active (Myers 2009, Kirk et al. 2013, Schneider et al. 2010, Peretto et al. 2013). I observed such the feeding process in this hub. It is considered that the filament provide the gas to the central hub where Class II sources exist (FIR 6 – ALMA 15), and the stars formed there. Moreover the filament provide the gas to the next bigger hub where Class 0 sources (FIR 6 – ALMA 13) exist and they are now growing. The starless core may have been born around the big hub. The area of FIR 6 – ALMA 10 may also be the hub, in which the gas is supplied from filament and star formation would be progressing.

4.2 CO and SiO emissions in FIR 6 – ALMA 13

Since both CO and SiO were detected in only FIR 6 – ALMA 13, I focus on FIR 6 – ALMA 13. In Figure 4.1 to Figure 4.10, the channel map of CO $J = 2$–1 and SiO $J = 5$–4 is overlaid with the contour. The contour level started at 5 σ and the channel map was created with $\delta v = 2.5$ km s^{-1}. The CO $J = 2$–1 emission is shown by blue lines, and the SiO $J = 5$–4 emission is shown by red lines. In FIR 6 – ALMA 13, a structure similar to the outflow seen in CO is also confirmed in SiO (Figure 4.5, Figure 4.6 and Figure 4.7). The peak positions of CO and SiO have a trend. In the vicinity of continuum peak position, the SiO emission exists near the continuum peak position, which is closer than the CO emission. In particular, the channel map of -7.5 km s^{-1}, -5 km s^{-1}, 22.5 km s^{-1}, 25 km s^{-1} shows a tendency; the SiO emission is distributed near the continuum peak position. In the ALMA interferometer observation, the positional error is determined by $\sim \theta_{\rm beam}/2({\rm S/N})$ with S/N $\sim$ 5 where the $\theta_{\rm beam}$ is the beam size. In this observation, the beam size is $\sim$ 4.5 arcsec, so the position accuracy is measured to be $\sim$ 0.45 arcsec. The peak positional shift between SiO and CO emissions is $\sim$ 8 arcsec at the maximum and $\sim$ 2 arcsec at the minimum. These positional shifts are real trend. It is consider that the SiO forms in high density jet (Shang et al. 2006) and can be quickly formed near the central protostar (Glassgold et al. 1989, 1991). In other words, since the SiO appears at a higher density and closer to the shock, it may have been detected in the region slightly closer to the continuum peak position than the CO. Such a tendency has been confirmed also in other sources, for example, the SiO emission is also slightly shifted inward of HH211 EHV flow (Dionatos et al. 2010) and MMS 5/OMC-3 EHV flow (Matsushita et al. 2019).

In OMC-2/FIR 6, FIR 6 – ALMA 5 and FIR 6 – ALMA 13 show a similar strong CO emission.

On the other hand, the SiO emission dose not detected in FIR 6 – ALMA 5. Although strong CO emission is detected, the shock is weak and may not have been heated to the extent that SiO appears. It is also considered that SiO is not simply not visible with the detection limit.

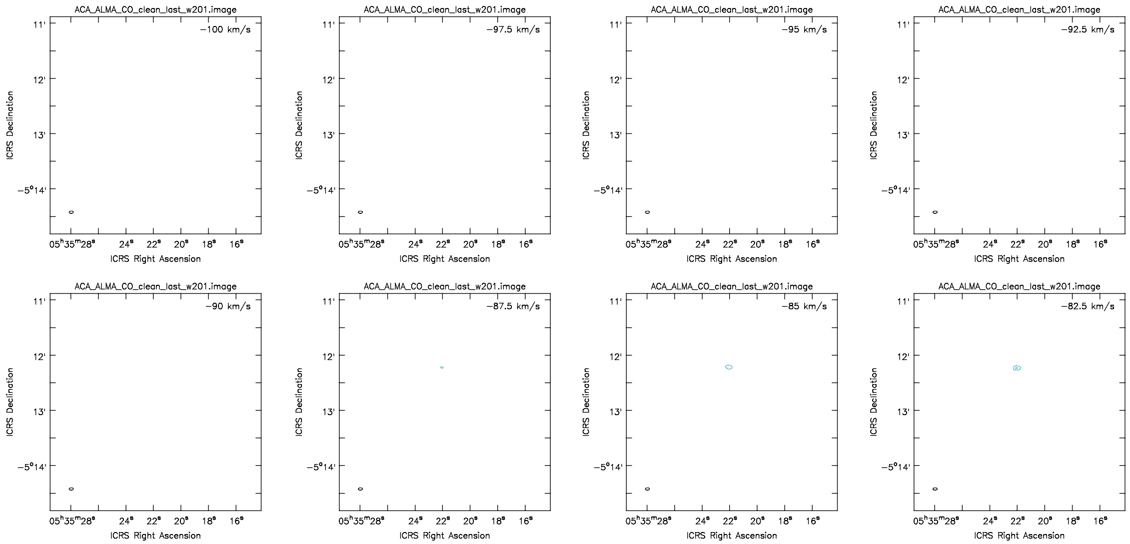

Figure 4.1: CO: Combined with ALMA 12m and ACA. The contour level starts at 5σ, [-5, 5, 10, 20, 40, 60, 80, 100, 150, 200] (1σ for the continuum image is 14.7 mJy beam^{-1}.) SiO: Combined with ALMA 12m and ACA. The contour level starts at 5σ, [-5, 5, 10, 20, 40, 60, 80, 100, 150, 200] (1σ for the continuum image is 13.1 mJy beam^{-1}.) The beam size is indicated by a circle in each panel.

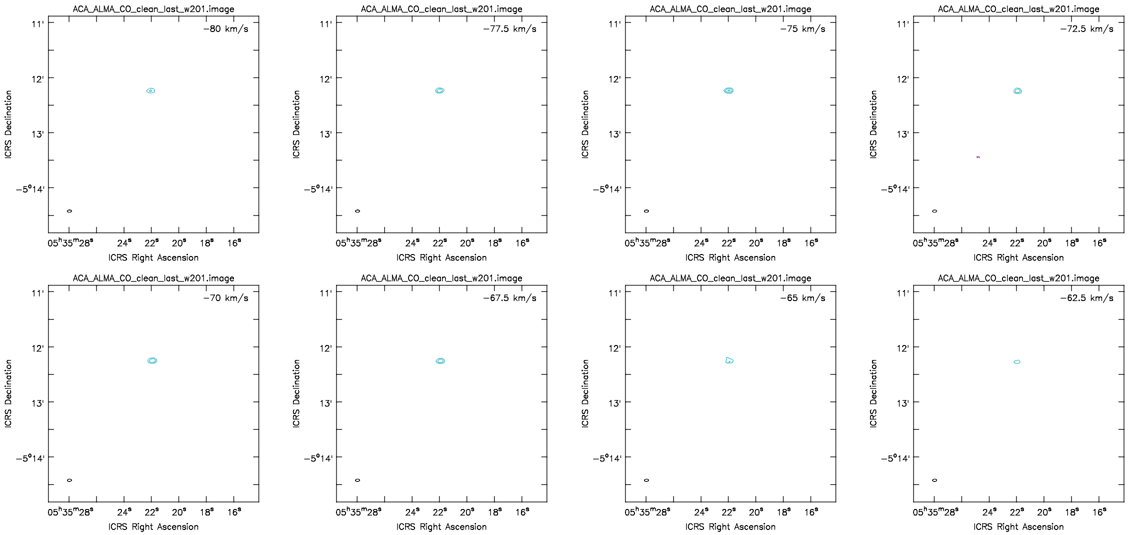

Figure 4.2: CO: Combined with ALMA 12m and ACA. The contour level starts at 5σ, [-5, 5, 10, 20, 40, 60, 80, 100, 150, 200] (1σ for the continuum image is 14.7 mJy beam^{-1}.) SiO: Combined with ALMA 12m and ACA. The contour level starts at 5σ, [-5, 5, 10, 20, 40, 60, 80, 100, 150, 200] (1σ for the continuum image is 13.1 mJy beam^{-1}.) The beam size is indicated by a circle in each panel.

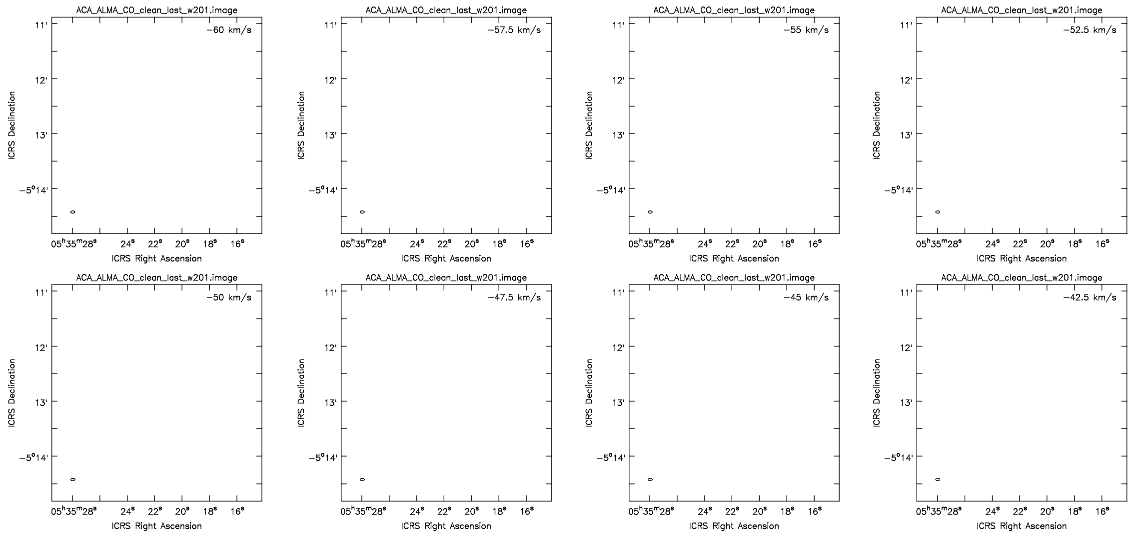

Figure 4.3: CO: Combined with ALMA 12m and ACA. The contour level starts at 5σ, [-5, 5, 10, 20, 40, 60, 80, 100, 150, 200] (1σ for the continuum image is 14.7 mJy beam^{-1}.) SiO: Combined with ALMA 12m and ACA. The contour level starts at 5σ, [-5, 5, 10, 20, 40, 60, 80, 100, 150, 200] (1σ for the continuum image is 13.1 mJy beam^{-1}.) The beam size is indicated by a circle in each panel.

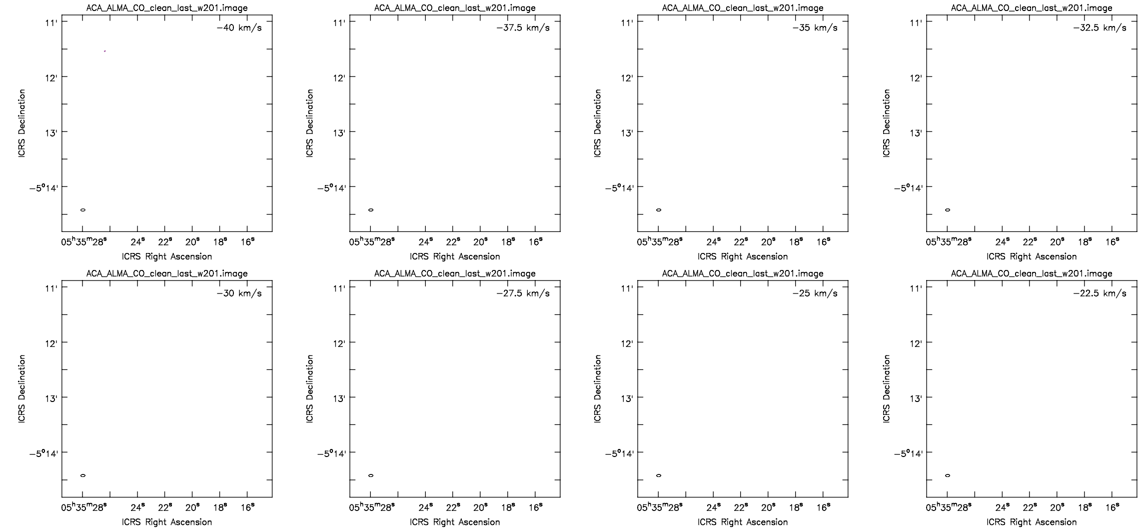

Figure 4.4: CO: Combined with ALMA 12m and ACA. The contour level starts at 5σ, [-5, 5, 10, 20, 40, 60, 80, 100, 150, 200] (1σ for the continuum image is 14.7 mJy beam^{-1}.) SiO: Combined with ALMA 12m and ACA. The contour level starts at 5σ, [-5, 5, 10, 20, 40, 60, 80, 100, 150, 200] (1σ for the continuum image is 13.1 mJy beam^{-1}.) The beam size is indicated by a circle in each panel.

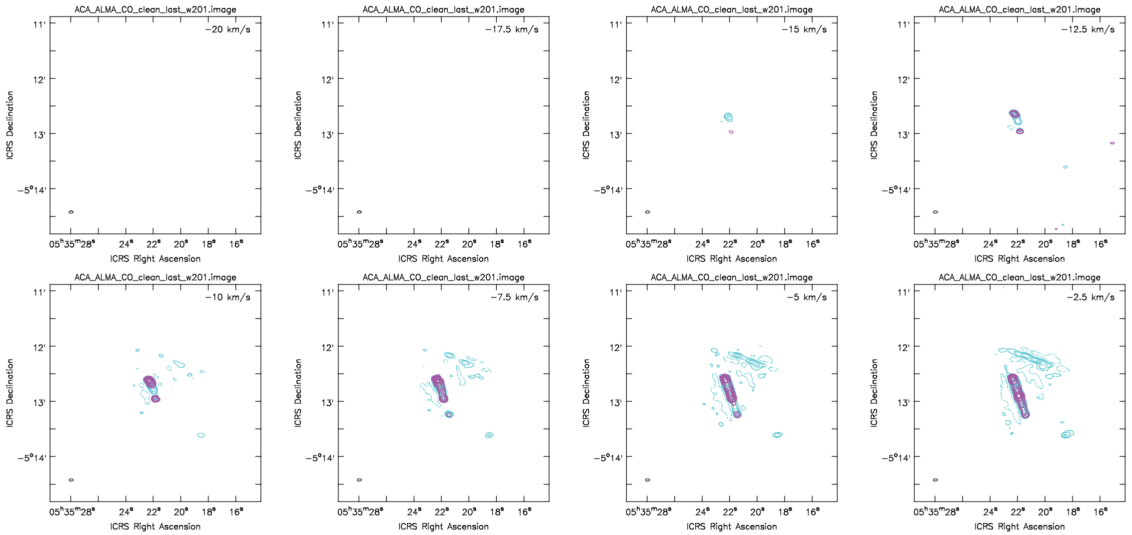

Figure 4.5: CO: Combined with ALMA 12m and ACA. The contour level starts at 5σ, [-5, 5, 10, 20, 40, 60, 80, 100, 150, 200] (1σ for the continuum image is 14.7 mJy beam^{-1}.) SiO: Combined with ALMA 12m and ACA. The contour level starts at 5σ, [-5, 5, 10, 20, 40, 60, 80, 100, 150, 200] (1σ for the continuum image is 13.1 mJy beam^{-1}.) The beam size is indicated by a circle in each panel.

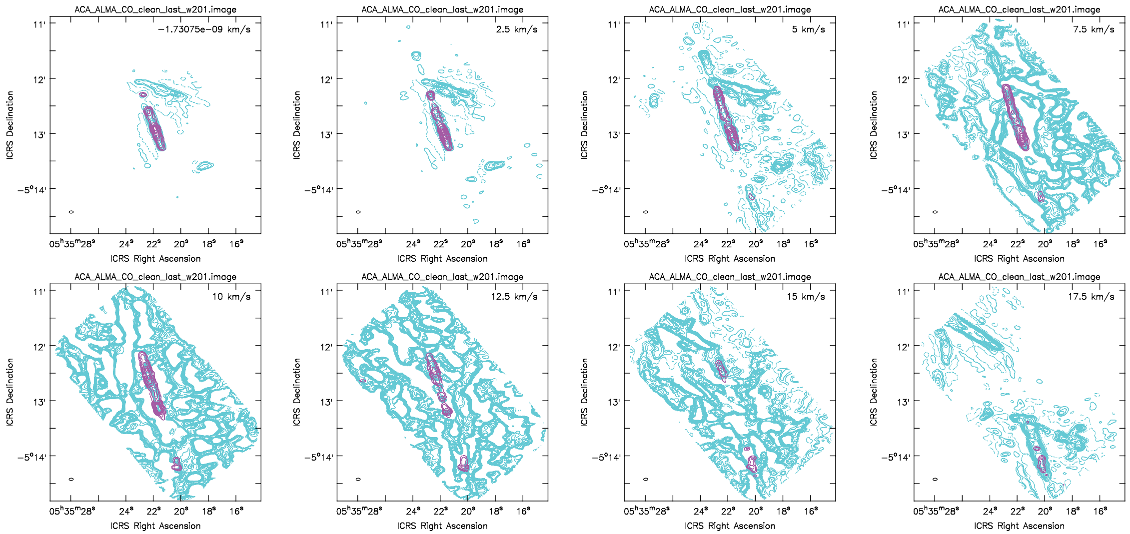

Figure 4.6: CO: Combined with ALMA 12m and ACA. The contour level starts at 5σ, [-5, 5, 10, 20, 40, 60, 80, 100, 150, 200] (1σ for the continuum image is 14.7 mJy beam^{-1}.) SiO: Combined with ALMA 12m and ACA. The contour level starts at 5σ, [-5, 5, 10, 20, 40, 60, 80, 100, 150, 200] (1σ for the continuum image is 13.1 mJy beam^{-1}.) The beam size is indicated by a circle in each panel.

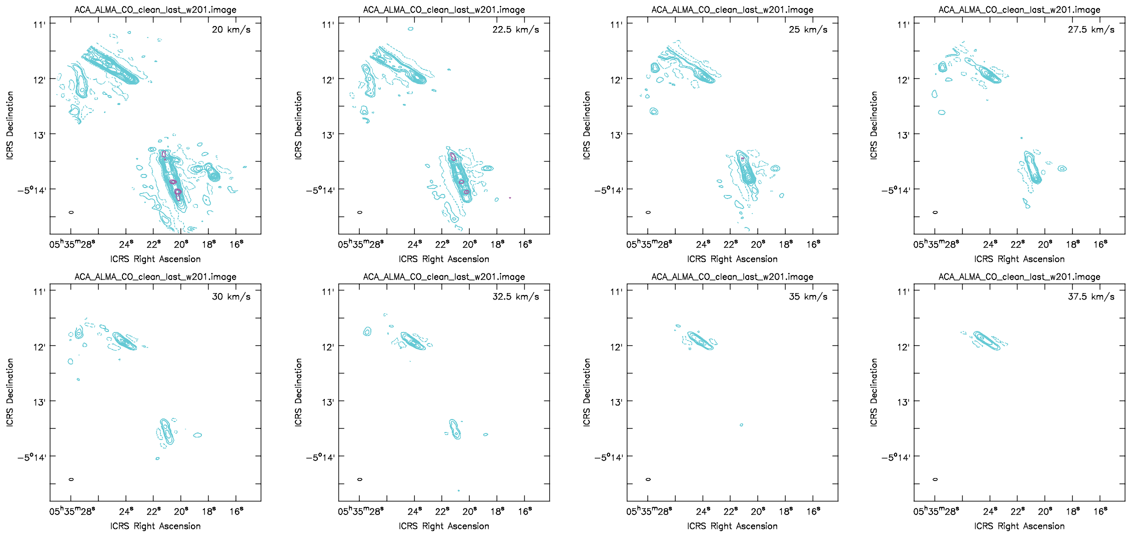

Figure 4.7: CO: Combined with ALMA 12m and ACA. The contour level starts at 5σ, [-5, 5, 10, 20, 40, 60, 80, 100, 150, 200] (1σ for the continuum image is 14.7 mJy beam^{-1}.) SiO: Combined with ALMA 12m and ACA. The contour level starts at 5σ, [-5, 5, 10, 20, 40, 60, 80, 100, 150, 200] (1σ for the continuum image is 13.1 mJy beam^{-1}.) The beam size is indicated by a circle in each panel.

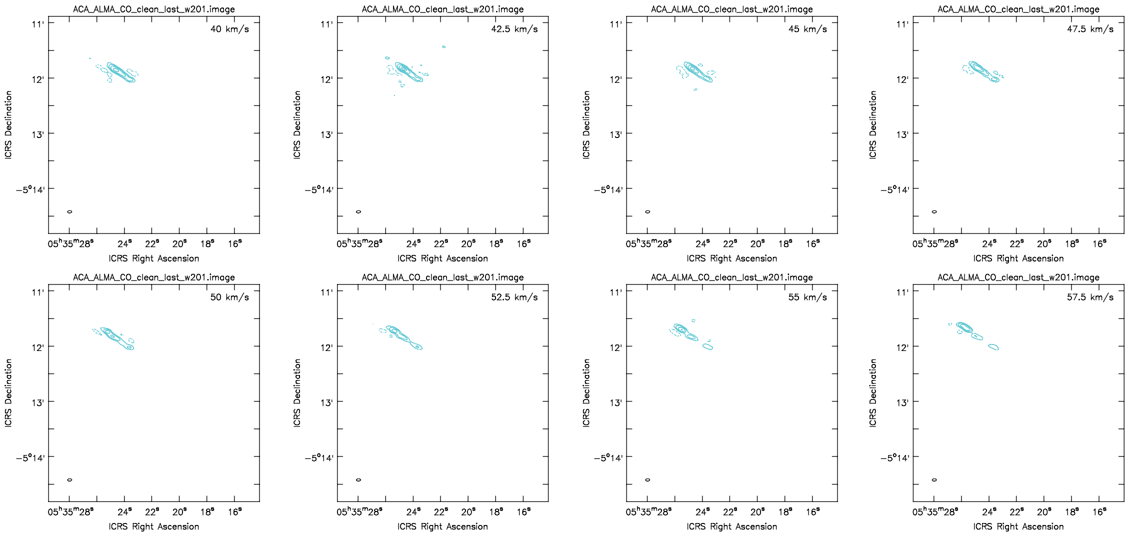

Figure 4.8: CO: Combined with ALMA 12m and ACA. The contour level starts at 5σ, [-5, 5, 10, 20, 40, 60, 80, 100, 150, 200] (1σ for the continuum image is 14.7 mJy beam^{-1}.) SiO: Combined with ALMA 12m and ACA. The contour level starts at 5σ, [-5, 5, 10, 20, 40, 60, 80, 100, 150, 200] (1σ for the continuum image is 13.1 mJy beam^{-1}.) The beam size is indicated by a circle in each panel.

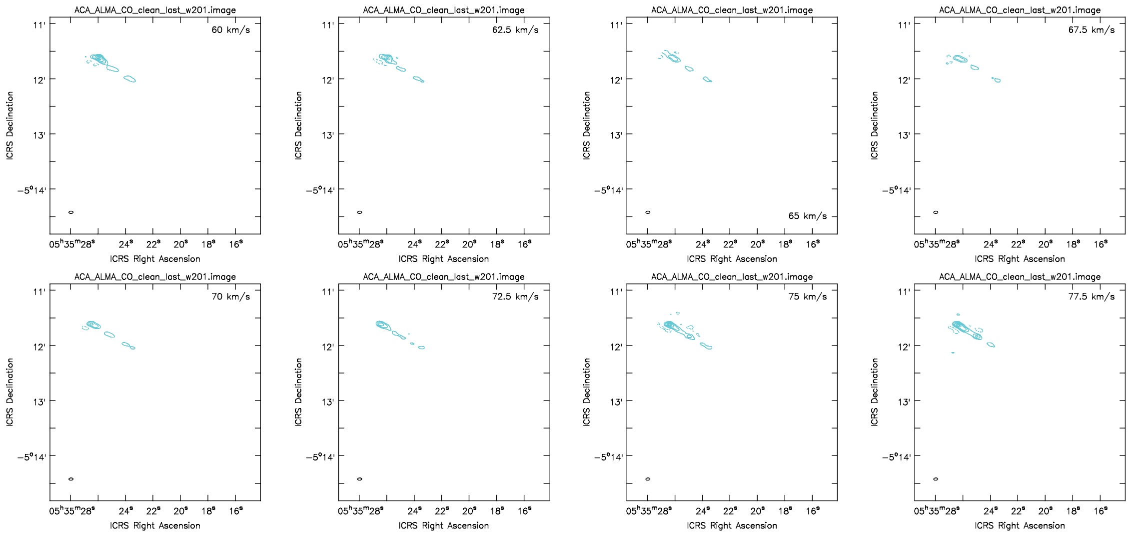

Figure 4.9: CO: Combined with ALMA 12m and ACA. The contour level starts at 5σ, [-5, 5, 10, 20, 40, 60, 80, 100, 150, 200] (1σ for the continuum image is 14.7 mJy beam^{-1}.) SiO: Combined with ALMA 12m and ACA. The contour level starts at 5σ, [-5, 5, 10, 20, 40, 60, 80, 100, 150, 200] (1σ for the continuum image is 13.1 mJy beam^{-1}.) The beam size is indicated by a circle in each panel.

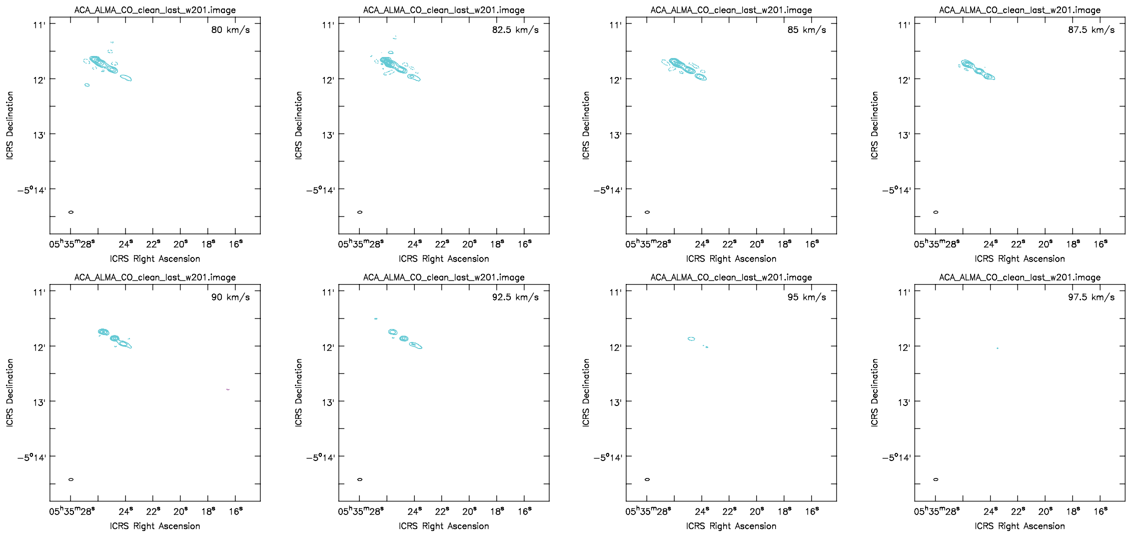

Figure 4.10: CO: Combined with ALMA 12m and ACA. The contour level starts at 5σ, [-5, 5, 10, 20, 40, 60, 80, 100, 150, 200] (1σ for the continuum image is 14.7 mJy beam^{-1}.) SiO: Combined with ALMA 12m and ACA. The contour level starts at 5σ, [-5, 5, 10, 20, 40, 60, 80, 100, 150, 200] (1σ for the continuum image is 13.1 mJy beam^{-1}.) The beam size is indicated by a circle in each panel.

4.3 H_2 jet and Bow Shock

OMC-2/FIR 6 is an active star forming region where multiple cores/clumps are formed along the filament and the outflows are known to be driven. Previous studies have shown that H_2 jet is detected in FIR 6/OMC-2 (Stanke et al. 2002). I confirmed the consistency between Stanke et al. (2002) and my ALMA observations. Figure 4.11 left panel shows the moment 1 (velocity) map in CO J = 2–1 of OMC-2/FIR 6 with my ALMA observation overlaid on the moment 0 (integrated intensity) map with the contours. The right panel shows the observation of H_2 in the same region observed by Stanke et al. (2002). In the right panel, objects 21, 22, 23, 24 and 25 correspond to H_2 jet. According to Stanke et al. (2002), for objects 21 and 22, there is a chain of compact structure in the North–South direction, while the driving source was not found. In my observation area, the CO emission is also detected around $v_{\rm sys}$ (5 km s^{-1} to 32.5 km s^{-1}; see Figure A.3). These CO emissions are likely to corresponding to 21 and 22 H_2 jets. However, there is no core candidate in my observation area that could be considered as the driving source of the CO emission.

The H_2 jet 23 in the right panel corresponds to the outflow driven from FIR 6 – ALMA 13. In addition, for the outflow of FIR 6 – ALMA 13, H_2 jet is corresponds to the emission of CO J = 2–1 and SiO J = 5–4. There is a strong emission in the lowermost side of the H_2 jet 23, and the bow-shock like structure is expected to be formed (Stanke et al. 2002). From FIR 6 – ALMA 13, such a structure is seen in the south side of the redshifted component (Figure 4.12). Around 12.5 km s^{-1}, I can see a bow shock clearly, which is consistent with the position of bow shock in the observation of H_2. FIR 6 – ALMA 13 has a very strong and energetic outflow/jet because outflow is detected by CO and SiO, H_2 and bow shock. On the other hand, the driving of extremely high velocity flow like FIR 6 – ALMA 5 has not been detected. FIR 6 – ALMA 13 corresponds to HOPS 60 and it has the inclination angle about 89° (Furlan et al. 2016). Since the angle is almost edge on, it is difficult to detach the high velocity from the low velocity components. Because both SiO and H_2 jet were detected, this outflow can be considered to be a high velocity jet.

24 H_2 jet corresponds to the observation in FIR 6 – ALMA 5 (the right panel of Figure 4.11). In addition, I could detect the same components as 25 H_2 jet at low velocity from my ALMA observations. The marginal component seen on the blueshifted side edge of FIR 6 – ALMA 5 is likely to match with 25 H_2 jet. Therefore, the component that unnaturally exists on the edge of blueshifted side in FIR 6-ALMA 5 outflow is H_2 jet confirmed by Stanke et al. (2002). The driving source of the 25 H_2 jet are not known and it can be considered that the slight interacting component is formed by the the collision of FIR 6 – ALMA 5 and 25 H_2 jet.

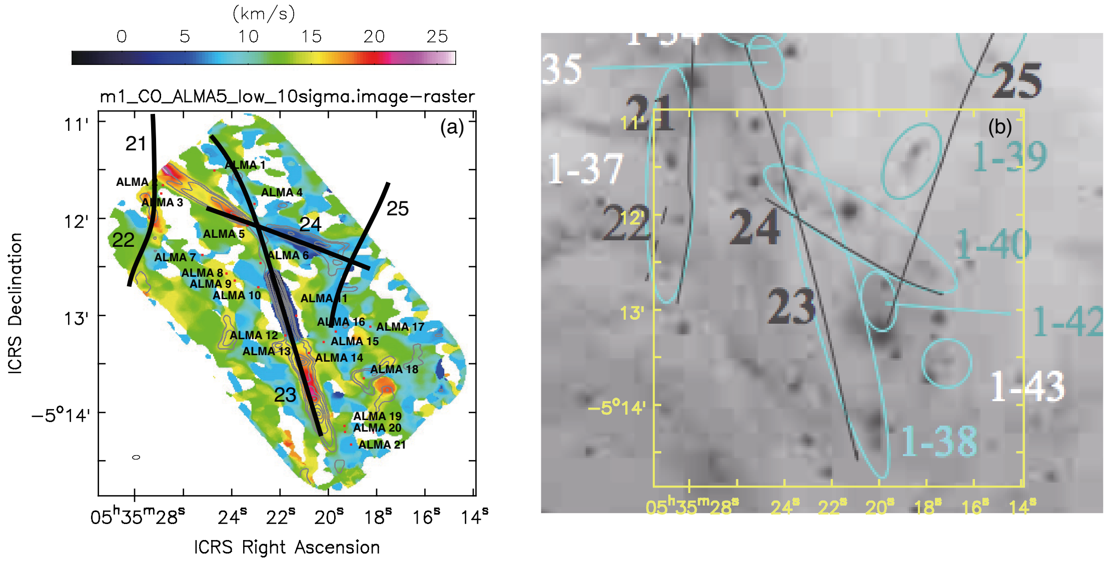

Figure 4.11: Left panel shows the CO moment 1 map overlaid the CO moment 0 map with gray contour and the continuum peak position with red dots. The beam size is indicated by a circle in each panel. The contour level starts at 5σ, [5, 10, 20, 30, 40, 50] (1σ for the continuum image is 0.0147 Jy beam^{-1}. Right panel shows the H_2 jet (Stanke et al. 2002) image overlaid the this ALMA observation region with yellow line.

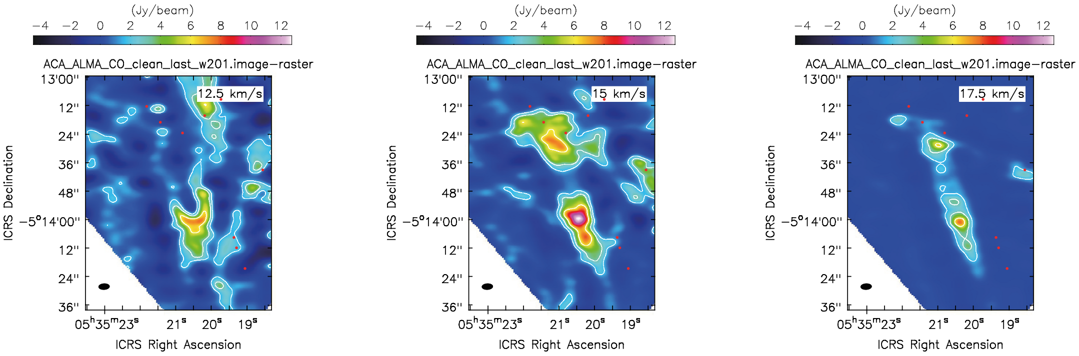

Figure 4.12: CO channel map combined with ALMA 12m and ACA. The beam size is indicated by a circle in each panel. The contour level starts at 5σ, [5, 10, 20, 30] (1σ for the continuum image is 0.01 Jy beam^{-1}. The bow shock structure associated with FIR 6 – ALMA 13.

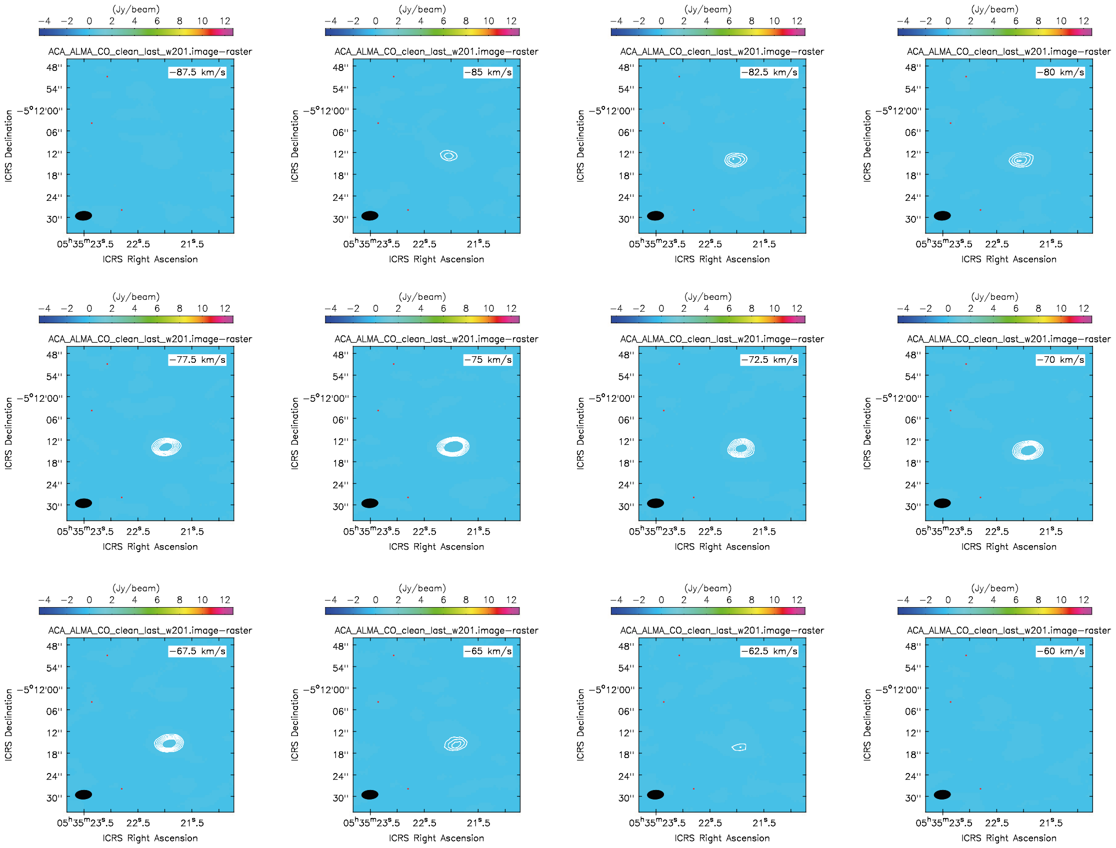

Figure 4.13: CO channel map combined with ALMA 12m and ACA. The beam size is indicated by a circle in each panel. The contour level starts at 5σ, [5, 6, 7, 8, 9, 10] (1σ for the continuum image is 0.02 Jy beam^{-1}. The blue-shifted high-velocity component associated with FIR 6 – ALMA 5.

Chapter 5

SUMMARY

1.3 mm continuum, CO $J = 2$–1 and SiO $J = 5$–4 molecular line emissions with high resolution observation have been carried out using ALMA toward the OMC-2/FIR 6 southern filament. The observation has done with a mosaic of 110 points covering approximately 90 arcsec × 180 arcsec. All the data in this thesis is combined with ACA 7 m array and ALMA 12 m array configurations, and I achieved the high angular resolution about 4.5 arcsec × 2.5 arcsec. The main results are summarized as following.

1. 21 dust continuum sources have been discovered and sufficiently spatially resolved with an H_2 mass between ~ 0.02 to 0.9 $M_\odot$ with 1.3 mm ALMA observation. I identified 1.3 mm continuum sources, which are correspond to 11 previously known sources and 10 new additional sources. In OMC-2/FIR 6, the detected sources have various evolutionary stages, starless core, Class 0 and Class II phases. I compared the 1.3 mm continuum, CO and SiO in my observation with previous infrared observation. As a results, 10/21 ($\sim$ 48 %) continuum sources are associated with infrared sources, and at least 5/21 ($\sim$ 24 %) continuum sources have molecular outflow (up to 9/21, $\sim$ 43 %). Thus, OMC-2/FIR 6 is a very young star formation region and it is expected that there are many starless cores.

2. At least five continuum sources (up to nine sources) have CO $J = 2$–1 outflow and one continuum source has SiO $J = 5$–4 outflow. Moreover, one continuum source has the Extremely High Velocity (EHV) flow. Both CO and SiO emissions were detected in only FIR 6 – ALMA 13, and the CO EHV flow was observed in FIR 6 – ALMA 5. FIR 6 – ALMA 5 and FIR 6 – ALMA 13 clearly show red- and blueshifted bipolar outflow. These two outflows are known in previous studies. In addition, I presented the discovery of 7 new additional outflows. FIR 6 – ALMA 1 and FIR 6 – ALMA 18 have a marginally outflow, and other five continuum sources have mono-polar (non bipolar) outflow. The complication of the CO line emission is attributed to the contamination from the ambient molecular cloud. Thus, it is difficult to distinguish outflow from other components. Three outflows are associated with the Class II (flat) source, the

two outflows are with Class 0 source and the four outflow are with starless core. The most strong and energetic outflow is driven from the Class 0 source, and weak outflow is likely associated with starless core or Class II source. Therefore, Class 0 sources have most actively outflow.

3. I classified the 1.3 mm continuum sources discovered by my ALMA observation into starless core, Class 0, Class I, and Class II phase. In total, 12 sources are starless core, two sources are between starless to Class 0 phase (they are pretty younger than Class 0), two are Class 0 phase, and three are Class II phase. The 1.3 mm continuum sources is concentrated in the bent part (called, hub) of the filament where FIR 6 – ALMA 12, 13, 14, 15, and 16 exists. In addition, these cores have a various ages/evolutionary stages, from starless to Class II. It is known that a large amount of gas flows into the hub of the filament and the star formation is more active than other non-hub regions. Thus, I can see the such feeding process in this hub of filament.

Appendix A

APPENDIX

CO Channel Map

All channel maps for CO J = 2–1 from -100 km s^{-1} to 97.5 km s^{-1} are listed below from Figure. A.1 to Figure. A.4. The velocity range was created in increments of 2.5 km s^{-1}. The red dots correspond to continuum souces (ALMA ID).

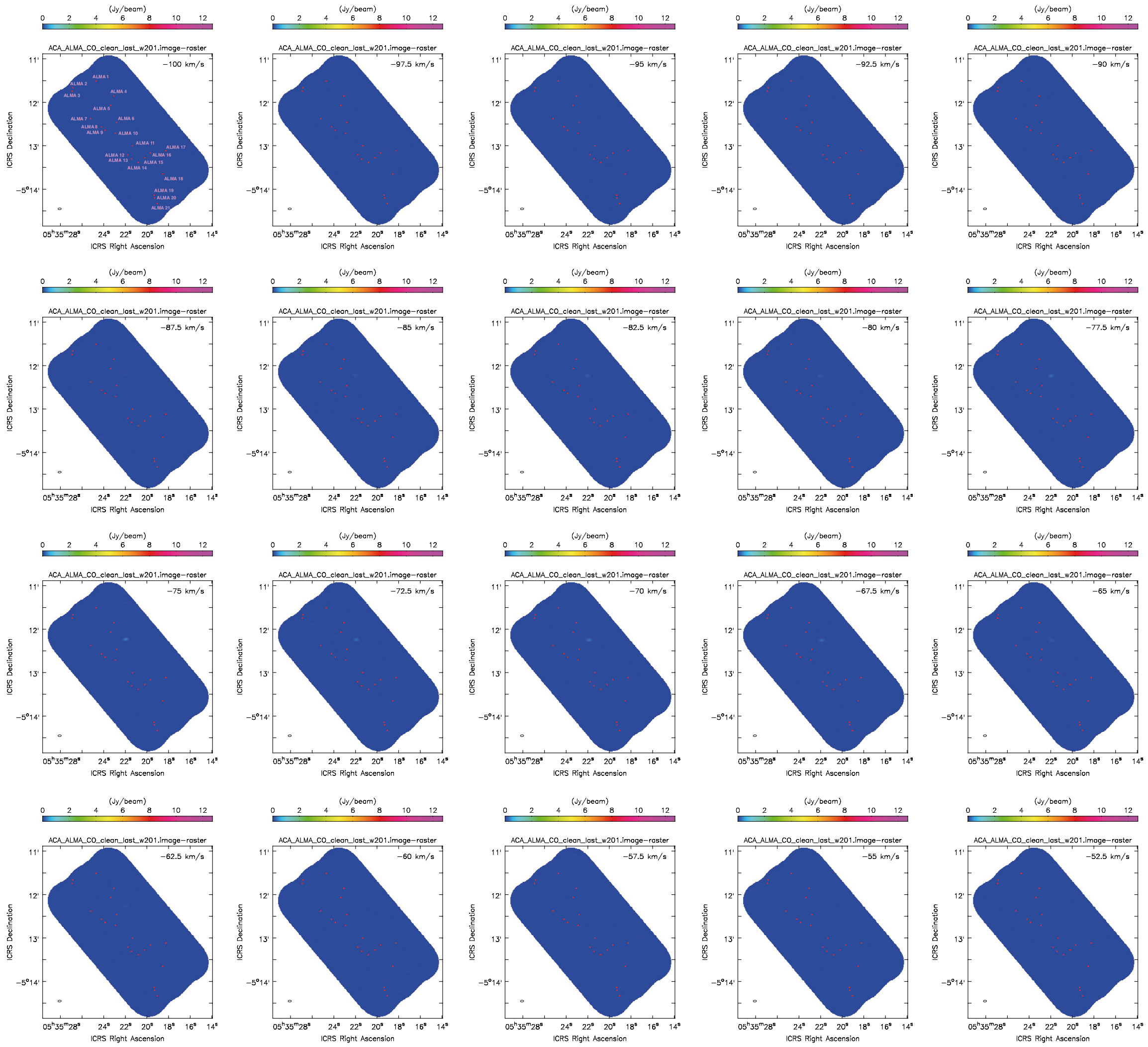

Figure A.1: This figure shows CO velocity channel map combined with ALMA 12m and ACA. We described the velocity from -100 km s^{-1} to -52.5 km s^{-1}. The beam size is indicated by a circle in each panel.

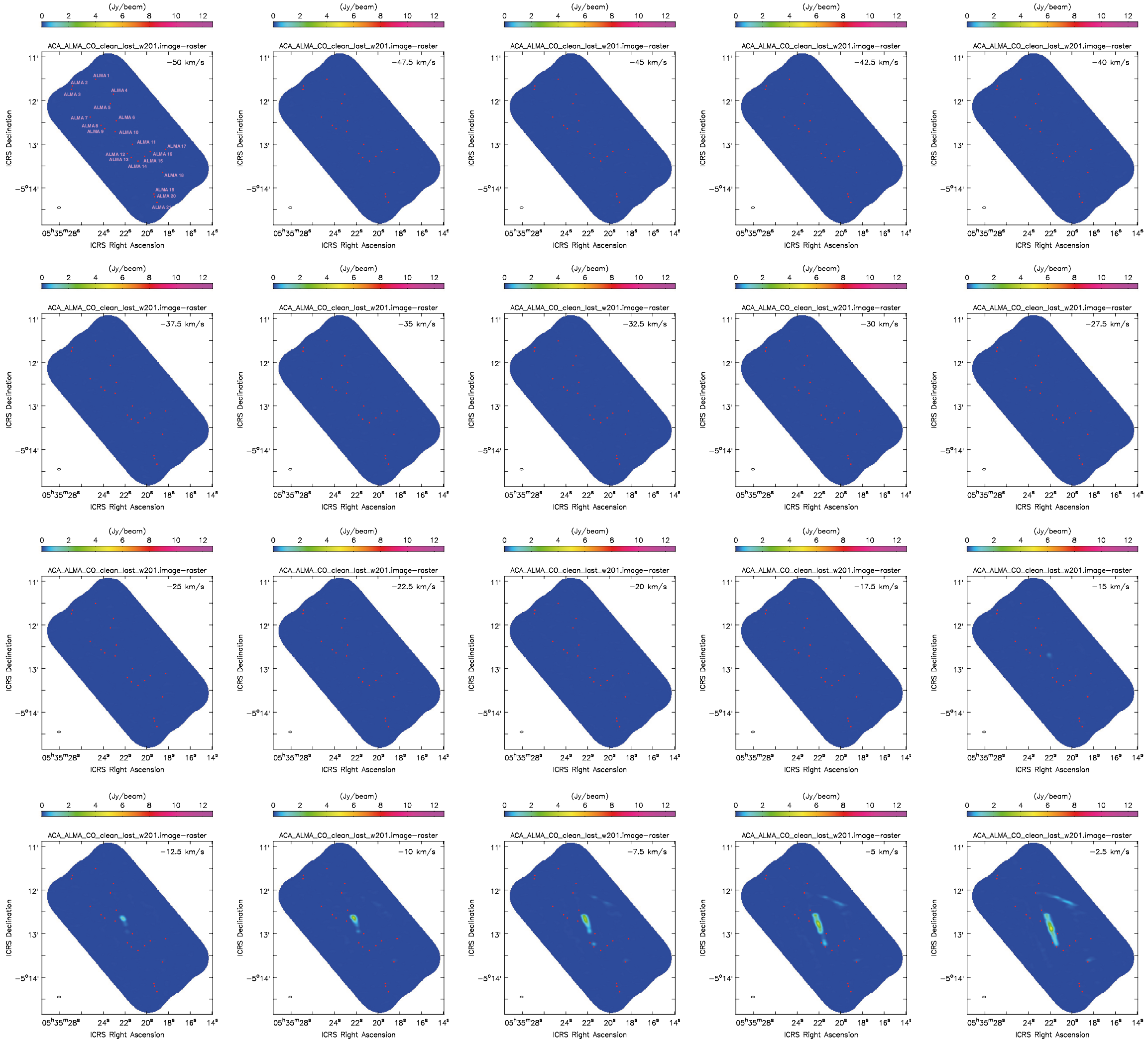

Figure A.2: This figure shows CO velocity channel map combined with ALMA 12m and ACA. We described the velocity from -50 km s^{-1} to -2.5 km s^{-1}. The beam size is indicated by a circle in each panel.

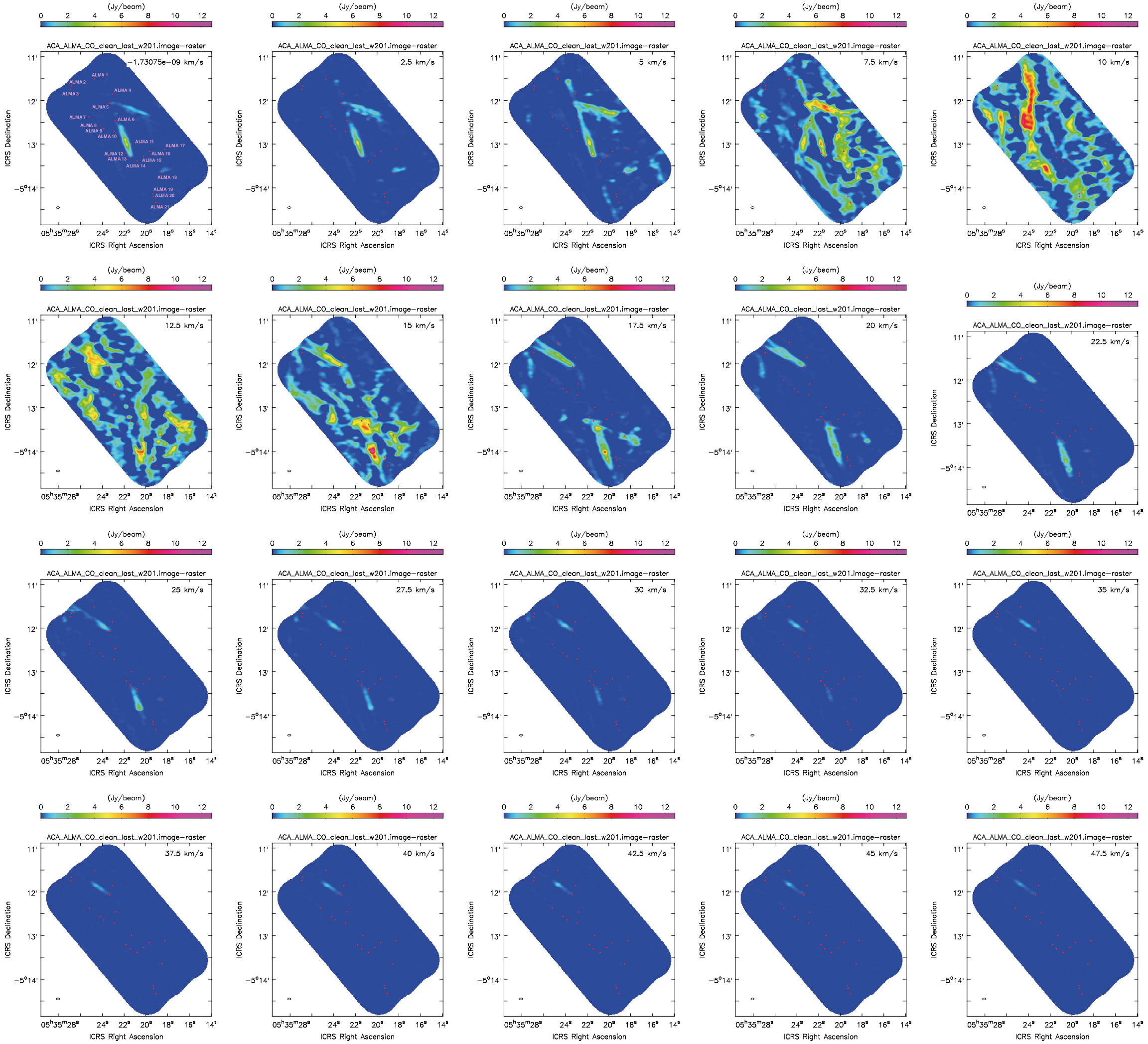

Figure A.3: This figure shows CO velocity channel map combined with ALMA 12m and ACA. We described the velocity from 0 km s^{-1} to 47.5 km s^{-1}. The beam size is indicated by a circle in each panel.

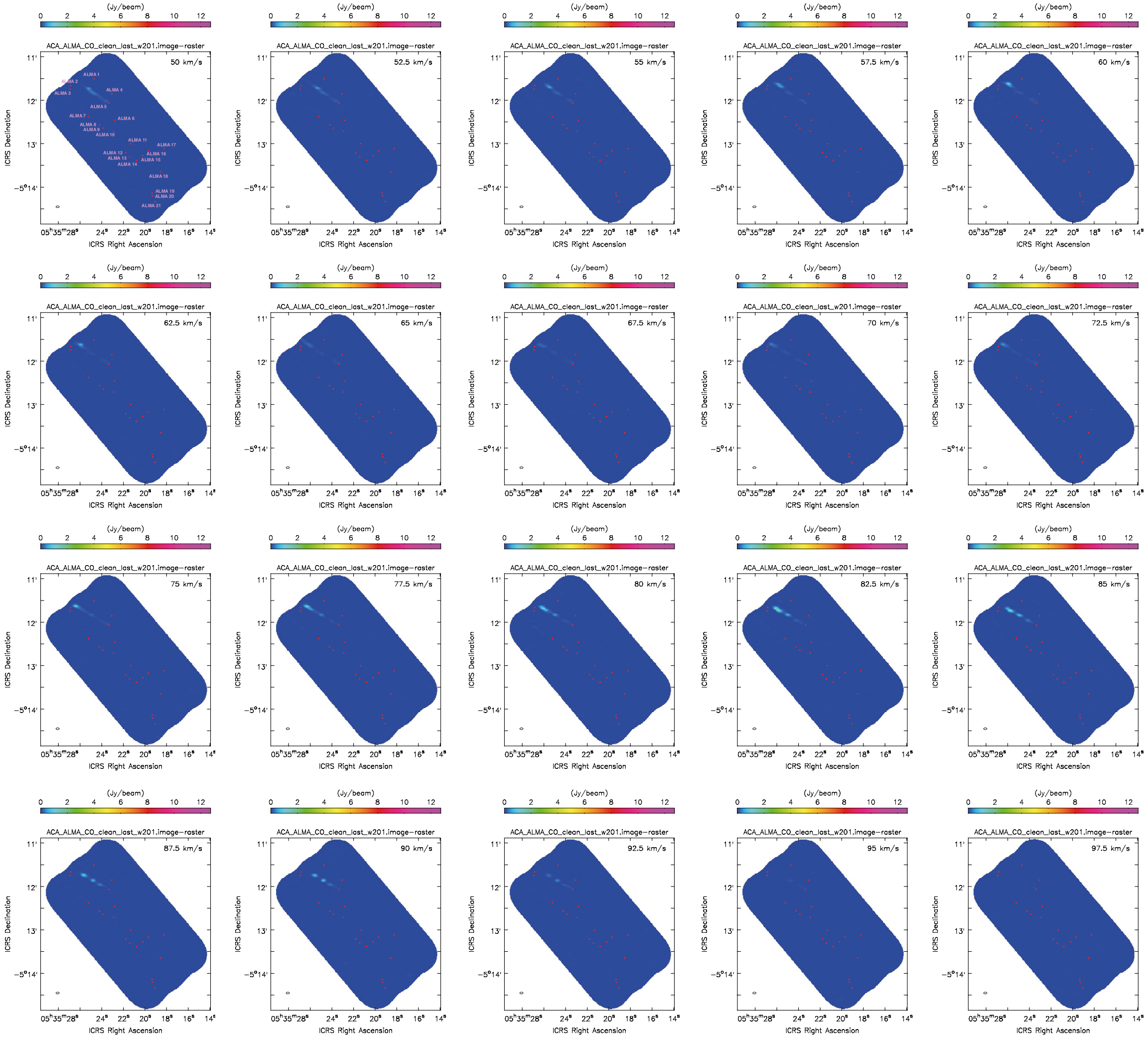

Figure A.4: This figure shows CO velocity channel map combined with ALMA 12m and ACA. We described the velocity from 50 km s^{-1} to 97.5 km s^{-1}. The beam size is indicated by a circle in each panel.

SiO Channel Map

All channel maps for SiO J = 5–4 from -100 km s^{-1} to 97.5 km s^{-1} are listed below from Figure. A.5 to Figure. A.8. The velocity range was created in increments of 2.5 km s^{-1}. The red dots correspond to continuum souces (ALMA ID).

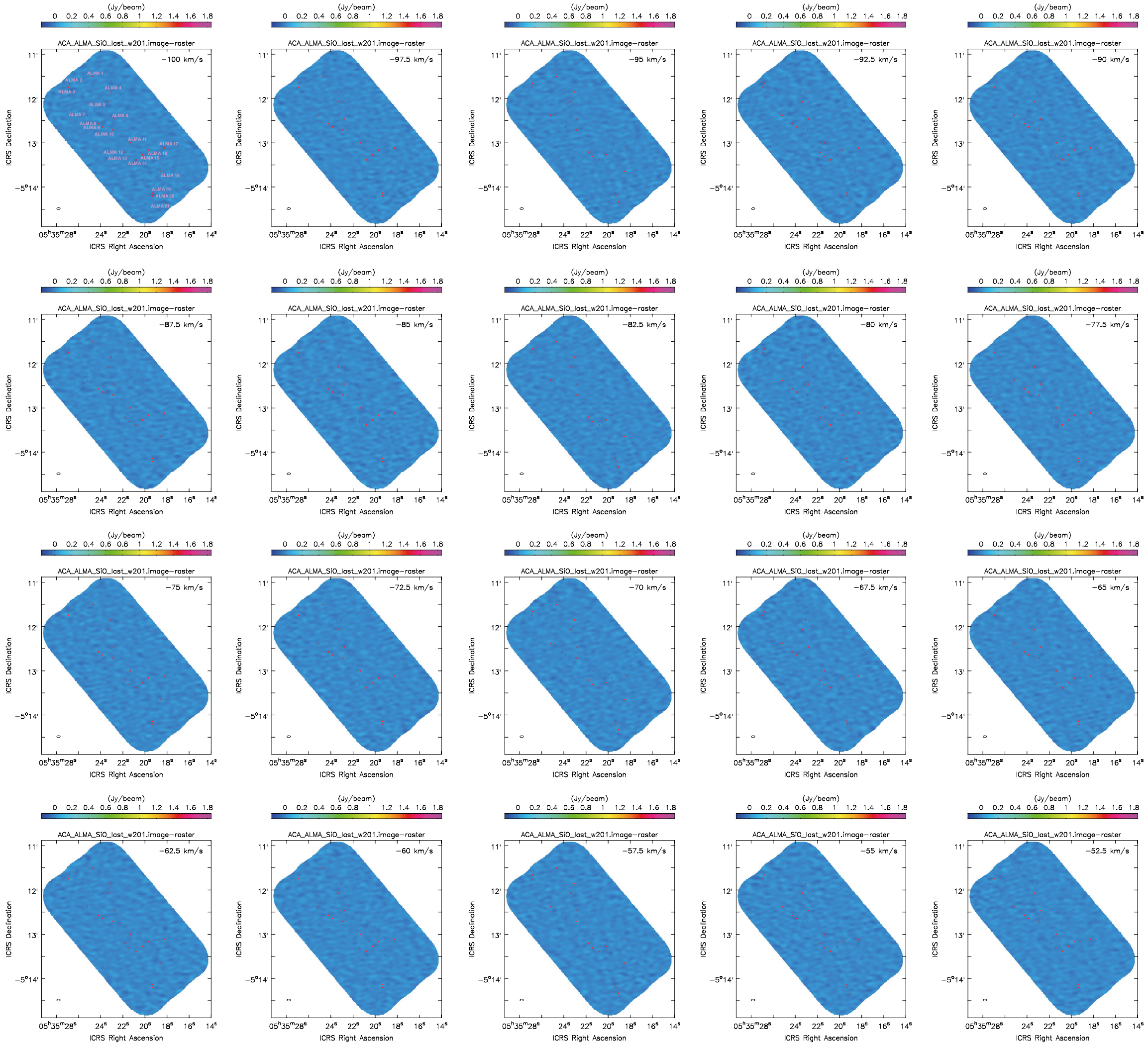

Figure A.5: This figure shows SiO velocity channel map combined with ALMA 12m and ACA. We described the velocity from -100 km s^{-1} to -52.5 km s^{-1}. The beam size is indicated by a circle in each panel.

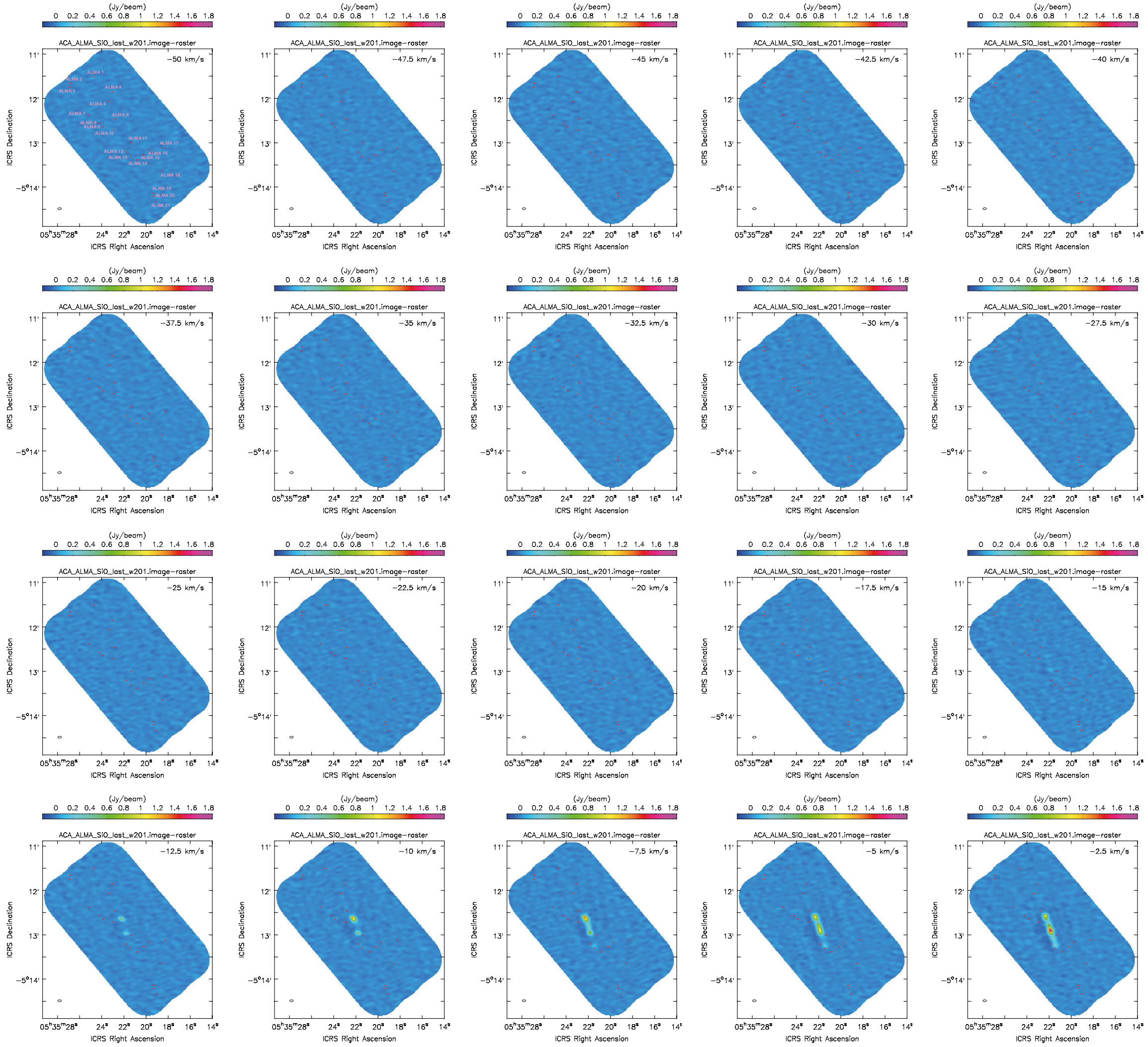

Figure A.6: This figure shows SiO velocity channel map combined with ALMA 12m and ACA. We described the velocity from -50 km s^{-1} to -2.5 km s^{-1}. The beam size is indicated by a circle in each panel.

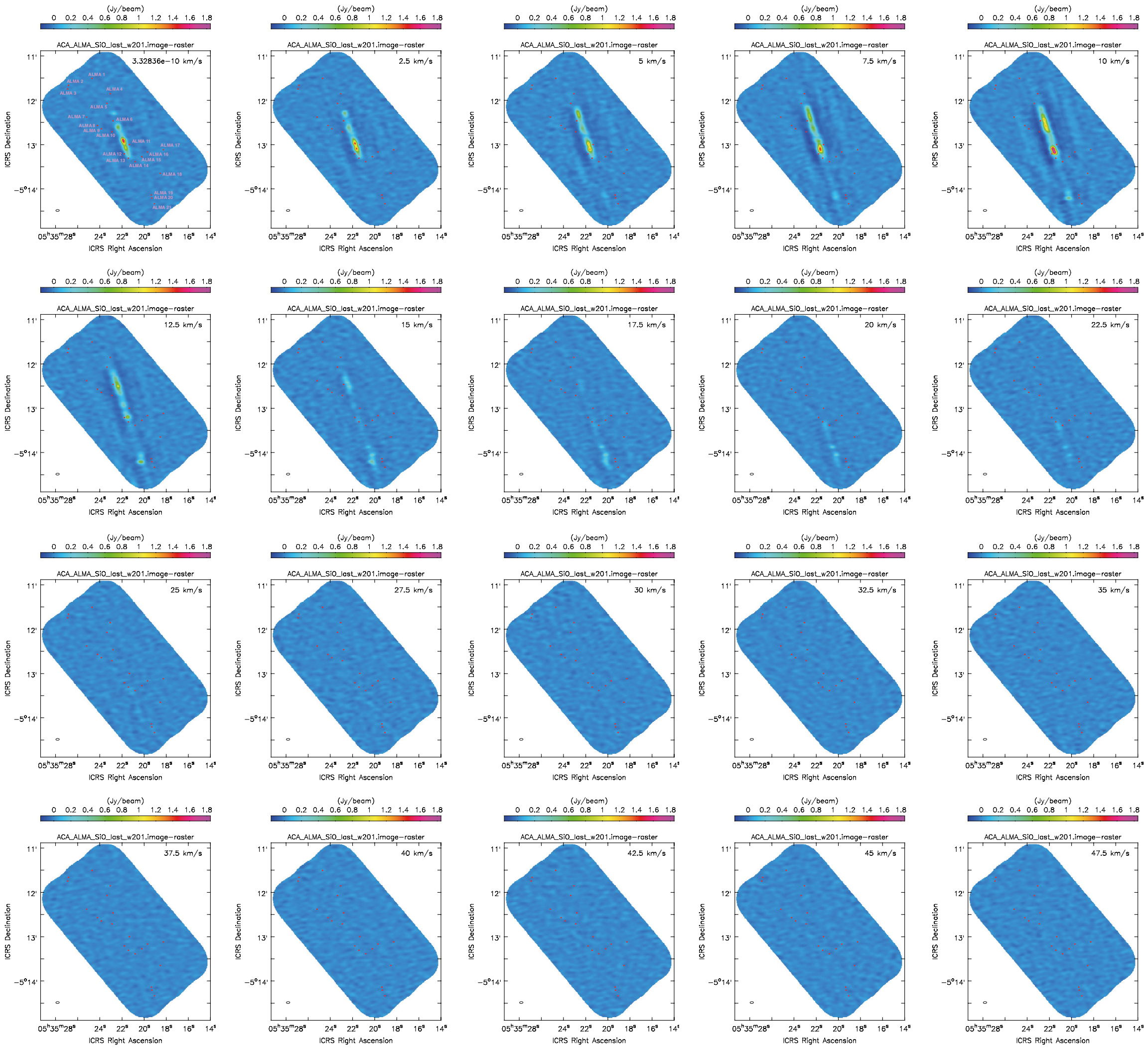

Figure A.7: This figure shows SiO velocity channel map combined with ALMA 12m and ACA. We described the velocity from 0 km s^{-1} to 47.5 km s^{-1}. The beam size is indicated by a circle in each panel.

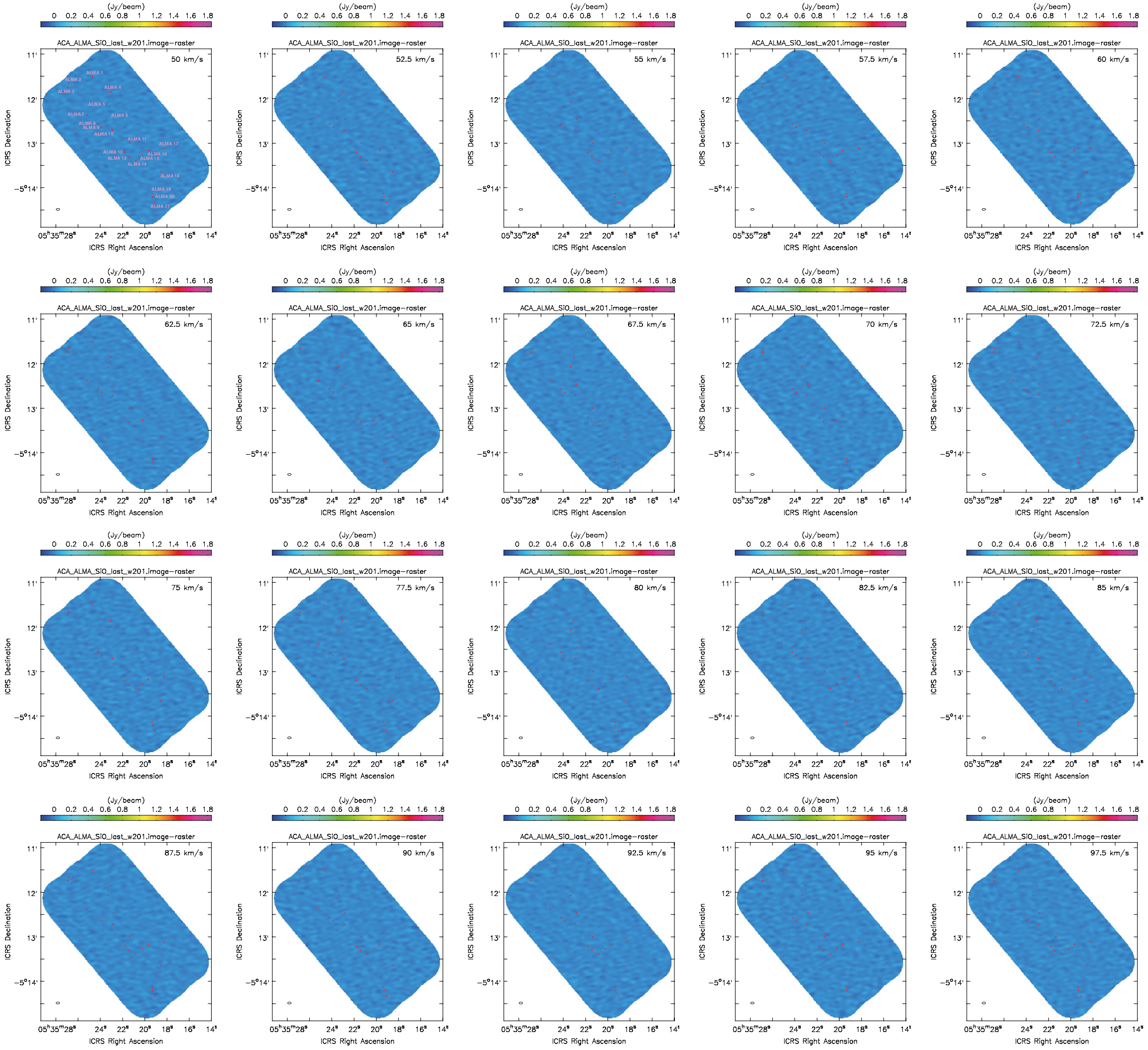

Figure A.8: This figure shows SiO velocity channel map combined with ALMA 12m and ACA. We described the velocity from 50 km s^{-1} to 97.5 km s^{-1}. The beam size is indicated by a circle in each panel.

CO Low Velocity Complex Structure

This is a channel map with only low velocity component of CO J = 2–1 from Figure. A.9 to Figure. A.22. In the vicinity of the system velocity, many components are complexly mixed, so the OMC-2 / FIR 6 area was divided up/bottom and an enlarged image was created. The velocity range was created in increments of 1 km s^{-1}.

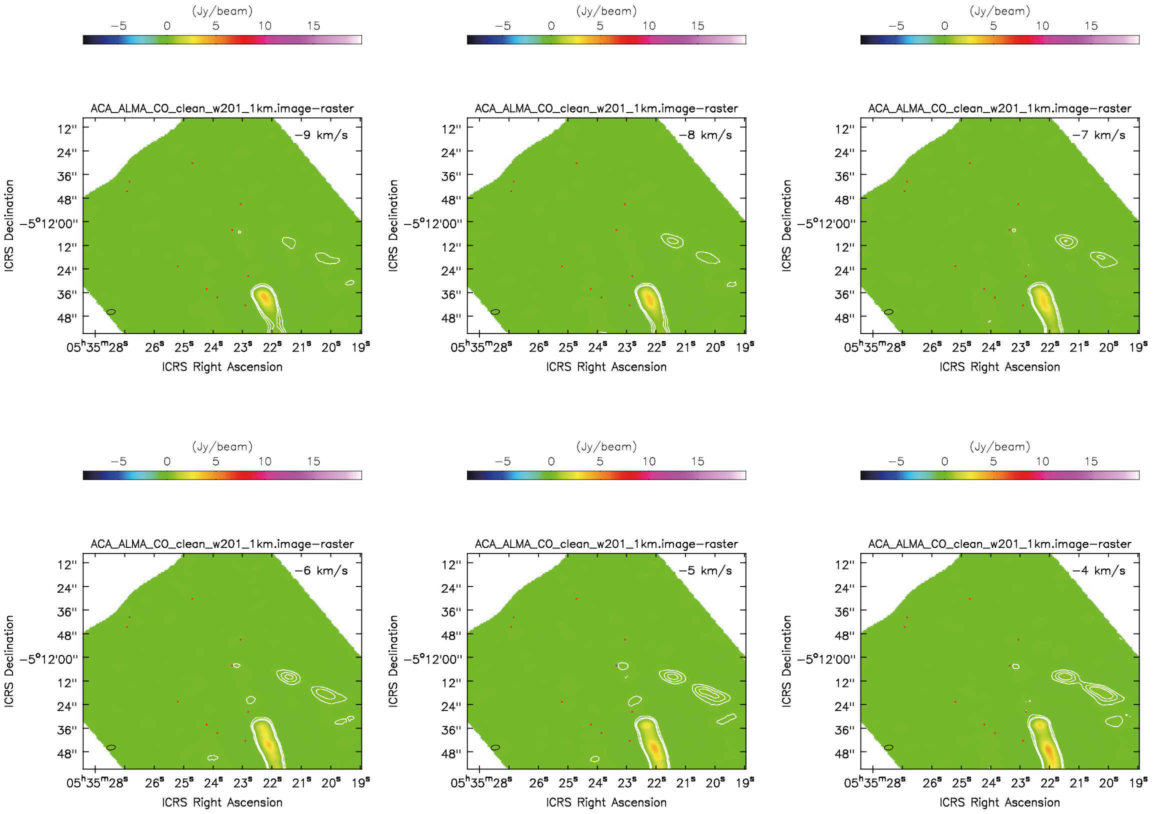

Figure A.9: CO: Combined with ALMA 12m and ACA. The contour level starts at 10σ, [10, 20, 30] (1σ for the continuum image is 14.7 mJy beam^{-1}.) The beam size is indicated by a circle in each panel. The red dots are the position of FIR–ALMA 1 to 21.

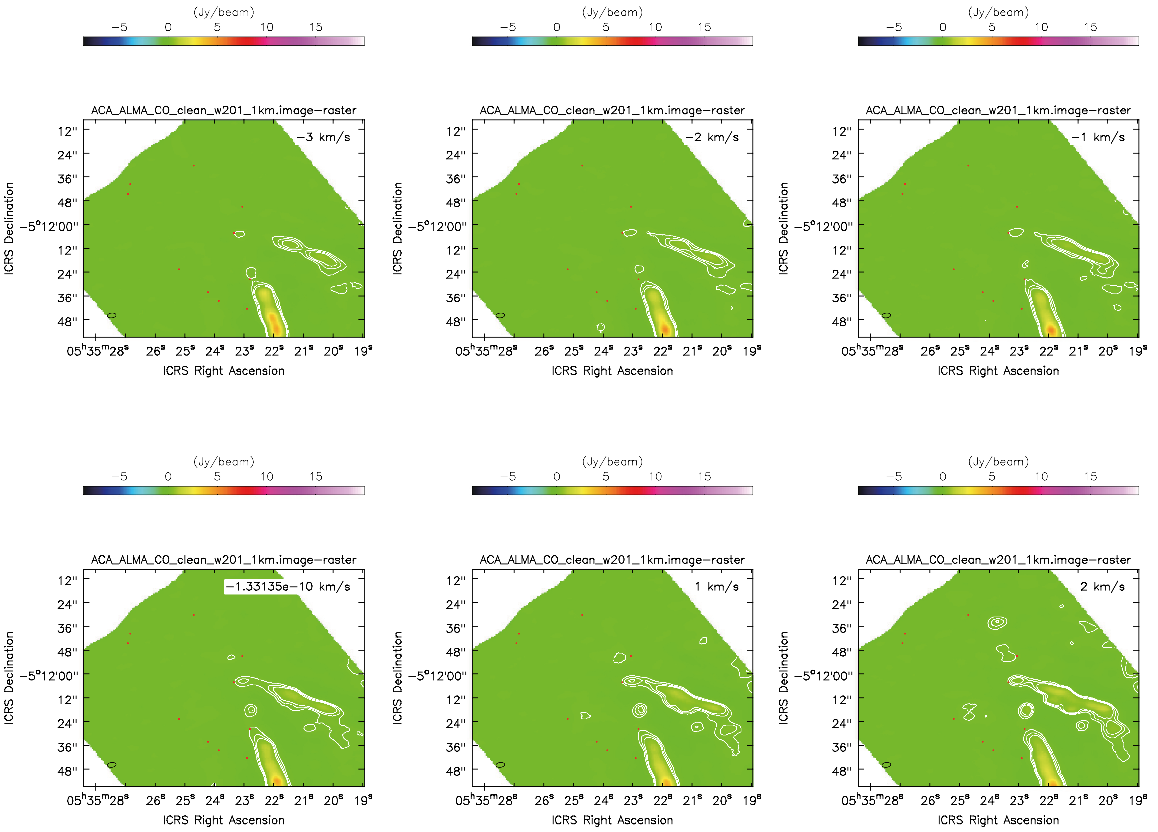

Figure A.10: CO: Combined with ALMA 12m and ACA. The contour level starts at 10σ, [10, 20, 30] (1σ for the continuum image is 14.7 mJy beam^{-1}.) The beam size is indicated by a circle in each panel. The red dots are the position of FIR–ALMA 1 to 21.

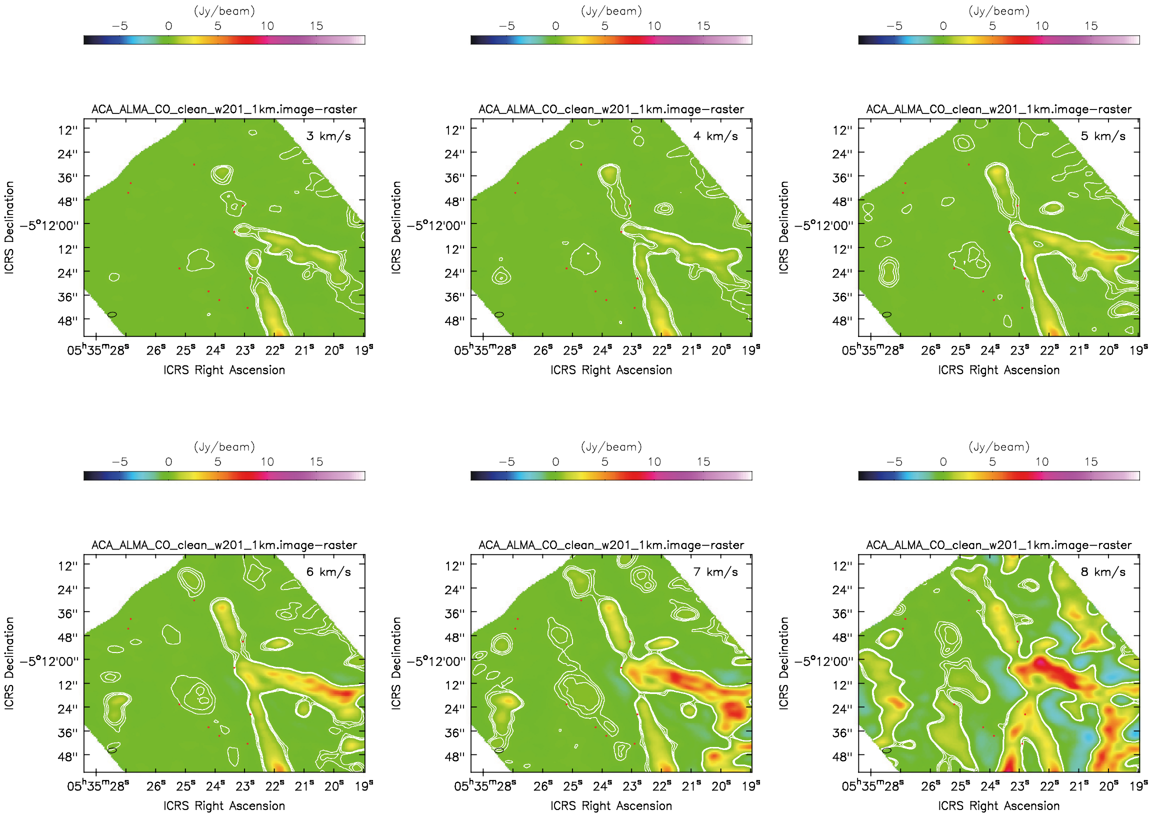

Figure A.11: CO: Combined with ALMA 12m and ACA. The contour level starts at 10σ, [10, 20, 30] (1σ for the continuum image is 14.7 mJy beam^{-1}.) The beam size is indicated by a circle in each panel. The red dots are the position of FIR–ALMA 1 to 21.

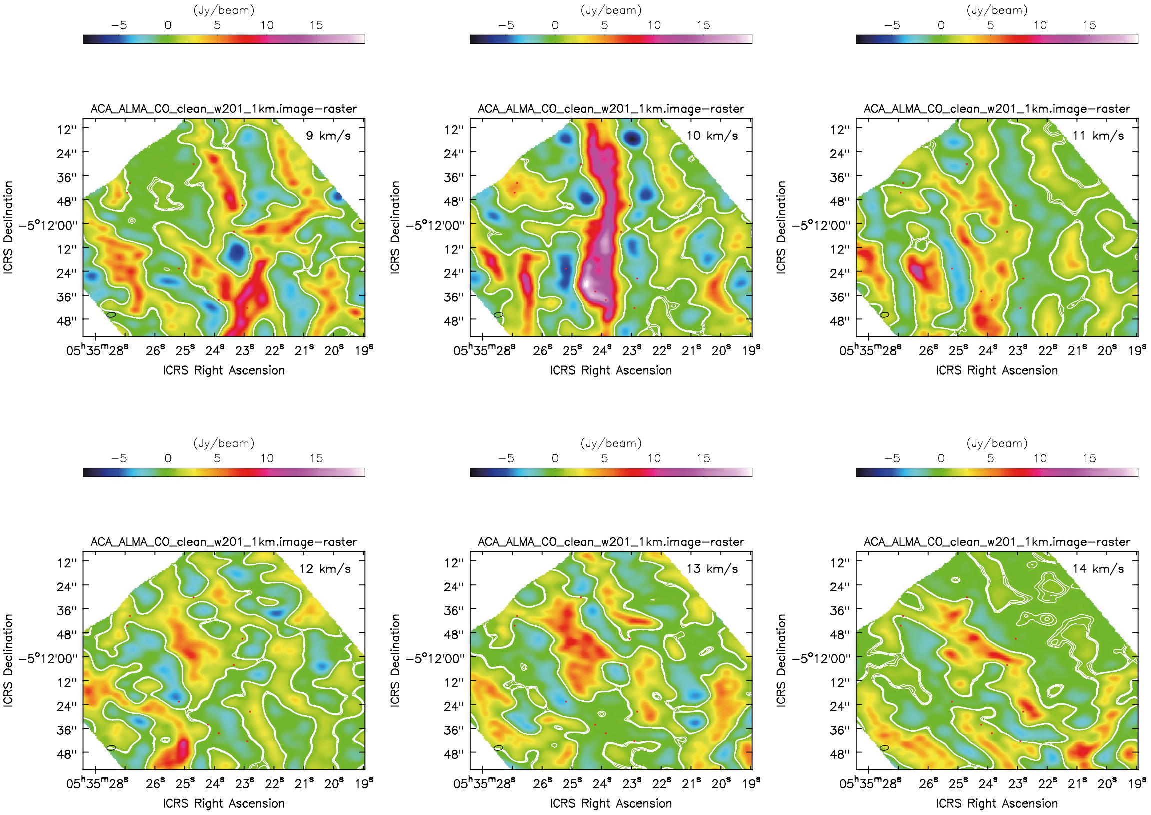

Figure A.12: CO: Combined with ALMA 12m and ACA. The contour level starts at 10σ, [10, 20, 30] (1σ for the continuum image is 14.7 mJy beam^{-1}.) The beam size is indicated by a circle in each panel. The red dots are the position of FIR–ALMA 1 to 21.

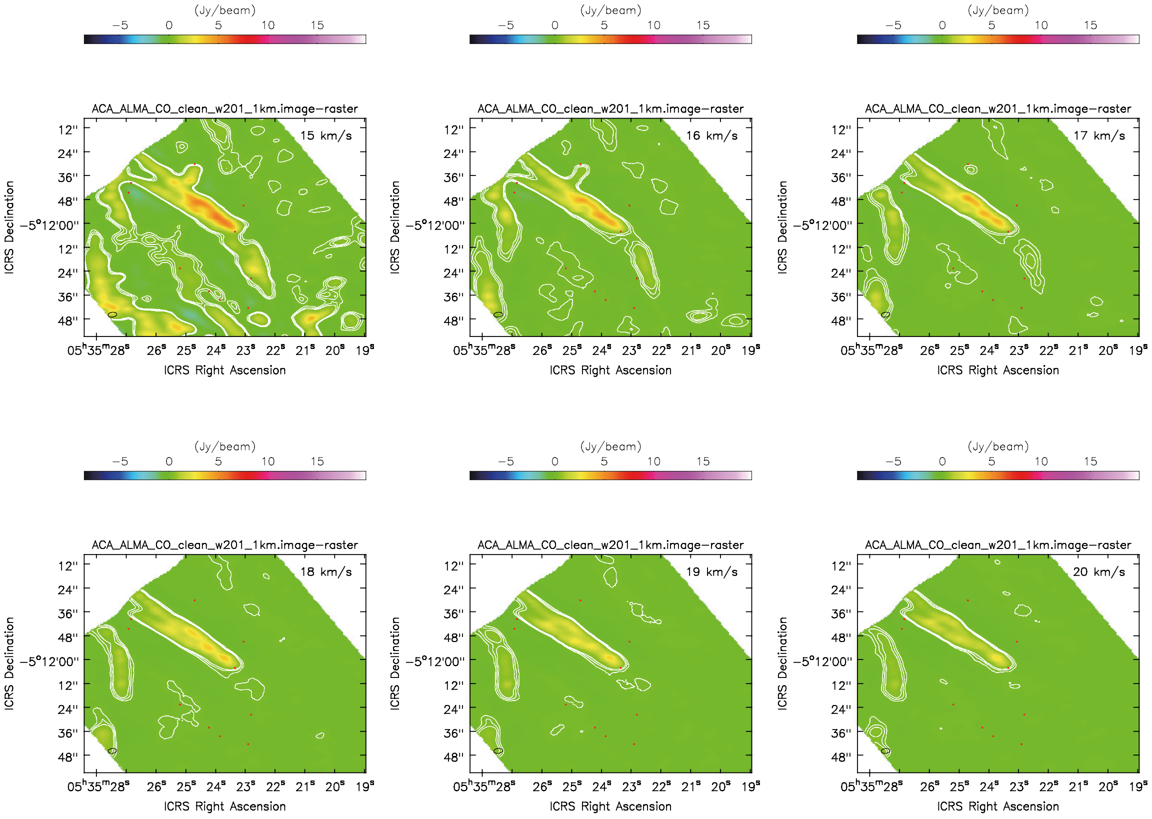

Figure A.13: CO: Combined with ALMA 12m and ACA. The contour level starts at 10σ, [10, 20, 30] (1σ for the continuum image is 14.7 mJy beam^{-1}.) The beam size is indicated by a circle in each panel. The red dots are the position of FIR–ALMA 1 to 21.

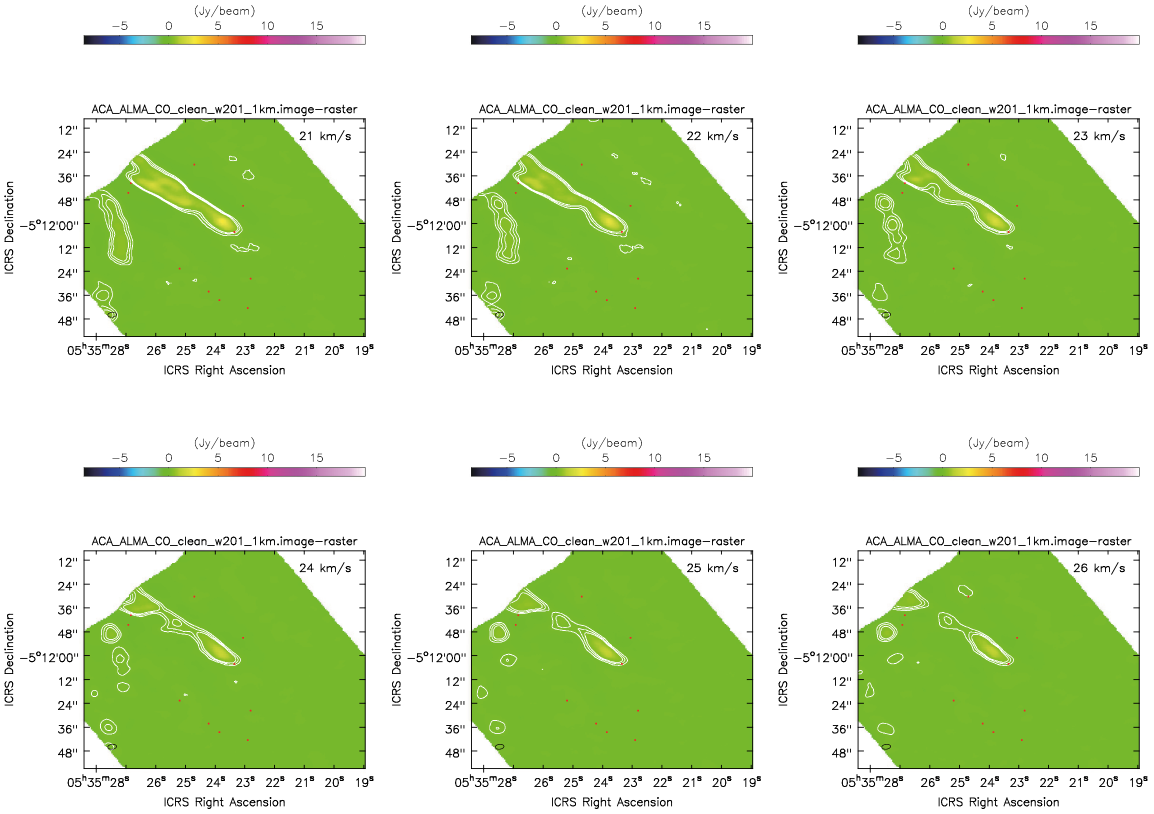

Figure A.14: CO: Combined with ALMA 12m and ACA. The contour level starts at 10σ, [10, 20, 30] (1σ for the continuum image is 14.7 mJy beam^{-1}.) The beam size is indicated by a circle in each panel. The red dots are the position of FIR–ALMA 1 to 21.

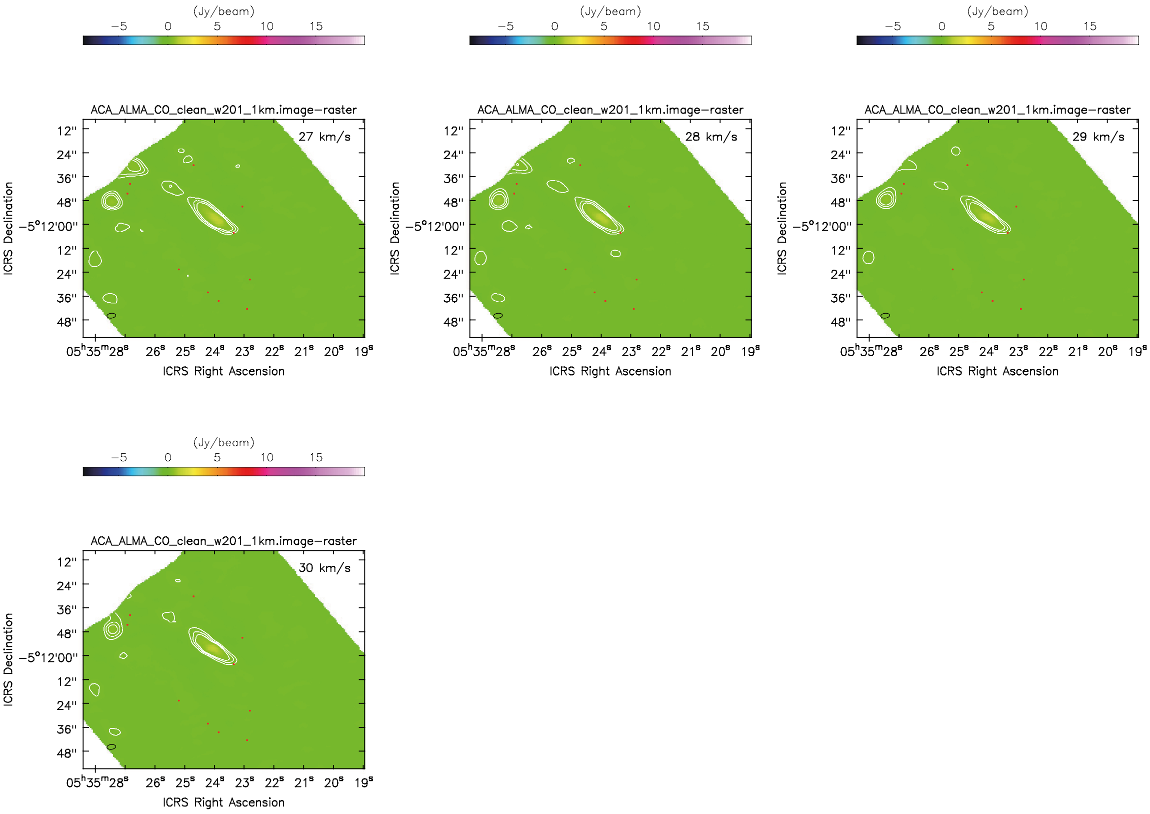

Figure A.15: CO: Combined with ALMA 12m and ACA. The contour level starts at 10σ, [10, 20, 30] (1σ for the continuum image is 14.7 mJy beam^{-1}.) The beam size is indicated by a circle in each panel. The red dots are the position of FIR–ALMA 1 to 21.

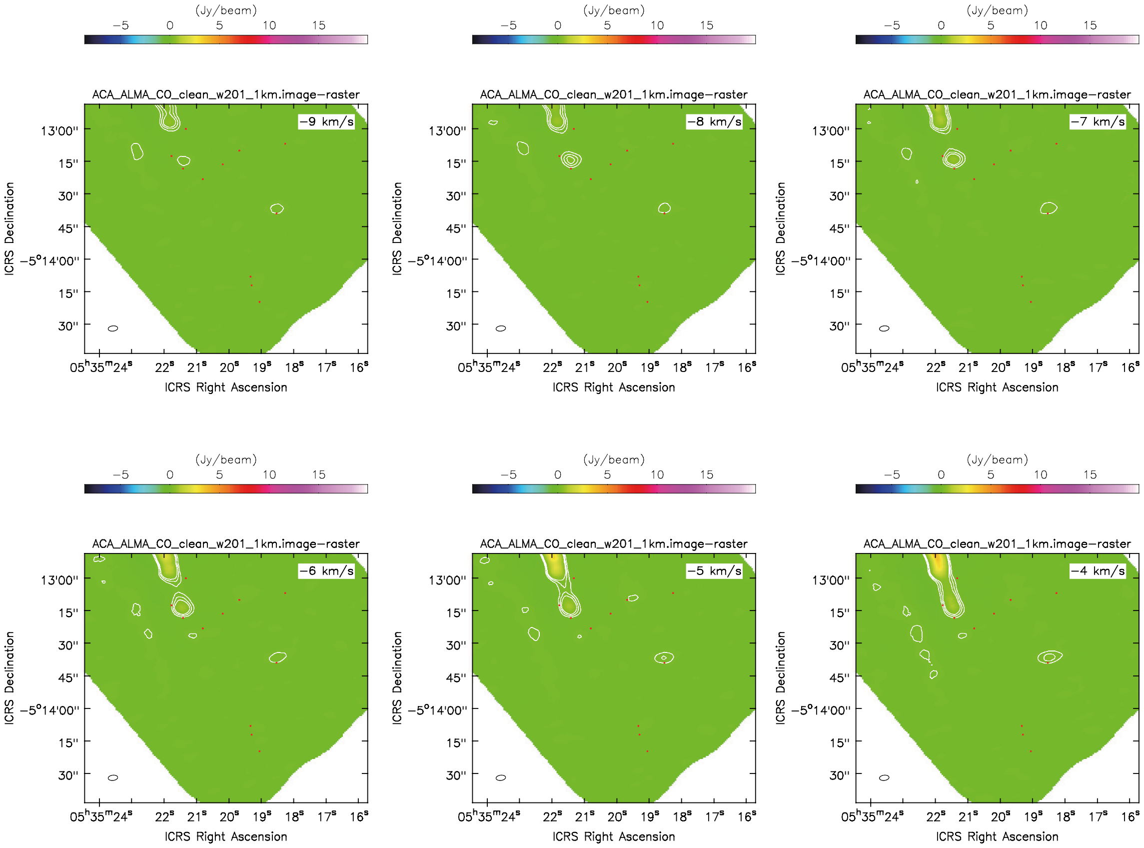

Figure A.16: CO: Combined with ALMA 12m and ACA. The contour level starts at 10σ, [10, 20, 30] (1σ for the continuum image is 14.7 mJy beam^{-1}.) The beam size is indicated by a circle in each panel. The red dots are the position of FIR–ALMA 1 to 21.

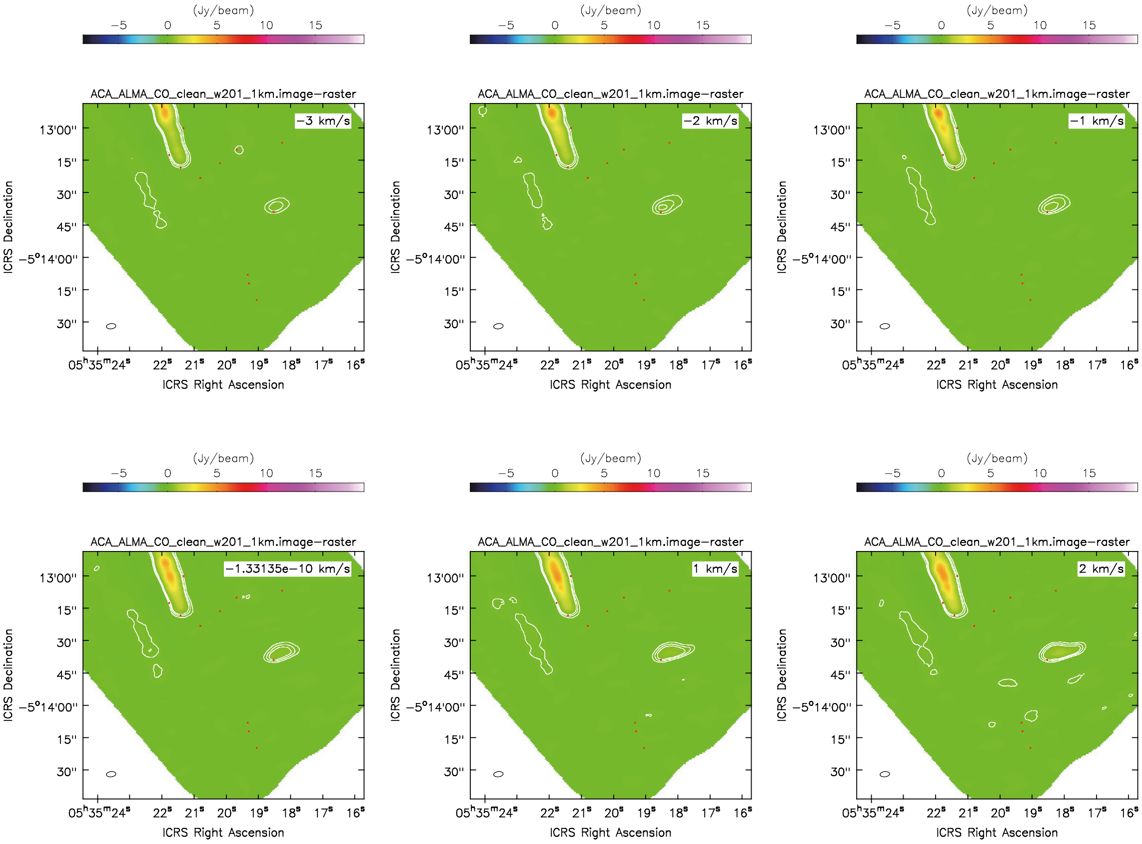

Figure A.17: CO: Combined with ALMA 12m and ACA. The contour level starts at 10σ, [10, 20, 30] (1σ for the continuum image is 14.7 mJy beam^{-1}.) The beam size is indicated by a circle in each panel. The red dots are the position of FIR–ALMA 1 to 21.

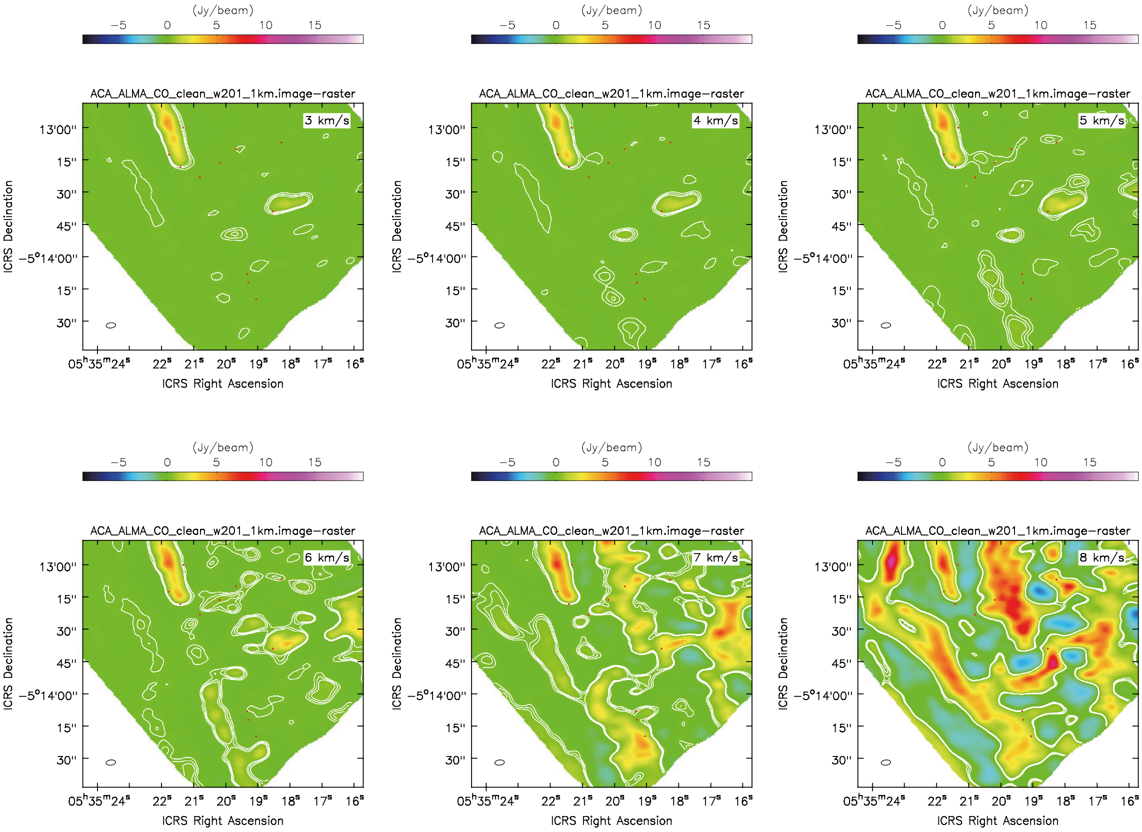

Figure A.18: CO: Combined with ALMA 12m and ACA. The contour level starts at 10σ, [10, 20, 30] (1σ for the continuum image is 14.7 mJy beam^{-1}.) The beam size is indicated by a circle in each panel. The red dots are the position of FIR–ALMA 1 to 21.

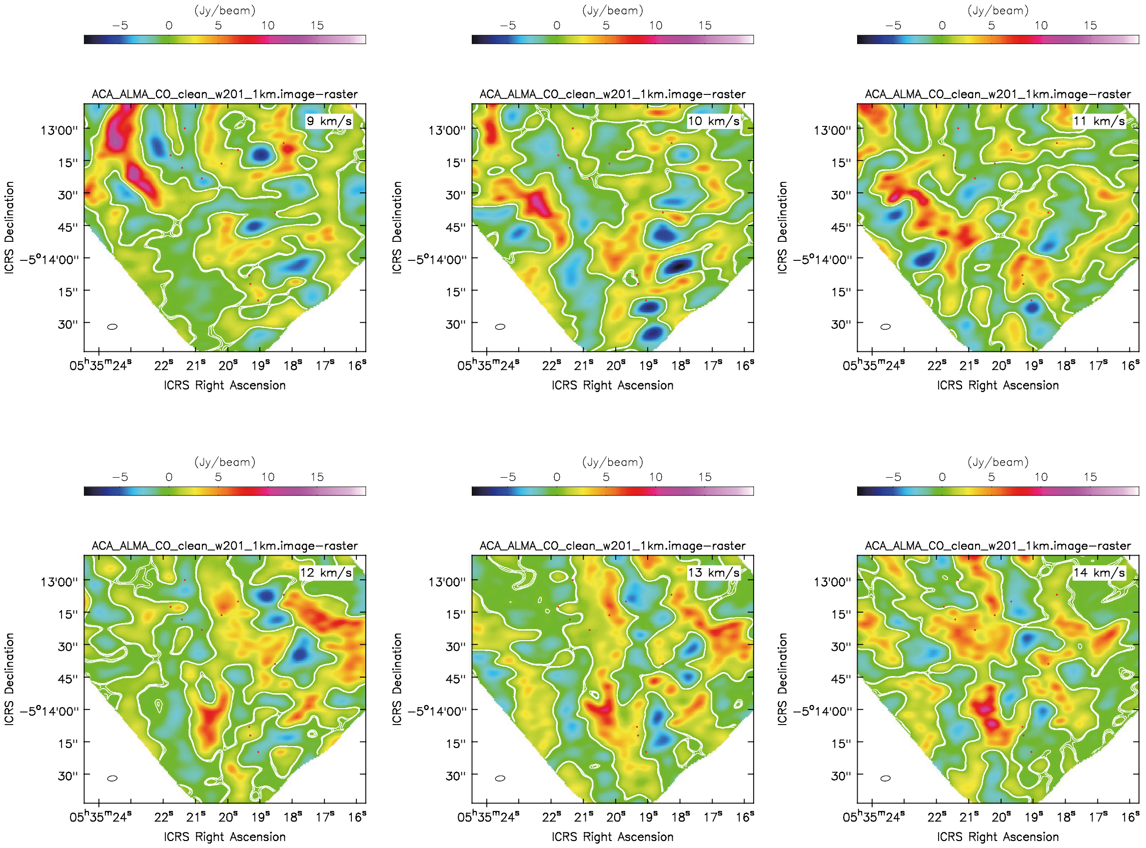

Figure A.19: CO: Combined with ALMA 12m and ACA. The contour level starts at 10σ, [10, 20, 30] (1σ for the continuum image is 14.7 mJy beam^{-1}.) The beam size is indicated by a circle in each panel. The red dots are the position of FIR–ALMA 1 to 21.

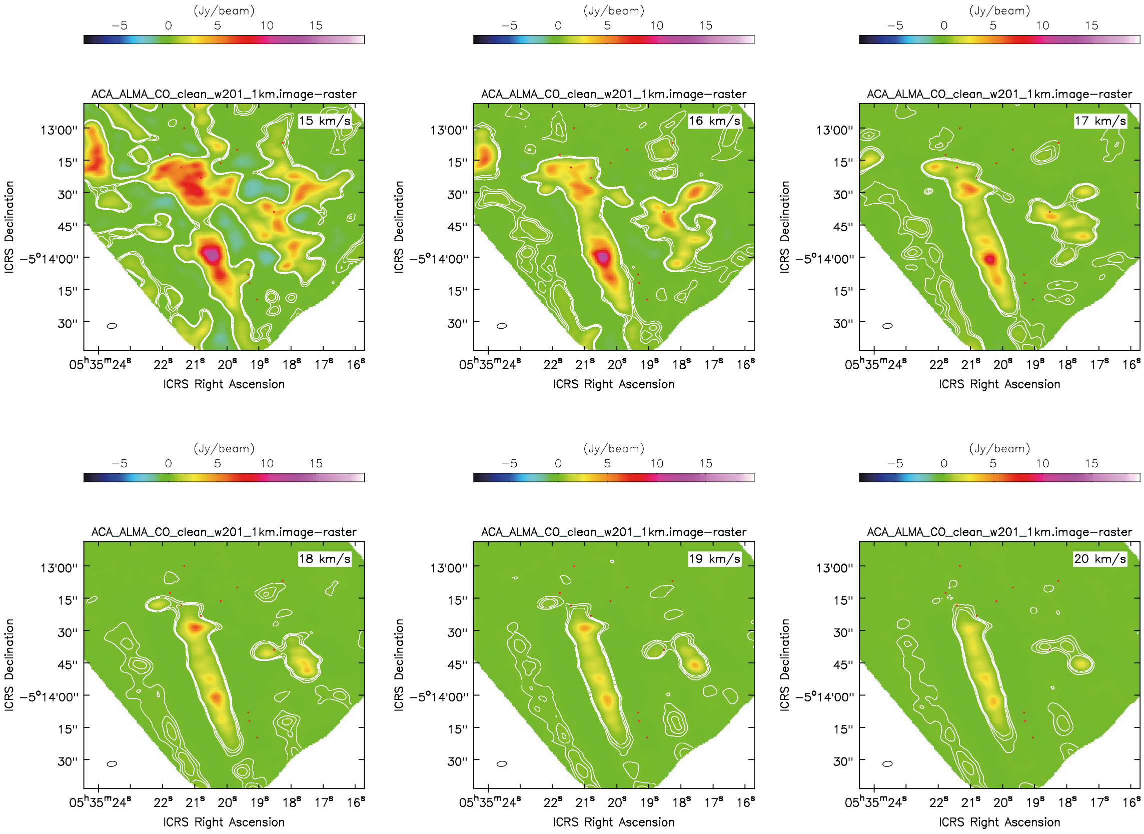

Figure A.20: CO: Combined with ALMA 12m and ACA. The contour level starts at 10σ, [10, 20, 30] (1σ for the continuum image is 14.7 mJy beam^{-1}.) The beam size is indicated by a circle in each panel. The red dots are the position of FIR–ALMA 1 to 21.

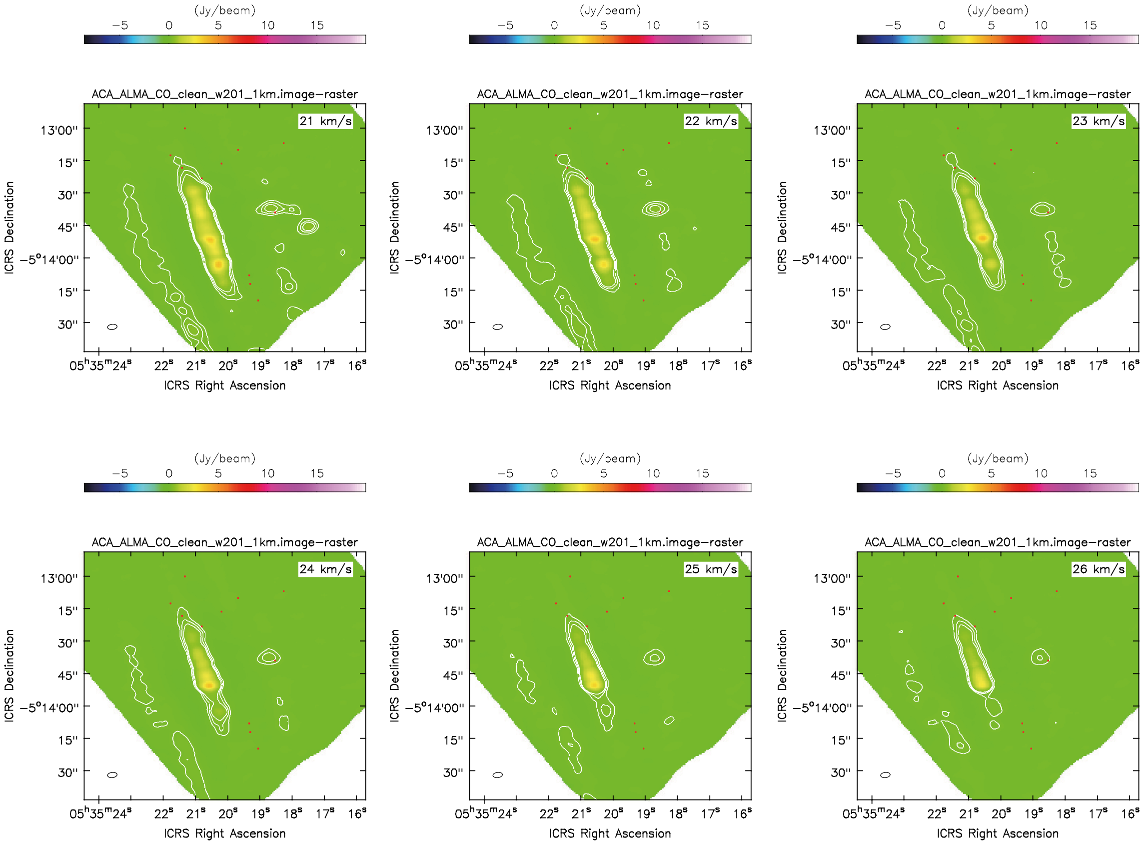

Figure A.21: CO: Combined with ALMA 12m and ACA. The contour level starts at 10σ, [10, 20, 30] (1σ for the continuum image is 14.7 mJy beam^{-1}.) The beam size is indicated by a circle in each panel. The red dots are the position of FIR–ALMA 1 to 21.

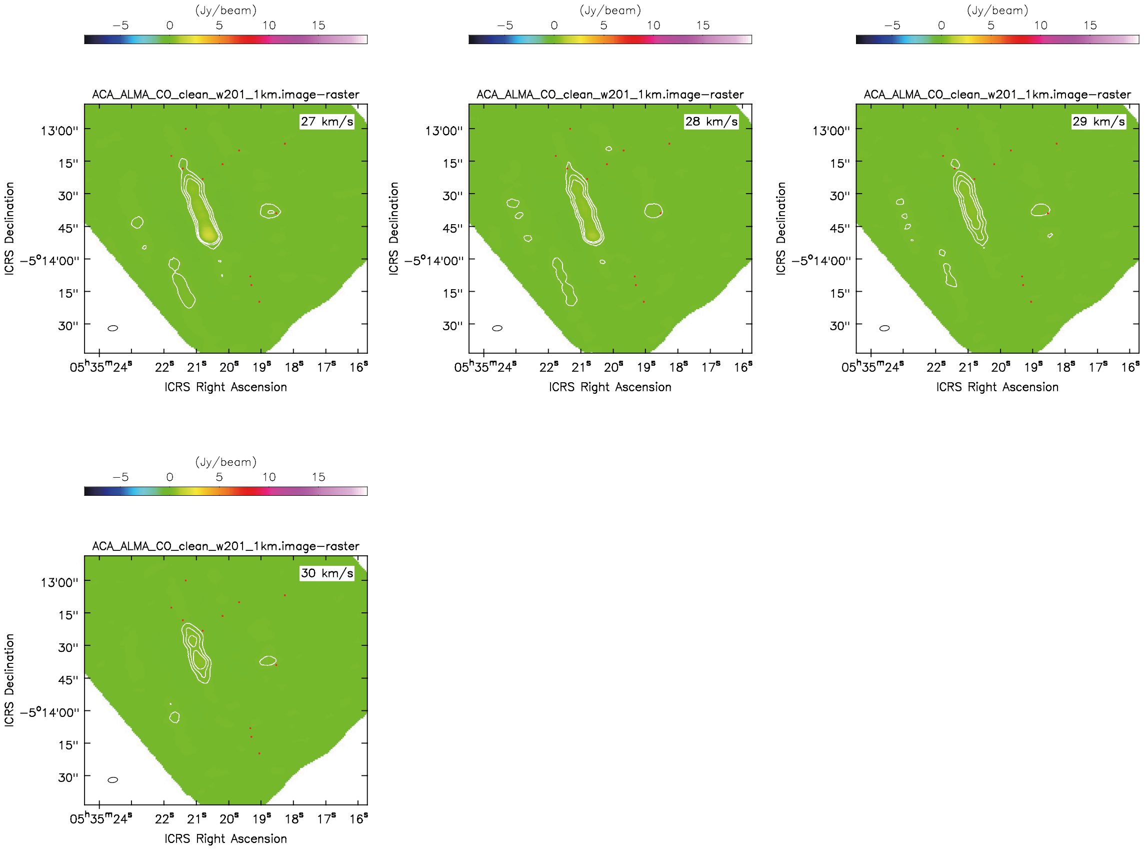

Figure A.22: CO: Combined with ALMA 12m and ACA. The contour level starts at 10σ, [10, 20, 30] (1σ for the continuum image is 14.7 mJy beam^{-1}.) The beam size is indicated by a circle in each panel. The red dots are the position of FIR–ALMA 1 to 21.

ACKNOWLEDGEMENTS

I would like to thank Professor Masahiro Machida, who gave tne the guidance in conduction my research. I would like to express our deep appreciation to my collaborators, Prof. Takahashi, Prof. Koji Tomisaka, and Prof. Shun Ishii at NAOJ. Also, Prof. Minoru Sekiya and Prof. Takashi Okazaki and laboratory members who give me many advices, all I would like to thank you very much. This paper makes use of the following ALMA data: ADS/JAO.ALMA#2017.1.01353.S ALMA is a partnership of ESO (representing its member states), NSF (USA) and NINS (Japan), together with NRC (Canada), MOST and ASIAA (Taiwan), and KASI (Republic of Korea), in cooperation with the Republic of Chile. The Joint ALMA Observatory is operated by ESO, AUI/NRAO and NAOJ.

Bibliography

André, P., J. Di Francesco, D. Ward-Thompson, S. I. Inutsuka, R. E. Pudritz, and J. E. Pineda. 2014. From Filamentary Networks to Dense Cores in Molecular Clouds: Toward a New Paradigm for Star Formation. In *Protostars and Planets VI*, ed. Henrik Beuther, Ralf S. Klessen, Cornelis P. Dullemond, and Thomas Henning, 27.

Arce, H. G., D. Shepherd, F. Gueth, C. F. Lee, R. Bachiller, A. Rosen, and H. Beuther. 2007. Molecular Outflows in Low- and High-Mass Star-forming Regions. In *Protostars and Planets V*, ed. Bo Reipurth, David Jewitt, and Klaus Keil, 245.

Aso, Yoshiyuki, Ken'ichi Tatematsu, Yutaro Sekimoto, Takenori Nakano, Tomofumi Umemoto, Katsuji Koyama, and Satoshi Yamamoto. 2000. Dense Cores and Molecular Outflows in the OMC-2/3 Region. *The Astrophysical Journal Suppliment Series* 131:465–482.

Bachiller, R., and J. Cernicharo. 1990. Extremely high-velocity emission from molecular jets in NGC 6334I and NGC 1333 (HH 7-11). *Astrophysical Journal* 239:276.

Bachiller, R., J. Martin-Pintado, and A. Fuente. 1991a. High-velocity SiO emission in the L1448 outflow. Evidence for dense shocked gas in the molecular bullets. *Astrophysical Journal* 243:L21.

Bachiller, R., J. Martin-Pintado, and P. Planesas. 1991b. High-velocity molecular jets and bullets from IRAS 03282+3035. *Astrophysical Journal* 251:639.

Bachiller, R., J. Martin-Pintado, and P. Planesas. 1991c. High-velocity molecular jets and bullets from IRAS 03282+3035. *Astrophysical Journal* 251:639.

Bachiller, R., M. Pérez Gutiérrez, M. S. N. Kumar, and M. Tafalla. 2001. Chemically active outflow L 1157. *Astrophysical Journal* 372:899–912.

Bachiller, R., and M. Tafalla. 1999. Bipolar Molecular Outflows. In *NATO Advanced Science Institutes (ASI) Series C*, ed. Charles J. Lada and Nikolaos D. Kylafis, volume 540, 227.

Bachiller, Rafael. 1996. Bipolar Molecular Outflows from Young Stars and Protostars. *Astrophysical Journal* 34:111–154.

Banerjee, Robi, and Ralph E. Pudritz. 2006. Outflows and Jets from Collapsing Magnetized Cloud Cores. *Astrophysical Journal* 641:949–960.

Burkert, Andreas, and Lee Hartmann. 2004. Collapse and Fragmentation in Finite Sheets. *Astrophysical Journal* 616:288–300.

Busquet, Gemma, Robert Estalella, Aina Palau, Hauyu Baobab Liu, Qizhou Zhang, Josep Miquel Girart, Itziar de Gregorio-Monsalvo, Thushara Pillai, Guillem Anglada, and Paul T. P. Ho. 2016. What Is Controlling the Fragmentation in the Infrared Dark Cloud G14.225-0.506?: Different Levels of Fragmentation in Twin Hubs. *Astrophysical Journal* 819:139.

Carpenter, John M., Lynne A. Hillenbrand, and M. F. Skrutskie. 2001. Near-Infrared Photometric Variability of Stars toward the Orion A Molecular Cloud. *Astrophysical Journal* 121:3160–3190.

Cesaroni, R., and T. L. Wilson. 1994. An ammonia study of the Orion streamer. *Astrophysical Journal* 281:209–219.

Chini, R., Bo Reipurth, D. Ward-Thompson, J. Bally, L. Å. Nyman, A. Sievers, and Y. Billawala. 1997. Dust Filaments and Star Formation in OMC-2 and OMC-3. *The Astrophysical Journal Letter* 474:L135–L138.

Dionatos, O., B. Nisini, S. Cabrit, L. Kristensen, and G. Pineau Des Forêts. 2010. Spitzer spectral line mapping of the HH211 outflow. *Astrophysical Journal* 521:A7.

Dutrey, A., G. Duvert, A. Castets, W. D. Langer, J. Bally, and R. W. Wilson. 1991. Periodically spaced fragmentation in Orion A. *Astrophysical Journal* 247:L9.

Furlan, E., W. J. Fischer, B. Ali, A. M. Stutz, T. Stanke, J. J. Tobin, S. T. Megeath, M. Osorio, L. Hartmann, N. Calvet, C. A. Poteet, J. Booker, P. Manoj, D. M. Watson, and L. Allen. 2016. VizieR Online Data Catalog: The Herschel Orion Protostar Survey (HOPS): SEDs (Furlan+, 2016). *VizieR Online Data Catalog* J/ApJS/224/5.

Glassgold, A. E., G. A. Mamon, and P. J. Huggins. 1989. Molecule Formation in Fast Neutral Winds from Protostars. *The Astrophysical Journal Letter* 336:L29.

Glassgold, A. E., G. A. Mamon, and P. J. Huggins. 1991. The Formation of Molecules in Protostellar Winds. *Astrophysical Journal* 373:254.

Gómez-Ruiz, A. I., N. Hirano, S. Leurini, and S. Y. Liu. 2013. The L 1157 protostellar outflow imaged with the Submillimeter Array. *Astrophysical Journal* 558:A94.

Gueth, F., S. Guilloteau, and R. Bachiller. 1996. A precessing jet in the L1157 molecular outflow. *Astrophysical Journal* 307:891–897.

Hacar, A., M. Tafalla, J. Kauffmann, and A. Kovács. 2013. Cores, filaments, and bundles: hierarchical core formation in the L1495/B213 Taurus region. *Astrophysical Journal* 554:A55.

Hanawa, Tomoyuki, Fumitaka Nakamura, Tomoaki Matsumoto, and Takenori Nakano. 1994. Fragmentation of Filamentary Molecular Clouds into Pseudo Disks and Further Evolution. In *Clouds, Cores, and Low Mass Stars*, ed. Dan P. Clemens and Richard Barvainis, volume 65 of *Astronomical Society of the Pacific Conference Series*, 151.

Hanawa, Tomoyuki, Fumitaka Nakamura, Tomoaki Matsumoto, Takenori Nakano, Ken'ichi Tatematsu, Tomofumi Umemoto, Osamu Kameya, Naomi Hirano, Tetsuo Hasegawa, Norio Kaifu, and Satoshi Yamamoto. 1993. Effects of Magnetic Fields and Rotation on the Fragmentation of Filamentary Molecular Clouds: Comparison of the Theory with the Orion A Cloud. *The Astrophysical Journal Letter* 404:L83.

Hirano, Naomi, Paul P. T. Ho, Sheng-Yuan Liu, Hsien Shang, Chin-Fei Lee, and Tyler L. Bourke. 2010. Extreme Active Molecular Jets in L1448C. *Astrophysical Journal* 717:58–73.

Ikeda, Norio, Kazuyoshi Sunada, and Yoshimi Kitamura. 2007. A Survey of Dense Cores in the Orion A Cloud. *Astrophysical Journal* 665:1194–1219.

Johnstone, Doug, and John Bally. 1999. JCMT/SCUBA Submillimeter Wavelength Imaging of the Integral-shaped Filament in Orion. *The Astrophysical Journal Letter* 510:L49–L53.

Keene, J., R. H. Hildebrand, and S. E. Whitcomb. 1982. A high resolution submillimeter map of OMC-1. *The Astrophysical Journal Letter* 252:L11–L15.

Kirk, Helen, Philip C. Myers, Tyler L. Bourke, Robert A. Gutermuth, Abigail Hedden, and Grant W. Wilson. 2013. Filamentary Accretion Flows in the Embedded Serpens South Protocluster. *Astrophysical Journal* 766:115.

Kounkel, Marina, Lee Hartmann, Laurent Loinard, Gisela N. Ortiz-León, Amy J. Mioduszewski, Luis F. Rodríguez, Sergio A. Dzib, Rosa M. Torres, Gerardo Pech, Phillip A. B. Galli, Juana L. Rivera, Andrew F. Boden, II Evans, Neal J., Cesar Briceño, and John J. Tobin. 2017. The Gould's Belt Distances Survey (GOBELINS) II. Distances and Structure toward the Orion Molecular Clouds. *Astrophysical Journal* 834:142.

Kudoh, Takahiro, and Kazunari Shibata. 1997. Magnetically Driven Jets from Accretion Disks. I. Steady Solutions and Application to Jets/Winds in Young Stellar Objects. *Astrophysical Journal* 474:362–377.

Kwon, Woojin, Manuel Fernández-López, Ian W. Stephens, and Leslie W. Looney. 2015. Kinematics of the Envelope and Two Bipolar Jets in the Class 0 Protostellar System L1157. *Astrophysical Journal* 814:43.

Lada, Charles J., and Elizabeth A. Lada. 2003. Embedded Clusters in Molecular Clouds. *Astrophysical Journal* 41:57–115.

Lebrón, M., H. Beuther, P. Schilke, and Th. Stanke. 2006. The extremely high-velocity molecular outflow in IRAS 20126+4104. *Astrophysical Journal* 448:1037–1042.

Lee, Chin-Fei, Paul. T. P. Ho, Zhi-Yun Li, Naomi Hirano, Qizhou Zhang, and Hsien Shang. 2017. A rotating protostellar jet launched from the innermost disk of HH 212. *Nature Astronomy* 1:0152.

Lis, D. C., E. Serabyn, Jocelyn Keene, C. D. Dowell, D. J. Benford, T. G. Phillips, T. R. Hunter, and N. Wang. 1998. 350 Micron Continuum Imaging of the Orion A Molecular Cloud with the Submillimeter High Angular Resolution Camera. *Astrophysical Journal* 509:299–308.

Lombardi, M., H. Bouy, J. Alves, and C. J. Lada. 2015. VizieR Online Data Catalog: Orion optical-depth and column-density maps (Lombardi+, 2014). *VizieR Online Data Catalog* J/A+A/566/A45.

Machida, Masahiro N. 2014. Protostellar Jets Enclosed by Low-velocity Outflows. *The Astrophysical Journal Letter* 796:L17.

Machida, Masahiro N., Shu-ichiro Inutsuka, and Tomoaki Matsumoto. 2008. High- and Low-Velocity Magnetized Outflows in the Star Formation Process in a Gravitationally Collapsing Cloud. *Astrophysical Journal* 676:1088–1108.

Maddalena, R. J., M. Morris, J. Moscowitz, and P. Thaddeus. 1986. The Large System of Molecular Clouds in Orion and Monoceros. *Astrophysical Journal* 303:375.

Matsushita, Yuko, Satoko Takahashi, Masahiro N Machida, and Kohji Tomisaka. 2019. A very compact extremely high velocity flow toward mms 5/omc-3 revealed with alma. *The Astrophysical Journal* 871:221.

Myers, Philip C. 2009. Filamentary Structure of Star-forming Complexes. *Astrophysical Journal* 700:1609–1625.

Nielbock, M., R. Chini, and S. A. H. Müller. 2003. The stellar content of OMC 2/3. *Astrophysical Journal* 408:245–256.

Peretto, N., G. A. Fuller, P. Andre, D. Arzoumanian, V. M. Rivilla, S. Bardeau, S. Duarte Puertas, J. P. Guzman Fernandez, C. Lenfestey, G. X. Li, F. A. Olguin, B. R. Rock, H. de Villiers, and J. Wiliams. 2013. VizieR Online Data Catalog: SDC13 infrared dark clouds spectra (Peretto+, 2014). *VizieR Online Data Catalog* J/A+A/561/A83.

Pineda, J. E., and P. S. Teixeira. 2013. Spokes cluster: The search for the quiescent gas. *Astrophysical Journal* 555:A106.

Podio, L., C. Codella, F. Gueth, S. Cabrit, R. Bachiller, A. Gusdorf, C. F. Lee, B. Lefloch, S. Leurini, B. Nisini, and M. Tafalla. 2015. The jet and the disk of the HH 212 low-mass protostar imaged by ALMA: SO and SO_2 emission. *Astrophysical Journal* 581:A85.

Pon, A., D. Johnstone, and M. J. Kaufman. 2011. Molecular Tracers of Turbulent Shocks in GMCs. In *EAS Publications Series*, ed. M. Röllig, R. Simon, V. Ossenkopf, and J. Stutzki, volume 52, 295–296.

Porras, Alicia, Micol Christopher, Lori Allen, James Di Francesco, S. Thomas Megeath, and Philip C. Myers. 2003. A Catalog of Young Stellar Groups and Clusters within 1 Kiloparsec of the Sun. *Astrophysical Journal* 126:1916–1924.

Rosolowsky, E. W., J. E. Pineda, J. Kauffmann, and A. A. Goodman. 2008. Structural Analysis of Molecular Clouds: Dendrograms. *Astrophysical Journal* 679:1338–1351.

Sadavoy, S. I., A. M. Stutz, S. Schnee, B. S. Mason, J. Di Francesco, and R. K. Friesen. 2016. Dust emissivity in the star-forming filament OMC 2/3. *Astrophysical Journal* 588:A30.

Santiago-García, J., M. Tafalla, D. Johnstone, and R. Bachiller. 2009. Shells, jets, and internal working surfaces in the molecular outflow from IRAS 04166+2706. *Astrophysical Journal* 495:169–181.

Schneider, N., T. Csengeri, S. Bontemps, F. Motte, R. Simon, P. Hennebelle, C. Federrath, and R. Klessen. 2010. Dynamic star formation in the massive DR21 filament. *Astrophysical Journal* 520:A49.

Schneider, S., and B. G. Elmegreen. 1979. A catalog of dark globular filaments. *The Astrophysical Journal Suppliment Series* 41:87–95.

Seifried, D., R. E. Pudritz, R. Banerjee, D. Duffin, and R. S. Klessen. 2012. Magnetic fields during the early stages of massive star formation - II. A generalized outflow criterion. *Monthly Notices of the Royal Astronomical Society* 422:347–366.

Shang, Hsien, Anthony Allen, Zhi-Yun Li, Chun-Fan Liu, Mei-Yin Chou, and Jeffrey Anderson. 2006. A Unified Model for Bipolar Outflows from Young Stars. *Astrophysical Journal* 649:845–855.

Shimajiri, Yoshito, Satoko Takahashi, Shigehisa Takakuwa, Masao Saito, and Ryohei Kawabe. 2009. Millimeter- and Submillimeter-Wave Observations of the OMC-2/3 Region. IV Interaction between the Outflow and the Dense Gas in the Cluster Forming Region of OMC-2 FIR 6. *Publications of the Astronomical Sciety of Japan* 61:1055.

Spruit, H. C., T. Foglizzo, and R. Stehle. 1997. Collimation of magnetically driven jets from accretion discs. *Monthly Notices of the Royal Astronomical Society* 288:333–342.

Stanke, T., M. J. McCaughrean, and H. Zinnecker. 2002. An unbiased H_2 survey for protostellar jets in Orion A. II\@. The infrared survey data. *Astrophysical Journal* 392:239–266.

Tafalla, M., J. Santiago, D. Johnstone, and R. Bachiller. 2004. A highly collimated, extremely high velocity outflow in Taurus. *Astrophysical Journal* 423:L21–L24.

Tafalla, M., J. Santiago-García, A. Hacar, and R. Bachiller. 2010. A molecular survey of outflow gas: velocity-dependent shock chemistry and the peculiar composition of the EHV gas. *Astrophysical Journal* 522:A91.

Tafalla, M., Y. N. Su, H. Shang, D. Johnstone, Q. Zhang, J. Santiago-García, C. F. Lee, N. Hirano, and L. Y. Wang. 2017. Anatomy of the internal bow shocks in the IRAS 04166+2706 protostellar jet. *Astrophysical Journal* 597:A119.

Takahashi, Satoko, Paul T. P. Ho, Paula S. Teixeira, Luis A. Zapata, and Yu-Nung Su. 2013. Hierarchical Fragmentation of the Orion Molecular Filaments. *Astrophysical Journal* 763:57.

Takahashi, Satoko, Masao Saito, Nagayoshi Ohashi, Nobuhiko Kusakabe, Shigehisa Takakuwa, Yoshito Shimajiri, Motohide Tamura, and R. Kawabe. 2008. Millimeter- and Submillimeter-Wave Observations of the OMC-2/3 Region. III. An Extensive Survey for Molecular Outflows. *Astrophysical Journal* 688:344–361.

Tatematsu, Ken'ichi, Ryo Kandori, Tomofumi Umemoto, and Yutaro Sekimoto. 2008. N_2H^+ and HC_3N Observations of the Orion A Cloud. *Publications of the Astronomical Sciety of Japan* 60:407.

Teixeira, P. S., S. Takahashi, L. A. Zapata, and P. T. P. Ho. 2016. Two-level hierarchical fragmentation in the northern filament of the Orion Molecular Cloud 1. *Astrophysical Journal* 587:A47.

Teixeira, Paula S., Charles J. Lada, Erick T. Young, Massimo Marengo, August Muench, James Muzerolle, Nick Siegler, George Rieke, Lee Hartmann, S. Thomas Megeath, and Giovanni Fazio. 2006. Identifying Primordial Substructure in NGC 2264. *The Astrophysical Journal Letter* 636:L45–L48.

Teixeira, Paula S., Luis A. Zapata, and Charles J. Lada. 2007. A Dense Microcluster of Class 0 Protostars in NGC 2264 D-MM1. *The Astrophysical Journal Letter* 667:L179–L182.

Tomisaka, Kohji. 2002. Collapse of Rotating Magnetized Molecular Cloud Cores and Mass Outflows. *Astrophysical Journal* 575:306–326.

van Terwisga, S. E., A. Hacar, and E. F. van Dishoeck. 2019. VizieR Online Data Catalog: Disk masses in the Orion Molecular Cloud-2 (van Terwisga+, 2019). *VizieR Online Data Catalog* J/A+A/628/A85.

Wang, Ke, Qizhou Zhang, Leonardo Testi, Floris van der Tak, Yuefang Wu, Huawei Zhang, Thushara Pillai, Friedrich Wyrowski, Sean Carey, Sarah E. Ragan, and Thomas Henning. 2014. Hierarchical fragmentation and differential star formation in the Galactic 'Snake': infrared dark cloud G11.11-0.12. *Monthly Notices of the Royal Astronomical Society* 439:3275–3293.

Zhang, Qizhou, T. R. Hunter, J. Brand, T. K. Sridharan, S. Molinari, M. A. Kramer, and R. Cesaroni. 2001. Search for CO Outflows toward a Sample of 69 High-Mass Protostellar Candidates: Frequency of Occurrence. *The Astrophysical Journal Letter* 552:L167–L170.